

**EFFECT OF THE ADDITIONAL ELECTRON ACCEPTOR
IN HYBRID ZnO:P3HT:PCBM SPIN-COATED FILMS
FOR PHOTOVOLTAIC APPLICATION**

**By
Thinavhuyo Albert Ramashia**

A Thesis Submitted in Fulfilment of the Requirements for the
Degree of Magister Scientiae in the Department of Physics,
University of the Western Cape

The logo of the University of the Western Cape, featuring a classical building facade with columns and a pediment, with the text "UNIVERSITY of the WESTERN CAPE" below it.

Supervisor: Dr. T.F.G Muller (University of the Western Cape)

Co-supervisor:

Dr. D.E. Motaung (Council for Scientific and Industrial Research)

FEBRUARY 2015

ACKNOWLEDGMENTS

I have taken efforts in this project. However, it would not have been possible without the kind support and help of many individuals and organizations. I would like to extend my sincere thanks to all of them.

My profound gratitude goes to Dr. Theo Muller (Department of Physics, University of the Western Cape (UWC)) for the exceptional supervision, guidance, friendship and the sustained support throughout the duration of this thesis.

Dr. David Motaung (National Centre for Nano-Structured Materials, Council for Scientific and Industrial Research) who acted as a co-supervisor, for his constant encouragement, guidance, support, friendship and many fruitful discussions.

Dr. Franscious Cummings and Dr. Gerald Malgas (Department of Physics, UWC), for their constant support throughout this project.

Prof. Christopher Arendse (Department of Physics, UWC), for his constant encouragement, guidance and many fruitful discussions.

My special thanks go to Mrs. Angela Adams and Miss. Shirese Spannenberg (Department of Physics, UWC), for always helping me with all the administration work.

The wonderful staff at the Physics Department of UWC, for their support and encouragement.

I credit also Dr. Remy Bucher (iThemba LABS) who always is available for discussion in crystal structure and XRD patterns, Mr Timothy Lesch (Department of Chemistry, University of the Western Cape), for the FTIR measurements.

I salute all my fellow MANUS/MATSCI, after all, we have shared "a home" for years now, and I will not forget our FIFA days and other activities. For many invigorating discussions, whether scientific or not, I thank all my colleagues and friends at UWC and elsewhere.

My profound gratitude goes to my CAPE TOWN family, D005 family (UNIVEN) and DENGA family (Thohoyandou).

I am overwhelmingly thankful to Khathutshelo Millicent Nedzamba your everlasting support throughout this work has been amazing and may the Almighty God bless you more.

Livhuwani "CEE" Mudau for extending your hand when I needed you the most, Ndi a livhuwa khomba ya Vho-Martha (RIP).

Family: I am very grateful to my mother (Naledzani Elisah Tsedu), siblings (Mpho Israel, Azwimbavhi Tsiko Eunice, Rudzani Godfrey) and the extended family for the continued support and believing in me throughout my studies. **NDI KHOU LIVHUWA KHA ZWOTHE.**

Sponsorship: I would also like to thank the University of the Western Cape and the National Research Foundation (NRF) for funding my studies.

They that hope in the LORD will renew their strength, they will soar as with eagles' wings; they will run and not grow weary, walk and not grow faint.

(Isaiah 40:31)

DEDICATED TO MY FIRST BORN

MY SOURCE OF INSPIRATION

MY ANGEL



DADDY'S LITTLE GIRL.....

UNIVERSITY of the
WESTERN CAPE

“DAKALO AKONAHO OLIVIA RAMASHIA”

(Born: 26 June 2015)

DECLARATION

I declare that

**“EFFECT OF THE ADDITIONAL ELECTRON ACCEPTOR IN
HYBRID ZnO:P3HT:PCBM SPIN-COATED FILMS FOR
PHOTOVOLTAIC APPLICATION”**



Is my own work, that it has not been submitted for any degree or examination in any other university, and that all the sources I have used or quoted have been indicated and acknowledged by means of complete references.

Thinavhuyo Albert Ramashia

FEBRUARY 2015

Signature: --

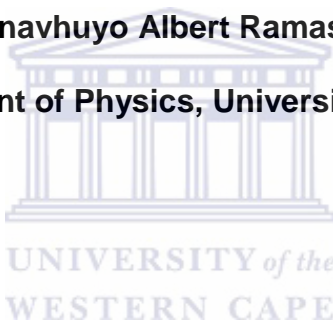
KEYWORDS

**“EFFECT OF THE ADDITIONAL ELECTRON ACCEPTOR IN HYBRID
ZNO:P3HT:PCBM SPIN-COATED FILMS FOR PHOTOVOLTAIC
APPLICATION”**

By

Thinavhuyo Albert Ramashia

MSc Thesis, Department of Physics, University of the Western Cape



Poly (3-hexylthiophene)

Fullerene

Organic photovoltaics

Hybrid solar cells

Inorganic semiconductor

Zinc oxide

Phase separation

Electron acceptor

Efficiency

Spin coating

ABSTRACT

“EFFECT OF THE ADDITIONAL ELECTRON ACCEPTOR IN HYBRID ZNO:P3HT:PCBM SPIN-COATED FILMS FOR PHOTOVOLTAIC APPLICATION”

By

Thinavhuyo Albert Ramashia

MSc Thesis, Department of Physics, University of the Western Cape

In a quest for low operational and maintenance cost solar cell devices, organic photovoltaics remain a potential source of energy worthy to be explored. In order to generate cost-effective electricity from solar energy, either the efficiency of the solar cells must be improved or alternatively the manufacturing cost must be lowered. The power conversion efficiency (PCE) of organic photovoltaics is influenced by the choice of electron acceptor material, the structure of the polymer, the morphology of the film, the interfaces between the layers and the ratio between the electron acceptor material and the polymer. Nevertheless, efficiency is still limited compared to conventional silicon based PV cells due to low mobility of charge carriers with a short exciton diffusion length in the active layer. Currently, hybrid solar cells have been considered as one of the most promising concepts to address the limited efficiency of organic solar cells.

Therefore in this thesis ZnO nanoparticles were synthesized using hydrothermal assisted method. These nanoparticles were incorporated in the poly (3-hexylthiophene) (P3HT):[6,6]-phenyl-C₆₁-butyric acid methyl ester (PCBM), and used as additional acceptors of electrons released from the polymer donor material, with the anticipation to increase the electron mobility, and ultimately the PCE. The thermo-gravimetric analyses revealed improved thermal stability of P3HT upon incorporating ZnO in the polymer matrix. X-ray diffraction analyses revealed that the diffraction peaks shift to higher angles when incorporating the ZnO in the P3HT:PCBM surface and this is consistent with the Raman observation.

The photovoltaic properties demonstrated that the addition of ZnO nanoparticles in P3HT:PCBM bulk-heterojunction increases PCE from a baseline of ~1.0 % in the P3HT:PCBM system to 1.7% in the P3HT:PCBM:ZnO ternary system. The enhanced PCE was due to improved absorption as compared to its counterparts. Upon increasing the addition of ZnO nanoparticles in the P3HT:PCBM matrix, the PCE decreases, due to a large phase separation between the polymer, PCBM and ZnO induced by ZnO agglomerations which resulted in increased surface roughness of the active layer. These findings signify that incorporation of ZnO nanostructures in the P3HT:PCBM polymer matrix facilitates the electron transport in the photoactive layer which results to improved efficiency.

TABLE OF CONTENTS

CHAPTER 1	1
BACKGROUND AND SCOPE OF INVESTIGATION	1
1.1. INTRODUCTION	1
1.2. PHOTOVOLTAICS (PVs)	2
1.2.1. Crystalline Silicon PV	2
1.2.2. Thin Film PV	3
1.2.3. Organic PV	5
1.2.4. Hybrid PV	6
1.3. HYBRID SOLAR CELLS	7
1.4. CHARGE TRANSFER MECHANISM IN ORGANIC PHOTOVOLTAICS	10
1.5. OPTIMIZATION OF ORGANIC PHOTOVOLTAICS	12
1.6. DEVICE EFFICIENCY	14
1.6.1. Short- circuit current	15
1.6.2. Open-circuit voltage	16
1.6.3. Fill factor (FF)	17
1.6.4. Power conversion efficiency (η)	18



1.7. HYBRID SOLAR CELL MATERIALS	18
1.7.1. Poly (3-hexylthiophene).....	18
1.7.2. Phenyl-C ₆₁ -butyric acid methyl ester.....	20
1.7.3. Zinc Oxide (ZnO)	21
1.7.3.1. Introduction	21
1.7.3.2. Crystal Structure	22
1.7.3.3. Lattice parameters	24
1.7.3.4. Nano- ZnO Synthesis	25
1.8. AIMS AND OUTLINE	26
1.9. REFERENCES	28
CHAPTER 2	34
ANALYTICAL TECHNIQUES	34
2.1. INTRODUCTION.....	34
2.2. X-RAY DIFFRACTION	36
2.2.1. Introduction.....	36
2.2.2. Theory.....	37
2.2.3. Experimental set-up.....	43
2.3. HIGH RESOLUTION TRANSMISSION ELECTRON MICROSCOPY	43
2.3.1. Introduction	43
2.3.3. Experimental set-up.....	54



2.4. HIGH RESOLUTION SCANNING ELECTRON MICROSCOPY	55
2.4.1. Introduction.....	55
2.4.2. Theory	56
2.4.3. Experimental set- up	61
2.5. RAMAN SPECTROSCOPY.....	62
2.5.1. Introduction.....	62
2.5.2. Theory	63
2.5.3. Experimental set-up	65
2.6. UV-VIS SPECTROSCOPY.....	66
2.6.1. Introduction.....	66
2.6.2. Theory	66
2.6.3. Experimental set- up	70
2.7. FOURIER TRANSFORM INFRARED SPECTROSCOPY.....	72
2.7.1. Introduction	72
2.7.2. Theory	73
2.7.3. Experimental set- up	75
2.8. X-RAY PHOTOELECTRON SPECTROSCOPY	75
2.8.1. Introduction.....	75
2.8.2. Theory	76
2.8.3. Experimental set- up	76



2.9.	PHOTOLUMINESCENCE SPECTROSCOPY	78
2.9.1.	Introduction	78
2.9.2.	Experimental set- up	79
2.10.	ATOMIC FORCE MICROSCOPY	80
2.10.1.	Introduction	80
2.10.2.	Theory.....	81
2.10.3.	Experimental set-up.....	84
2.12.	REFERENCES.....	84
CHAPTER 3	88
STRUCTURAL AND OPTICAL PROPERTIES OF ZnO		
GROWN BY HYDROTHERMAL METHOD	88
3.1.	INTRODUCTION	88
3.2.	EXPERIMENTAL DETAILS	89
3.2.1.	Synthesis of ZnO nanoparticles	89
3.2.2.	Characterization.....	89
3.3.	RESULTS AND DISCUSSION	91
3.3.1.	Thermal analysis	91
3.3.2.	Structural Properties.....	92
3.3.3.	Surface Morphology	101
3.3.4.	Optical properties.....	104

3.3.4.1. Reflectance Properties.....	108
3.3.4.2. Transmittance Properties	109
3.4. CONCLUSION.....	111
3.5. REFERENCES	112
CHAPTER 4.....	114
EFFECT OF ZnO AS AN ADDITIONAL ELECTRON ACCEPTOR ON THE PHOTOVOLTAIC PROPERTIES OF P3HT:PCBM: ZnO TERNARY STRUCTURE .	114
4.1. INTRODUCTION	114
4.2. SAMPLE PREPARATION.....	115
4.3. RESULTS AND DISCUSSION	116
4.3.1. Thermal Analysis.....	116
4.3.2. Effect of chloroform as a casting solvent.....	118
4.3.2.1. Structural properties	118
4.3.2.2. Surface morphology	123
4.3.3. Effect of 1, 2 dichlorobenzene as a casting solvent	127
4.3.3.1. Structural properties	127
4.3.3.2. Surface morphology	133
4.3.3.3. Optical properties	136
4.3.3.4. Photovoltaic properties.....	138
4.4. CONCLUSION.....	144

4.5. REFERENCES 146

SUMMARY 150

FUTURE WORK 151



CHAPTER 1

BACKGROUND AND SCOPE OF INVESTIGATION

1.1. INTRODUCTION

Fossil fuels as used in the developing and developed countries remain the most effective form of energy generation, even into the twenty-first century. Fossil fuels, which have been formed from the fossilized remains of prehistoric plants and animals, including coal, oil and natural gas have played a fundamental role in the production of electrical energy. However, the disadvantage is that fossil fuels pollute the environment and are not renewable. Renewable resources provide alternative forms of energy such as solar energy, hydrothermal energy and wind energy, and looks set to replace fossil fuels in future, because unlike fossil fuels they are inexhaustible and environmental friendly. For example, making use of solar energy to meet human needs has seen the photovoltaic (PV) field growing in leaps and bounds. One of the technologies employed to achieve this is the photovoltaic generation of energy, which uses the photovoltaic effect to convert solar energy into electrical energy by means of a PV device. However, efficient harvesting of solar energy is one of the great scientific and industrial challenges of today. Environmental, social, and economic factors all motivate such research. In the field of polymer PV the bulk heterojunction (BHJ) device is the current design to achieve the highest efficiencies with organic films. In this thesis, the current laboratory standard materials used in bulk heterojunction PV devices are therefore investigated.

1.2. PHOTOVOLTAICS (PVs)

Conventional solar cells based on silicon technology have low operational and maintenance costs, but their main drawback is the high initial costs of fabrication [1.1-1.7]. In order to generate cost-effective electricity from solar energy, either the efficiency of the solar cells must be improved or alternatively the manufacturing cost must be lowered. Hence continuous research has been carried out in this direction and has led to generations of PV technologies.

1.2.1. Crystalline Silicon PV

The first generation photovoltaic cells are the dominant technology in the commercial production of solar cells and account for nearly 80% of the solar cell market [1.8]. These cells are typically made using a crystalline silicon (c-Si) wafer. The typical efficiency of such silicon-based commercial photovoltaic energy systems is in the order of 15% [1.9]. In these cells a substantial increase of their efficiency up to 33% is theoretically possible, but the best laboratory cells have power conversion efficiency (PCE) of only about 25% [1.10-1.13]. The starting material used to prepare c-Si must be refined to a purity of 99.99 % [1.14]. This process is very laborious and energy intensive; as a result manufacturing plant capital cost is as high as 60% of manufacturing cost [1.15]. The cost of generating electricity using silicon solar modules is typically 10 times higher than that from fossil fuel which inhibits their widespread application. The main advantages of first generation solar cells are their broad spectral absorption range, high carrier mobility and high efficiency [1.16, 1.17]. However, the main disadvantages are:

they require expensive manufacturing technologies [1.18], most of the energy of higher energy photons, at the blue and violet end of the spectrum is wasted as heat, and they are poor absorbers of light.

1.2.2. Thin Film PV

Second generation solar cells are usually called thin-film solar cells. This generation basically has three types of solar cells made of amorphous silicon (a-Si), cadmium telluride (CdTe), and copper indium gallium diselenide (CIGS). Furthermore, thin film production market share in the global solar PV market grew from a mere 2.8% in 2001 to 25% in 2009; this indicates a growing market share of these solar cells in future (see Figure 1.1) [1.19]. These devices are typically made by depositing a thin layer of photo-active material onto glass or a flexible substrate (see figure 1.2). The driving force for the development of thin film solar cells has been their potential for the reduction of manufacturing costs. Moreover, as these semiconductors have direct band gaps which lead to higher absorption coefficients, it results in the fact that less than a 1 μm thick semiconductor layer is required to absorb solar radiation; this thickness is 100-1000 times less than the thickness required for crystalline Si [1.20]. Thinner layers can be used to increase the electric field strength across the material and hence can provide better stability. However, the use of thinner layers reduces light absorption, which causes a reduction in cell efficiency. CdTe has a nearly optimal band gap and can be easily deposited with thin film techniques. Over 16.7% efficiencies have been achieved in the laboratory for the CdTe solar cells [19]. CdTe is usually deposited on cadmium sulfide (CdS) to form a p-n junction photovoltaic solar cell (see Figure 1.2(c) for basic

device configuration for this generation solar cell). When copper indium diselenide (CIS) is modified by adding gallium, it exhibited a record laboratory efficiency of 20.3 % among thin film materials [1.21]. It also shows excellent stability. At the moment CIGS is the most promising candidate for solar cells based on these technologies.

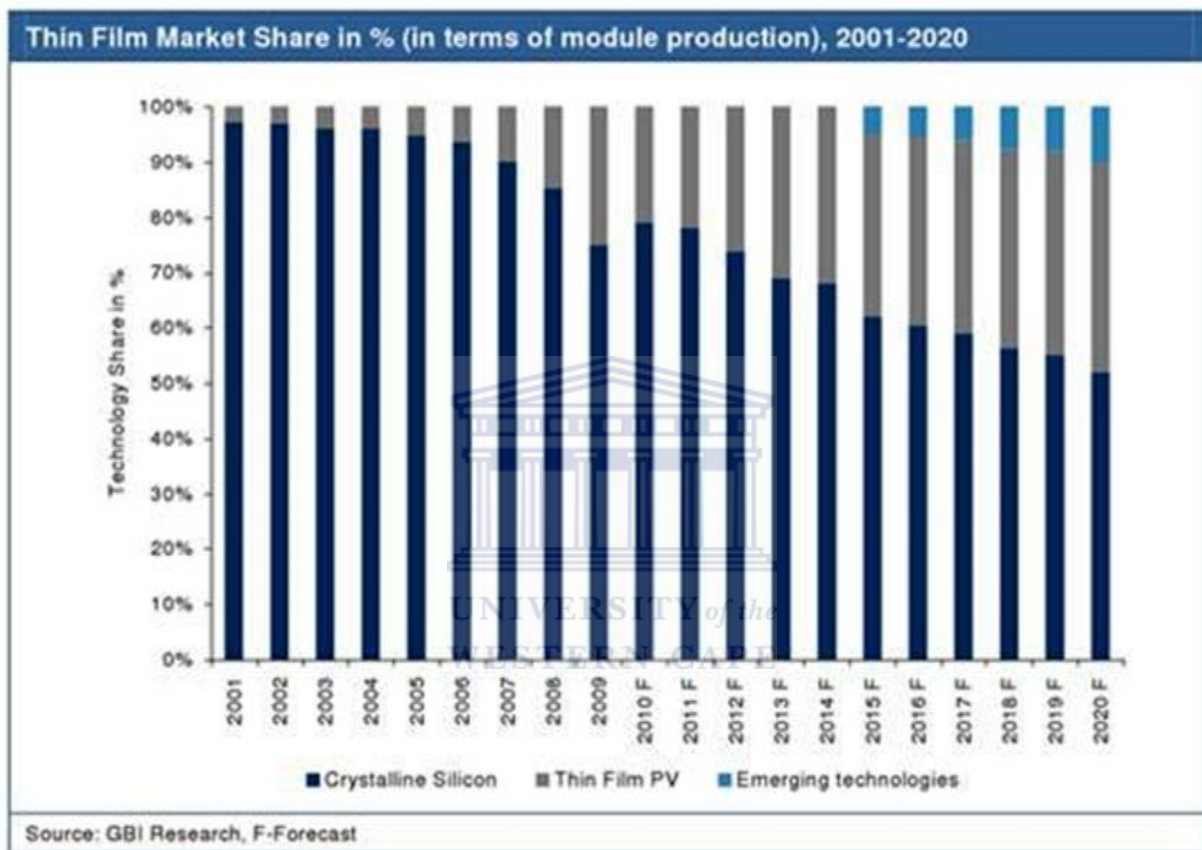


Figure 1.1: Market shares of different solar PV technologies [1.21].

The photovoltaic devices based on these materials have shown efficiencies of 15-20% [1.23-1.26], somewhat less than that of solar cells based on monocrystalline silicon. This is due to the relatively poor charge transport in these materials compared to monocrystalline silicon. This means that the promise of low cost power has not yet been realized by these technologies.

Metal(front)	Metal(Back)	Metal(Back)	TCO
n-Si	n-a-Si	CdTe	CdS
P-Si	i-μc-Si	CdS	CIGS
	p-μc-Si	TCO (front)	Mo (Back)
	TCO (front)	glass	glass -Metal foil
Metal(Back)	glass	glass	glass -Metal foil
A	B	C	D

Figure 1.2: Device configurations for (a) c-Si, (b) a-Si, (c) CdTe and, (d) CIGS solar cells [1.26].

1.2.3. Organic PV

Third generation technologies aim to enhance poor electrical performance of second generation thin films technologies while maintaining very low production costs. Currently, most of the work on third generation solar cells is being done in the laboratory and being developed by new companies and most part of it is still not commercially available. Today, the third generation approaches being investigated include nanocrystal solar cells, photo electrochemical cells (PEC), dye-sensitized hybrid solar cells (DSSC), tandem cells, organic photovoltaic cells (OPV), and the cells based on the materials that generate multiple electron-hole pairs [1.27]. These cells are based on low energy, high-throughput processing technologies e.g. OPV are: chemically synthesized and solution processable, have low material cost, large area deposition potential and are light weight and flexible [1.28]. The Graetzel (DSSC) cell is an attractive replacement for existing technologies in "low weight" applications like rooftop

solar collectors; they work even in low-light conditions [1.29]. However, efficiencies of all third generation cells are lower as compared to first and second generation PV technologies. Secondly their efficiencies decay with time due to degradation effects under environmental conditions [1.26].

1.2.4. Hybrid PV

Nowadays a lot of research has been focused on hybrid materials, which is a promising candidate to enhance the efficiency of solar cells through enhanced use of the solar spectrum, a higher aspect ratio of the interface, and the good processability of polymers [1.30]. This has led to the development of fourth generation solar cells. Hybrid polymer solar cells [1.30-1.33] consist of conjugated polymers such as poly(3-hexylthiophene) (P3HT), poly[2-methoxy-5-(2-ethylhexyloxy)-1,4] MEH-PPV, etc. and semiconducting material such as CdTe, titanium dioxide (TiO₂), lead selenide (PbSe), lead sulphide (PbS), zinc oxide (ZnO), cadmium selenide telluride (CdSeTe), CdS, carbon nanotubes (CNT) and cadmium selenide (CdSe) [1.34-1.37].

Hybrid PV systems have attracted considerable research attention because of their potential for large area deposition, are flexible, easily processable, and can be manufactured at low-cost. Moreover, hybrid materials have the ability to tune each component in order to achieve composite films optimized for solar energy conversion.

1.3. HYBRID SOLAR CELLS

Polymer-based solar cells suffer from lower efficiencies and a limited lifetime as compared to silicon-based solar cells. The limited efficiency of the BHJ polymer solar cell is due to the poor carrier mobility, the short exciton diffusion length, the charge trapping, and the mismatch of the absorption spectrum of the active layer and the solar emission [1.38, 1.39]. To address these fundamental limitations of polymer solar cells, new strategies have been developed by blending inorganic nanoparticles (NPs) with organic materials which integrate the benefits of both classes of materials. These hybrid materials are potential systems for OPV devices because it includes the desirable characteristics of organic and inorganic components within a single composite. They possess the advantage of tunability of photo-physical properties of the inorganic nanoparticles and also retain the polymer properties like solution processing, fabrication of devices on large and flexible substrates [1.40]. Blends of conjugated polymers and nanoparticles are similar to that of used in organic BHJ solar cells. Excitons created upon photo-excitation are separated into free charge carriers at organic-inorganic interfaces. Electrons will then be accepted by the material with the higher electron affinity, and the hole by the material with the lower ionization potential. The use of inorganic semiconductor nanoparticles (NPs) embedded in semiconducting polymers is promising for several reasons, such as [1.41]:

- ❖ Inorganic NPs have high absorption coefficients.
- ❖ They are superb electron acceptors having high electron affinity and high electron mobility.

- ❖ A substantial interfacial area for charge separation is provided by NPs, which have high surface area to volume ratios.
- ❖ NPs are prepared by inexpensive wet chemical synthesis route, hence NPs are cost effective.
- ❖ The NPs are easily dispersed in the polymers which can be spin-coated for large area and flexible devices.
- ❖ They show good physical and chemical stability.

Therefore, hybrid polymer-nanoparticles solar cells have recently gained a lot of attention in the scientific community and have also shown considerable PCEs.



Table 1.1: Device configuration and parameters for a range of selected hybrid solar cells [1.12, 1.18, 1.32, and 1.35].

Device configuration	Voc (V)	Jsc (mA/cm ²)	EQE	PCE (%)	References
PCPDTBT: CdSe tetrapods	0.67	10.10	0.55	3.2	S. Daya et al., Nano Lett. 10 (2010) 239
P3HT: CdSe QDs	0.62	5.80		2	Y. Zhou et al., APL, 96 (2010) 013304
P3HT: CdSe nanorods	0.62	8.79	0.70	2.6	B. Sun et al., Phys. Chem Chem. Phys 8 (2006) 3557
OC1C10-PPV: CdSe	0.75	9.10	0.52	2.8	B. Sun et al., J Appl Phys 97 (2005) 014914
P3HT:PCBM:Pt QDs	0.64	10		4.08	M. Y. Chang et al J. Electrochem. Soc. 156 (2009) B234
PCBM:PbS	0.24	14.0		1.68	N. Zhao et al. ACS Nano 4 (2010) 3743.
P3HT:GaAs-TiOx	0.59	7.16		2.36	S. Ren et al. Nano Lett. 11 (2011) 408
P3HT:CdS(in-situ)	0.64			2.9	H-C. Liao et al. Macromol. 42 (2009) 6558
P3HT:ZnO (in-situ)	0.75	5.2	0.44	2.0	S. D. Oosterhout et al. Nat. Mater. 8 (2009) 818

From table 1.1 it is evident that the P3HT:PCBM:Pt solar cell with efficiency of 4.08%, by far is the crowning achievement for hybrid solar cells, even though the challenge of the cost of the platinum (Pt) remains as it is very expensive. However, an

impressive PCE of over 2% has been reported for ZnO/P3HT solar cells. This has fuelled the possibility of replacing platinum (Pt) with Zinc Oxide (ZnO). In this thesis the application of ZnO in the polymer-fullerene P3HT:PCBM mixture is therefore further explored.

1.4. CHARGE TRANSFER MECHANISM IN ORGANIC PHOTOVOLTAICS

Upon irradiation an electron is excited from the highest occupied molecular orbital (HOMO) to the lowest unoccupied molecular orbital (LUMO), forming an exciton (Figure 1.3), which is an electron-hole pair. This process is followed by exciton dissociation [1.42]. The electron must then reach one electrode while the hole must reach the other electrode. In order to achieve charge separation an electrical field is important; this electrical field is provided by the workfunction of the electrodes. As a result the electron-flow is more favoured from the low-workfunction electrode to the high-workfunction electrode (forward bias), a phenomenon referred to as rectification [1.43]. A schematic of the light absorbing process along with the positioning of energy levels is shown in Figure 1.3.

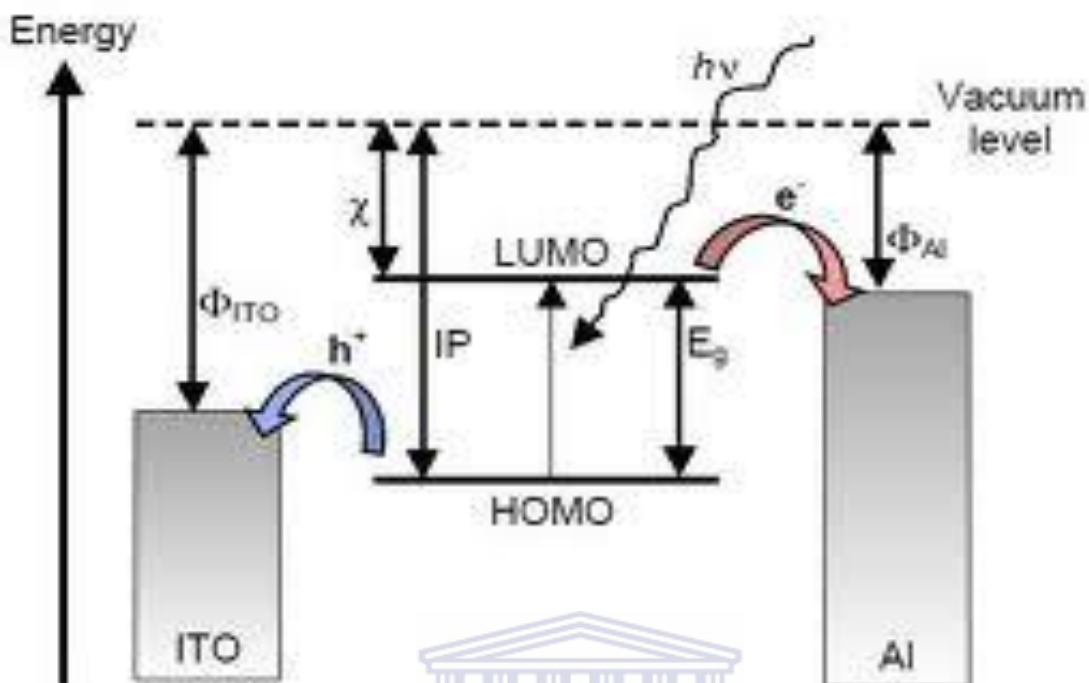


Figure 1.3: Light harvesting and energy levels [1.43].

The figure depicts electrons transferred to the aluminium electrode (Al) at the same time that holes are collected at the Indium Titanium oxide (ITO) electrode. Other parameters depicted in the schematic are Φ , which is the workfunction, χ is the electron affinity, IP is the Ionisation Potential and E_g is the band gap energy.

The charge carrier mobility of organic and polymeric semiconductors is generally low compared to inorganic semiconductors because the HOMOs and LUMOs in the organic semiconductors do not interact strong enough to form a conduction band (CB) and a valence band (CV), whereas in the inorganic semiconductors, HOMOs and LUMOs form a CB and VB throughout the material [1.42]. Thus it is important to

complement the organic and polymeric semiconductors with an inorganic semiconductor, as to allow better charge transfer within the bands. The effect of bringing two different semiconductors in contact causes the electrical field at the heterojunction interface. This field allows the excitons diffusing to the interface to dissociate. Charge transfer is much more efficient at the donor-acceptor interface than at the electrode interface [1.44].

1.5. OPTIMIZATION OF ORGANIC PHOTOVOLTAICS

Optimization of OPVs offers a better understanding of energy conversion in order to improve their performance. Optimizing the performance of organic photovoltaics does depend strictly on their mechanism of operation. There are four fundamental steps involved in the energy conversion process namely [1.45]:

1. Absorption of light and generation of excitons
2. Diffusion of the exciton
3. Dissociation of the exciton to generate charge
4. Charge transfer and collection

Figure 1.4 shows the mechanism of energy conversion using the fundamental steps outlined above.

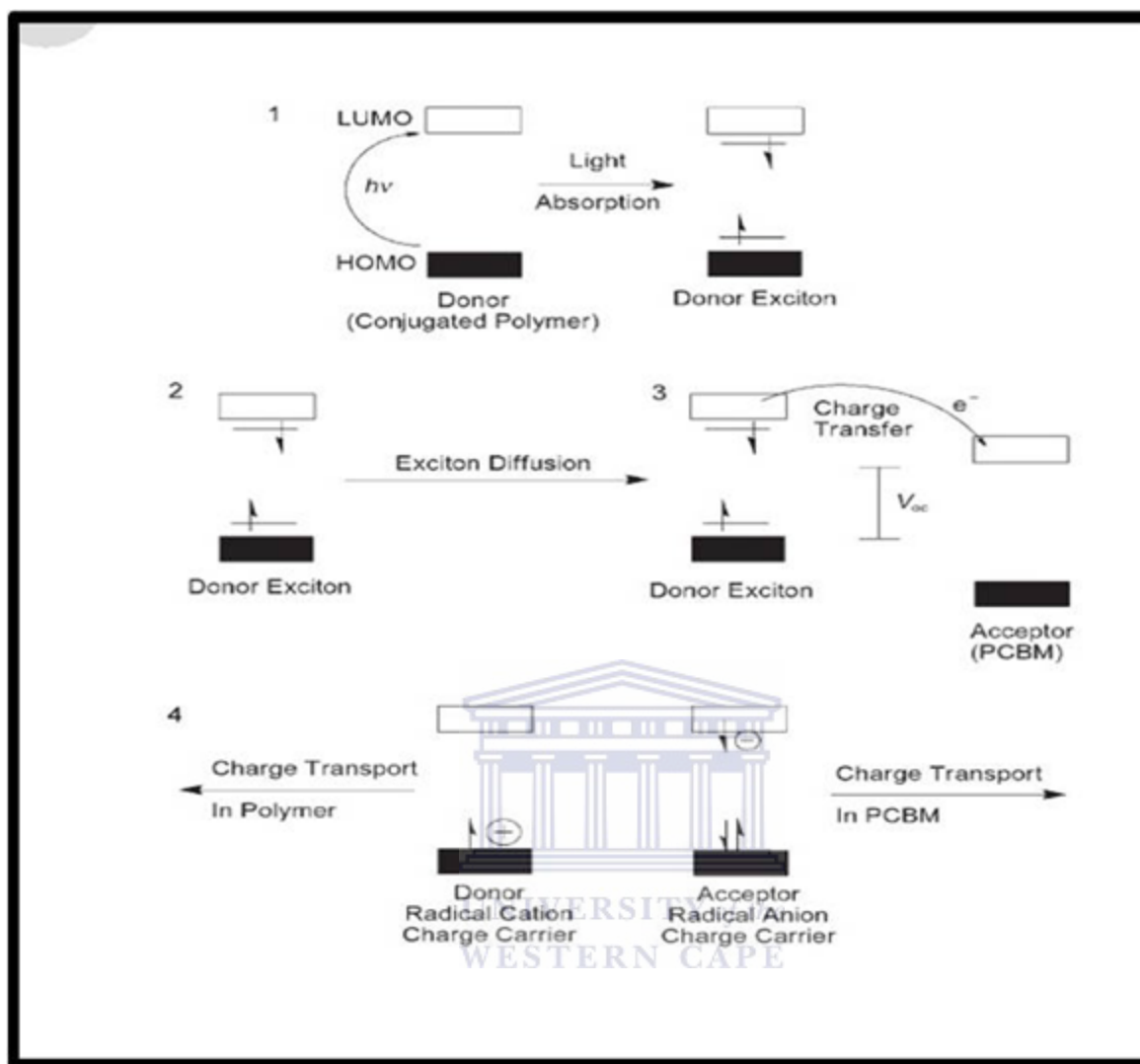


Figure 1.4: General mechanism for energy conversion in excitonic solar cells [1.45].

The energy difference between the HOMO of the donor and the LUMO of the acceptor is determined by how the energy of the donor relates to that of the acceptor (Figure 1.4) hence it is clear that the materials of the active layer together with their morphology will have a major impact on the overall performance of the solar cell.

In general, by adjusting the electronic properties and interactions of the donor – acceptor constituents, it is possible to optimise the polymer-fullerene solar cell. This is important in order to absorb more radiant energy, since enhanced absorption generates large numbers of free charges. At the same time those free charges should be transported to their respective electrodes at a maximum rate and with minimum recombination. However, this approach satisfies the electrical characteristics such as charge carrier mobility and absorption coefficient but fails to account for the morphological aspect [1.45].

The morphological aspect is paramount as the performance of BHJ solar cells depends on the physical interaction of the donor-acceptor constituent even though the donor-acceptor shares an ideal relationship. Ideally the BHJ solar cell is known as a bi-continuous constituent of a donor-acceptor with maximum interfacial area for exciton dissociation and a mean domain size corresponding with the exciton diffusion length of 5-10 nm [1.44]. The two constituents should phase-segregate on a suitable length scale to allow maximum rate ordering within each phase, and thus effective charge transport in continuous pathways to the electrodes in order to maintain the recombination of free charges at a minimum. The constituents should also self-assemble into the most favourable morphology with long term stability, hence the importance of understanding the morphology of the polymer-fullerene solar cell.

1.6. DEVICE EFFICIENCY

A solar cell under illumination is characterized by the following parameters: the short circuit current (J_{SC}), the open- circuit voltage (V_{OC}), the fill factor (FF) and the

PCE (η). These parameters are indicated on the J-V characteristic curve of a solar cell, as shown in Figure 1.5.

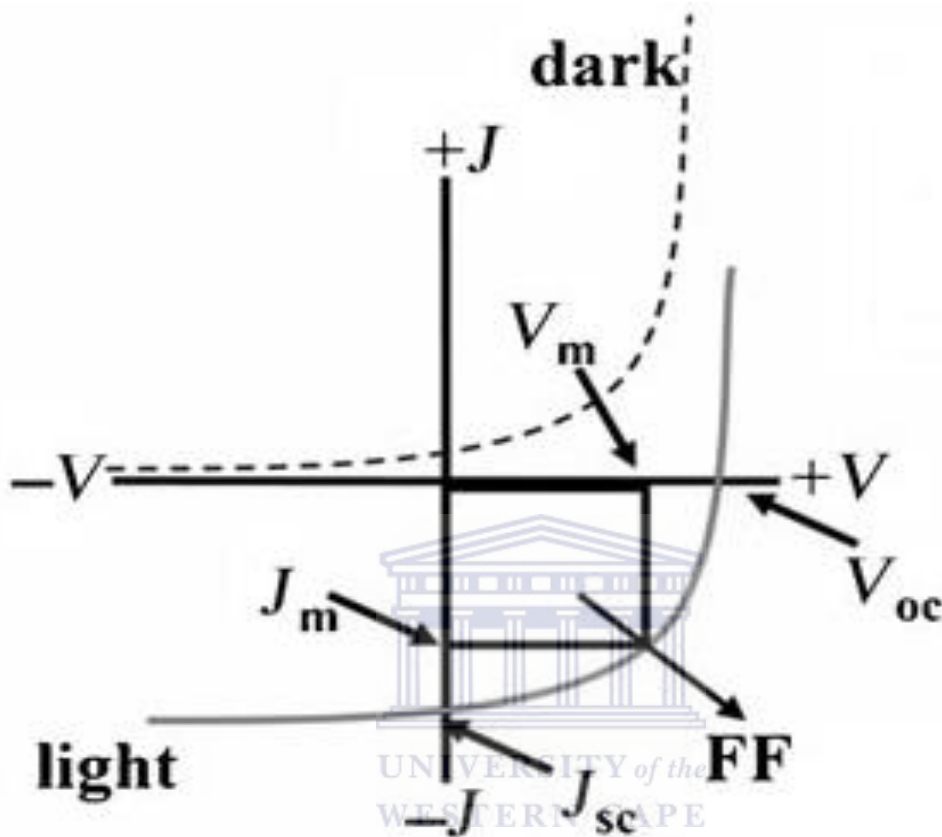


Figure 1.5: Current-Voltage (J-V) curves illustrating parameters of an organic solar cell device [1.46].

1.6.1. Short- circuit current

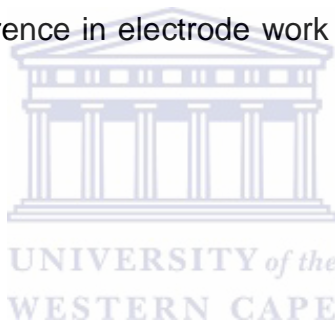
The short circuit current is the photo-generated current of a solar cell, which is extracted at zero applied bias [1.46]. In this case, exciton dissociation and charge transport is driven by the so-called built-in potential. The J_{sc} is heavily dependent on the

number of absorbed photons which originates from two different factors. Firstly, J_{SC} shows a linear dependence on the incident light intensity as long as no saturation effects occur within the active layer. Secondly, J_{SC} can be maximized by enlarging the absorption spectrum of the photoactive layer to harvest more photons within the terrestrial sun spectrum. The J_{SC} also depends on the charge carrier mobilities of the active layer [1.47-1.48].

1.6.2. Open-circuit voltage

The open-circuit voltage is the bias voltage to be applied in order to annihilate the current generated by the illumination. So, at the V_{OC} there is no external current which flows through the device under illumination ($J=0$). For a solar cell with a single conjugated polymer active layer, the V_{oc} scales with the work function difference of the electrodes and thus follow the metal-insulator-metal (MIM) model under consideration of clean polymer/electrode interfaces [1.49-1.50]. Here, clean polymer/electrode interface refers to absence of dipoles or other entities that changes interface conditions, usually resulting in a shift of charge injection barriers. In a single-layer device, the V_{OC} cannot exceed the difference in the work functions of the two electrodes [1.49]. The experimentally determined V_{OC} is generally somewhat lower, owing to the recombination of free charge carriers. At open-circuit conditions, all charge carriers recombine within the photoactive layer. Thus, if recombination can be minimized, the V_{OC} can more closely approach the theoretical limit. However, based on thermodynamic considerations of the balance between photo-generation and recombination of charge

carriers, it has been found that charge recombination cannot be completely avoided, resulting in a lower open-circuit voltage [1.51]. In a bilayer, the V_{oc} scales linearly with the work function difference of the electrodes plus an additional contribution from the dipoles created by photoinduced charge transfer at the interface of the two polymers [1.52]. On the other hand, this does not explain the V_{oc} observed for BHJ solar cells. The V_{oc} of BHJ solar cells mainly originates from the difference between the LUMO of the acceptor [1.53] and the HOMO of the donor [1.54], indicating the importance of the electronic levels of donor and acceptor in determining the efficiency of such solar cells. In the case of polymer-polymer BHJ solar cells, it has been demonstrated that the V_{oc} significantly exceeded the difference in electrode work function with values as large as 0.7 V [1.55, 1.56].



1.6.3. Fill factor (FF)

The purpose of a solar cell is to deliver power. The fourth quadrant of the J-V curve (Figure 1.5) shows the range where the cell can deliver power. In this quadrant, a point can be found where the power reaches its maximum value, called the maximum deliverable power (P_{max}). The fill factor is defined by Equation (1.1), where the abbreviations are as defined previously.

$$FF = \frac{J_m V_m}{J_{sc} V_{oc}} \quad (1.1)$$

The fill factor (FF) is a measure for the characteristics of the solar cell device. The

higher the FF number, the more ideal is the semiconductor. Ideally, the fill factor should be unity, but due to losses caused by transport and recombination its value is generally between 0.2 - 0.7 for OPV devices. The direct relation of FF with current density indicates that it is greatly affected by the mobility of the charge carriers. Moreover, series and shunt resistance are also observed as limiting factors in BHJ solar cells [1.57]. In order to obtain a high fill factor the shunt resistance of a photovoltaic device has to be very large in order to prevent leakage currents, and series resistance has to be very low.

1.6.4. Power conversion efficiency (η)

In order to determine the PCE of a PV device, the maximum power that can be extracted from the solar cell has to be compared to the incident radiation intensity. It is the ratio of delivered power (P_{in}), to the irradiated light power.

$$\eta = \frac{V_{oc} \times J_{sc} \times FF}{P_{in}} \quad (1.2)$$

where η reflects how well the solar cell can convert light into electrical current.

1.7. HYBRID SOLAR CELL MATERIALS

1.7.1. Poly (3-hexylthiophene)

Poly (3-hexylthiophene) (P3HT) is a conjugated polymer, (see figure 1.6). It is a commonly used polymer in organic solar cells and acts as the light absorbing and hole

transporting material. P3HT has a high solubility and a high crystallinity due to the alkyl-groups. Since the thiophene is a 5-membered ring that is polymerised at the 2- and 5-positions, substitution introduces directionality in the polymer which brings about regioregularity [1.58]. The degree of crystallinity is affected by the regioregularity of the polymer. Regioregularity refers to the design of a polymer and the effect of the polymerisation at a particular position. A regioregular P3HT usually has a regioregularity of minimum 90% and the higher the regioregularity, the higher the crystallinity. It was also recognized that higher molecular weight leads to a red shift in the absorption spectrum and to higher hole mobility [1.59-1.60]. P3HT is a conjugated polymer with a thiophene backbone. The carbon atoms in the thiophene rings are sp² hybridized, and thus form a π bond with the neighbor carbon atoms. In the polymer the π band which is called the highest occupied molecular orbital (HOMO). In this π band the electrons are delocalized. The band-gap of thiophenes is built by transition from the aromatic into the quinoid structure. Impurities in the polymer act like a p-type doping and hence enable pure P3HT to be electrically conductive. P3HT is a low band gap polymer with band gap energy of 1.8 eV; low band gap polymers are capable of increasing the efficiency of OPVs, due to a better overlap of the absorption spectrum and the solar spectrum [1.58]. The regioregularity of the polymer structure is of great importance to achieve a low band gap.

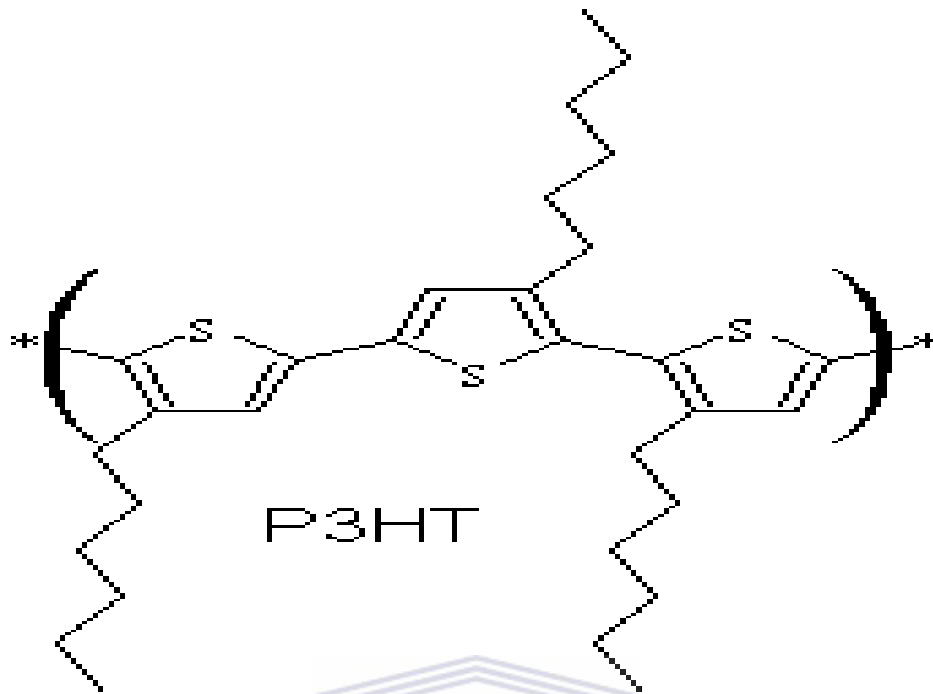
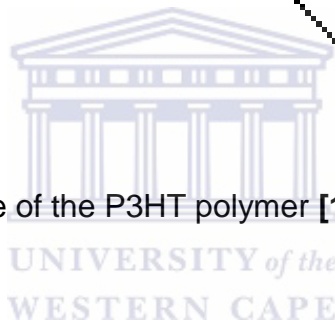


Figure 1.6: Chemical structure of the P3HT polymer [1.58].



1.7.2. Phenyl-C₆₁-butyric acid methyl ester

Phenyl-C₆₁-butyric acid methyl ester (PCBM) is a derivative of a fullerene based molecule (see figure 1.7), used as an acceptor in organic PVs. Fullerenes are very high electron affinity molecules owing to their high energy LUMO, and shows high electron mobility of up to $1\text{cm}^2\text{V}^{-1}\text{s}^{-1}$ in field effect transistors (FETs) [1.61]. The mobility in the PCBM is between 2×10^{-3} and $2 \times 10^{-2} \text{cm}^2/\text{Vs}$. the hole mobility is negligibly small. The HOMO level is 6.1 eV and the LUMO level is 4.4 eV

[1.61]. It also has a π -band, but the electrons are moving in the LUMO. All these fundamental properties contribute positively in the choice of using PCBM as an

accepter material. However, C_{60} molecules have very limited solubility and to make it soluble the methyl-ester group is attached.

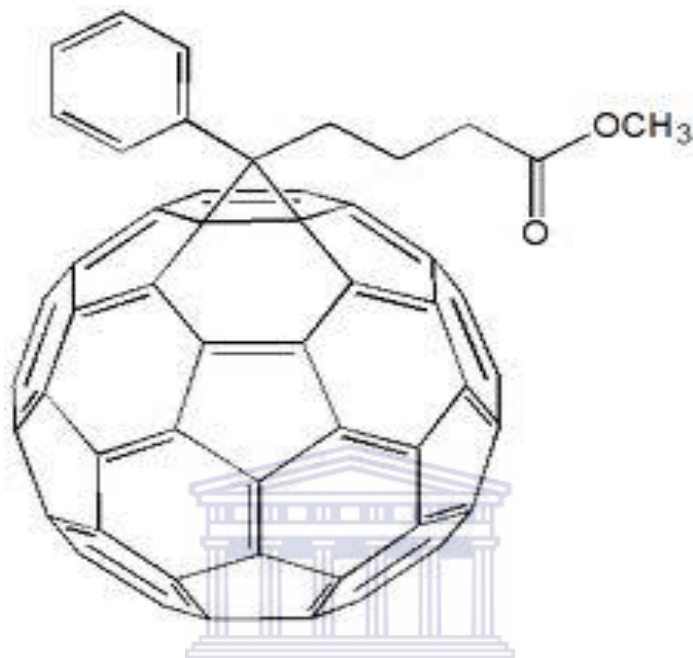


Figure 1.7: Chemical structure of PCBM [1.61].

1.7.3. Zinc Oxide (ZnO)

1.7.3.1. Introduction

Research in ZnO started around the 1930's due to its prospects in optoelectronics applications owing to its direct wide band gap, E_g of 3.3 eV at 300 K [1.62]. Some optoelectronic applications of ZnO overlap with that of GaN, another wide-gap semiconductor ($E_g = 3.4$ eV at 300 K) which is widely used for production of green, blue- ultraviolet, and white light-emitting devices [1.63]. Research peaked around the end of the 1970's and the beginning of the 1980's. The field is fuelled by theoretical

predictions and perhaps experimental confirmation of ferromagnetism at room temperature for potential spintronics application [1.64]. The interest faded away partly because it was not possible to dope ZnO both n- and p-type, which is an indispensable prerequisite for applications of ZnO in optoelectronics [1.65]. Research then moved to structures of reduced dimensionality [1.66]. Zinc oxide nanostructures have been fabricated and proven its versatility and compatibility in numerous applications. ZnO nanostructures were synthesized in the form of nanorods, nanowires, nanotubes, nanobelts, nanocombs, nanosprings and nanorings, etc [1.64-1.66]. The wide interest in ZnO has resulted from the following fundamental characteristic features with potential applications in electronic, structural and bio-materials [1.62]:

- ❖ Direct band gap semiconductor (3.37 eV)
- ❖ Large exciton binding energy (60 meV)
- ❖ Near UV emission and transparent conductivity
- ❖ Bio-safe and bio-compatible

1.7.3.2. Crystal Structure

Most of the group-II-VI binary compound semiconductors crystallize in either cubic zinc-blende or hexagonal wurtzite structure where each anion is surrounded by four cations at the corners of a tetrahedron, and vice versa [1.67]. This tetrahedral coordination is typical of sp^3 covalent bonding, but these materials also have a substantial ionic character. ZnO is an II-VI compound semiconductor whose ionicity resides at the borderline between covalent and ionic semiconductor. The crystal structures shared by

ZnO are wurtzite B4, zinc blende B3, and rock salt B1, as schematically shown in figure 1.8 at ambient conditions, while the thermodynamically stable phase is wurtzite. The zinc-blende ZnO structure can be stabilized only by growth on cubic substrates, and the rock salt NaCl structure may be obtained at relatively high pressures [1.68].

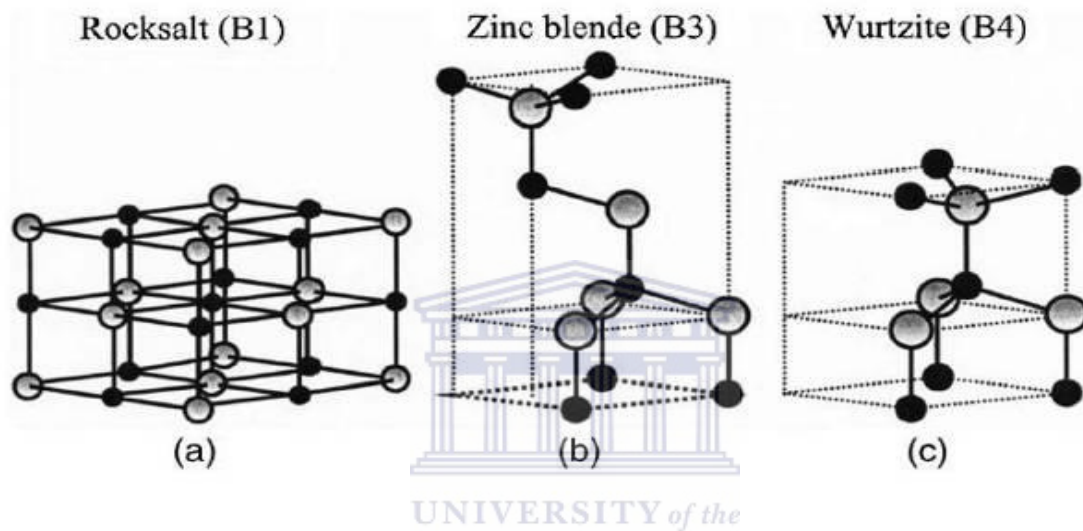


Figure 1.8: Stick and ball representation of ZnO crystal structures: (a) cubic rock salt (B1), (b) Cubic zinc blende (B3) and (c) Hexagonal wurtzite (B4). Shaded gray and black spheres denote Zn and O atoms, respectively [1.68].

Zinc oxide hexagonal wurtzite-type structure has a polar hexagonal axis, the c -axis, chosen to be parallel to z . The primitive translation vectors a and b lay in the x - y plane, are of equal length, and include an angle of 120° , while c is parallel to the z -axis. One zinc ion is surrounded tetrahedrally by four oxygen ions and vice versa. The primitive unit cell contains two formula units of ZnO. The values of the primitive translation vectors are at room temperature $a = b \approx 0.3249$ nm and $c \approx 0.5206$ nm. The ratio c/a of the elementary translation vectors deviates with values around 1.602 slightly from

the ideal value $c/a = 8/3 = 1.633$. In contrast to other Group II-VI semiconductors, which exist both in the cubic zinc-blend and the hexagonal wurtzite-type structures (like ZnS, which gave the name to both structures) ZnO crystallizes with great preference in the wurtzite-type structure. The two latter structures both form a face-centered cubic lattice (FCC), however with different arrangements of the atoms within the unit cell, i.e. different bases [1.68].

1.7.3.3. *Lattice parameters*

The lattice parameters of a semiconductor usually depend on the following factors:

- ❖ Free electron concentration acting via deformation potential of a conduction band minimum occupied by these electrons
- ❖ Concentration of foreign atoms and defects and their difference of ionic radii with respect to the substituted matrix ion
- ❖ External strains (for example, those induced by substrate)
- ❖ Temperature

The lattice parameters of any crystalline material are commonly and most accurately measured by high resolution x-ray diffraction (HRXRD) by using the Bond method for a set of symmetrical and asymmetrical reflections [1.69].

For the wurtzite ZnO, lattice constants at room temperature determined by various experimental measurements and theoretical calculations are in good agreement. The lattice constants mostly range from 3.2475 to 3.2501 Å for the **a** parameter and from 5.2042 to 5.2075 Å for the **c** parameter. The **c/a** ratio vary in a slightly wider range, from

1.593 to 1.6035 .The deviation from that of the ideal wurtzite crystal is probably due to lattice stability and ionicity. It has been reported that free charge is the dominant factor responsible for expanding the lattice proportional to the deformation potential of the conduction-band minimum and inversely proportional to the carrier density and bulk modulus [1.70]. The point defects such as zinc anti-sites, oxygen vacancies, and extended defects, such as threading dislocations, also increase the lattice constant. For the zinc-blende poly-type of ZnO, the calculated lattice constants based on a modern *ab-initio* technique are predicted to be 4.60 and 4.619 Å [1.71].

1.7.3.4. Nano- ZnO Synthesis

There are several methods reported for the synthesis of ZnO nanoparticles, which include chemical vapor deposition [1.72], gas-phase method [1.73], spray pyrolysis, micro emulsion, electrochemical method [1.74], pulsed laser deposition and the sol gel method [1.12, 1.13, 1.75].

The different surface structures of ZnO could induce anisotropic growth on a nanoscale level [1.76]. Under thermodynamic equilibrium conditions, the facet with higher surface energy is usually small in area, while the lower energy facets are larger. Specifically, in the ZnO growth, the highest growth rate is along the c-axis and the large facets are usually 0110 and 2110. By controlling the growth kinetics, it is possible to change the growth behaviour of ZnO nanostructures. Various ZnO nanostructures can be achieved by means of the controllable synthesized parameters, such as deposition

temperatures and pressures as well as carrier gas flux. Such ZnO nanostructures include nanorods, nanobelts, nanocombs, nanohelices and nanorings, etc [1.77]. In this thesis the hydrothermal synthesis method was used as the synthesis method for ZnO because it is a reliable, cheap, simple and a repeatable process [1.78].

1.8. AIMS AND OUTLINE

Research on photovoltaic solar cells has increased over the years and meaningful results have been obtained. Lately organic solar cells have taken the spotlight due to their low-cost, flexibility and their high processing speed. Their power conversion efficiency and stability remains a challenge as compared to the well-established inorganic solar cells based on crystalline silicon (c-Si). Research showed that in organic solar cells the addition of metal-oxide provides a direct and ordered path for photo-generated electrons to the collecting electrode.

The efficiency of OPVs is influenced by a number of factors namely, the choice of polymers, the structure of polymers, the morphology of the thin film and the interfaces between the layers. The stability of the solar cell is important as it determines its functionality to exposure to light or radiation.

In this project poly (3-hexylthiophene) (P3HT) is used as an electron donor and [6,6]-phenyl-C₆₁-butyric acid methyl ester (PCBM), a derivative of the C₆₀ fullerene, as the acceptor material. Zinc oxide is firstly synthesized, characterized and subsequently incorporated into the composite organic material because of its wide-band gap energy and its high electron mobility. The aim is to achieve effective charge transfer at the

interfaces of the active layer of the organic solar cell device. This will be achieved by preparing solutions of 1:1 weight-ratio of P3HT to PCBM, and different ratios of zinc oxide nanoparticles incorporated to form hybrids of ZnO:P3HT:PCBM. After characterization of the hybrid material solar cells will be manufactured and efficiencies calculated to evaluate charge transfer efficiencies.

In chapter 1, the development of photovoltaics over the decades up to hybrid-organic photovoltaics is summarized together with an overview of the basic properties of ZnO, including the crystal structure, lattice parameters and nano-ZnO synthesis.

Chapter 2 focuses on all the analytical techniques that will be used in this study to investigate the material characteristics. The analytical techniques include Thermo gravitational analysis, x-ray diffraction, transmission electron microscopy, scanning electron microscopy, photoluminescence spectroscopy, ultraviolet spectroscopy and Raman spectroscopy. A theoretical background for each analysis technique is discussed.

Chapter 3 will report on the experimental details as well as the results and discussions on the morphological, crystallographic, and optical properties of the synthesized ZnO nanoparticles as inorganic constituent of the hybrid photovoltaic material.

Chapter 4 ultimately reports on the solar cell performance as function of the ZnO concentration in the P3HT-PCBM blend.

Finally, Chapter 5 presents a summary of the main findings.

1.9. REFERENCES

- [1.1] T. Markvart, L. Castaner (Eds.), Solar Cells: Materials, Manufacture and Operation, Elsevier, Oxford, UK, 2005.
- [1.2] A. Goetzberger, J. Knobloch, B. Voss (Eds.), Crystalline Silicon Solar Cells, John Wiley & Sons Ltd., England, 1998.
- [1.3] M. A. Green (Ed.), Silicon solar cells: advanced principles & practice, Centre for Photovoltaic Devices and Systems , Kensington,N.S.W., 1995.
- [1.4] T. Markvart, Light harvesting for quantum solar energy conversion, Prog. Quantum Electronics 24 (2000) 107.
- [1.5] R. B. Bergmann, Crystalline Si thin-film solar cells: a review, Applied Physics A (Materials- Science-Processing) 69 (1999) 187.
- [1.6] R. Schropp, M. Zeman (Eds.), Amorphous and Microcrystalline Silicon Solar Cells: Modelling, Materials and Device Technology" Kluwer, Boston, 1998.
- [1.7] A. Goetzberger, J. Luther, G. Willeke, Sol. Energy Mater.Solar Cells 74 (2002) 1.
- [1.8] Blakers, A., Weber, K. and Everett, V, Chemistry in Australia, 72(1) (2005) 911.
- [1.9] Renewable energy sources and climate change mitigation: special report on inter-governmental panel on climate change, Ipcc (2012)
- [1.10] National Renewable Energy Laboratories (NREL), www.nrel.gov (2005).
- [1.11] University of New South Wales (2008, October 24). Highest Silicon Solar Cell Efficiency Ever Reached. Science Daily, Retrieved April 11, 2010.
- [1.12] Yuwen Zhao, The roadmap of China PV development (2015 & 2020) China Photovoltaic Society 2012
- [1.13] M. A. Green, Prog. Photovolt. Res. Appl. 9 (2001) 287.

- [1.14] Solar Powering Your Community: A Guide for Local Governments, Energy Efficiency and Renewable Energy (2011) 94.
- [1.15] J. J. Dittmer, R. Lazzaroni, P. Leclere, P. Moretti, M. Granstrom, K. Petritsch, E. A. Marseglia, R. H. Friend, J. L Bredas, H. Rost, A. B. Holmes, Solar Energy Materials and Solar Cells 61 (2000) 53.
- [1.16] L.C. Rogers, W.C. O'Mara, R.B. Herring, and L.P. Hunt, Handbook of Semiconductor Silicon Technology, Noyes Publications, New Jersey, USA (1990).
- [1.17] W. Wetling, Sol. Energy Mater. Sol. Cell, 38, (1995)487.
- [1.18] F. Antony, C. Durschner, K-H Remmers, Photovoltaics for professional, Solarpraxis AG, London (2007).
- [1.19] S. E. Shaheen, D. S. Ginley, and G. E. Jabbour. Organic-based photovoltaics: towards low cost power generation. MRS Bulletin, 30 (2006) 10.
- [1.20] M. A. Green, K. Emery, Y. Hishikawa, and W. Warta. Solar cell efficiency tables (version 36). Progress in Photovoltaics: Research and Applications, 18 (2010) 346.
- [1.21] J. Seo, W. J. Kim, S. J. Kim, K.-S. Lee, A. N. Cartwright, P. N. Prasad, Appl. Phys. Lett. 94 (2009) 133302.
- [1.22] M. A. Green, K. Emery, Y. Hishikawa and W. Warta, Solar Cell Efficiency Tables (Version 37), Prog. Photovolt. Res. Appl.19 (2011) 84.
- [1.23] R. Schropp, M. Zeman (Eds.), Amorphous and Microcrystalline Silicon Solar Cells: Modelling, Materials and Device Technology" Kluwer, Boston, 1998.
- [1.24] J. Poortmans, V. Arkhipov (Eds.), Thin Film Solar Cells: Fabrication, Characterization and Applications, John Wiley & Sons Ltd., England, 2006.

- [1.25] Wu X, Kane JC, Dhere RG, DeHart C, Albin DS, Duda A, Gessert TA, Asher S, Levi DH, Sheldon P. 16.5% Efficiency CdS/CdTe polycrystalline thin-film solar cells. Proceedings of the 17th European Photovoltaic Solar Energy Conference and Exhibition, Munich, (2002) 995.
- [1.26] R. Noufi, K. Zweibel (Eds.), High-Efficiency CdTe and CIGS Thin-Film Solar Cells: Highlights and Challenges," IEEE 4th World Conf. on Photovoltaic Energy Conversion, 1 (2006) 317.
- [1.27] Energy Matters. Organic solar cell efficiency record set by konarka. Renewable Energy News, 2010.
- [1.28] Frederik C. Krebs. Polymer Photovoltaics: A Practical Approach. SPIE.Press, Bellingham, Washington, 2008.
- [1.29] M. LoCascio. Application of semiconductor nanocrystals to photovoltaic energy conversion devices. Evident Technologies, Troy, NY, August (2002).
- [1.30] B. R. Saunders, M. L. Turner, Adv. in Colloid and Interface Science 138 (2008) 1.
- [1.31] S. Kumar, G. D. Scholes, Microchim. Acta 160 (2008) 315.
- [1.32]. T. Shiga, K. Takechi, T. Motohiro, Sol. Energy Mater. Sol. Cell, 90 (2006) 1849.
- [1.33] S. Kumar, T. Nann, J. Mater. Res. 19 (2004) 1990.
- [1.34] M. T. Khan, A. Kaur, S K Dhawan and S. Chand, J. Appl. Phys. 109 (2011) 114509.
- [1.35] M. T. Khan, A. Kaur, S K Dhawan and S. Chand, J. Appl. Phys. 110 (2011) 044509.
- [1.36] J. Y. Kim, I. J. Chung, Y. C. Kim, J.-W. Yu, J. of the Korean Phys. Soc. 45 (2004) 231.

- [1.37] Y. Kang, N.-G. Park, D. Kim, Appl. Phys. Lett. 86 (2005) 113101.
- [1.38] M. M. Wienk, M. G. R Turbiez, M. P. Struijk, M. Fonrodona, R. A. Janssen, J. Appl. Phys. Lett. 88 (2006) 153511.
- [1.39] K. Markus, E. Hans-Joachim, D. Gilles, C. S. Markus, J. B. Christoph, S. Pavel, N. H Claudia, Adv. Funct. Mater 20 (2010) 338.
- [1.40] H. Xin, O. G. Reid, G. Ren, F. S. Kim, D. S. Ginger, S. A. Jenekhe, ACS Nano, 4 (2010) 1861.
- [1.41] S. Gunes, N. S. Sariciftci, Inorganica Chimica Acta 361 (2008) 581. [132] A.P. Alivisatos, Science 271 (1996) 933.
- [1.42] G. Li, V. Shrotriya, J. Huang, Y. Yao, T. Moriarty, K. Emery, Y. Yang, Nat. Mater. 4 (2005) 864.
- [1.43] H. Spanggaard, F. C. Krebs, Sol. Energy Mater. & Sol. Cells 83 (2004) 125
- [1.44] U. Rauscher, H. Bassler, D. D. C. Bradley, Phys. Rev. B 42 (1990) 9830
- [1.45] B. C. Thompson, M. J. Frechet, Angew. Chem. Int. Ed. 47 (2008) 58
- [1.47] C. J. Brabec, A. Cravino, D. Meissner, N. S. Sariciftci, T. Fromherz, M. T. Rispens, L. Sanchez, J. C. Hummelen, Adv. Funct. Mater. 11 (2001) 374.
- [1.48] V. D. Mihailetschi, P. W. M. Blom, J. C. Hummelen, M. T. Rispens, J. Appl. Phys. 94 (2003) 6849.
- [1.49] H. Frohne, S. E. Shaheen, C. J. Brabec, D. C. Muller, N. S. Sariciftci, K. Meerholz, Chem. Phys. Chem. 3 (2002) 795.
- [1.50] B.A. Gregg, J. Phys. Chem. B., 107 (2003) 4688.
- [1.51] V. Dyakonov, Physica E, 14 (2002) 53.
- [1.52] I.D. Parker, J. Appl. Phys., 75 (1994) 1656.

- [1.53] J. Liu, Y. Shi, and Y. Yang, *Adv. Funct. Mater* 11, (2001) 420.
- [1.54] H. Kiess, W. Rehwald, *Sol. Energy Mater. Sol. Cells*, 38 (1995) 45.
- [1.55] C. M. Ramsdale, J. A. Barker, A. C. Arias, J. D. Mackenzie, R. H. Friend, and N. C. Greenham, *J. Appl. Phys.* 92 (2002) 4266.
- [1.56] C.J. Brabec, A. Cravino, D. Meissner, N.S. Sariciftci, M.T. Rispens, L. Sanchez, J.C. Hummelen, T. Fromherz, *Thin Solid Films*, 403 (2002) 368.
- [1.57] H. Kim, S.-H. Kim, H. Suh, K. Lee, *Organic Photovoltaics IV*, Eds.: Z.H. Kafafi, P.A. Lane, *Proceedings of SPIE*, SPIE: Bellingham, 5215 (2004) 111.
- [1.58] R. D. McCullough, R. D. Lowe, D. L. Anderson, *J. Org. Chem.* 58 (1993) 904.
- [1.59] A. Zen, J. Paum, S. Hirschmann, W. Zhunang, F. Kaiser, U. Asawapirom, J. Rabe, and D. N. U. Scherf, *Adv. Funct. Mater.* 14 (2004) 757.
- [1.60] P. Schilinsky, U. Asawapirom, U. Scherf, M. Biele, and C. Brabec, *Chem. Mater.* 17 (2005) 2175.
- [1.61] D. Veldman, S. Meskers, and R. Janssen, *Adv. Funct. Material*, 19 (2009) 1939.
- [1.62] C. Klingshirn, *ChemPhysChem* 8 (2007) 782.
- [1.63] C. Klingshirn, *phys. Stat. Sol(B)*, 9 (2007) 3027.
- [1.64] Segets, D. *ACS Nano* 3 (2009) 1703.
- [1.65] T. Bacaksiz, *J. Alloy. Compd.* 466 (2008) 447.
- [1.66] L. Spanhel, M.A. Anderson, *J. Am. Chem. Soc.* 113 (1991) 2826.
- [1.67] Hui Zhang, Xiangyang Ma, Jin Xu, Junjie Niu and Deren Yang, *Nanotechnology* 14 (2003) 423.
- [1.68] M. Riaz, A. Ful, L. L. Yang, O. Nur, M. Willander, and P. Klason: *Journal of Applied Physics*, 18 (2008)

- [1.69] W. L. Bond, Acta Crystallography. 13 (1960) 814
- [1.70] Z. L. Wang, Materials Today 7 (2004) 26.
- [1.71] C. N. R. Rao and A. Govindaraj, in Nanotubes and Nanowires, H. Kroto, P. O'Brien, and H. Craighead, Eds., The RSC Nanoscience and Nanotechnology Series, Royal Society of Chemistry, London, UK, (2005).
- [1.72] D. Sridevi, K. V. Rajendran, Int. J. Nanotechn. Appl., 3(2) (2009) 43
- [1.73] J. Zhou, F. Zhao, Y. Wang, Y. Zhang, L. Yang, J. Lumin, 122 – 123 (2007) 195
- [1.74] Y.L. Zhang, Y. Yang, J.H. Zhao, R. Q. Tan, P. Cui, W.J. Song, J. Sol-Gel Sci Technol,51 (2009) 198
- [1.75] C. Bouvy, W. Marine, R. Sporken, B. L. Su, Chem. Phys. Lett., 428 (2006) 312
- [1.76] AWei, X W Sun,C X Xu, Z L Dong,Y Yang, S T Tan and WHuang, Nanotechnology 17 (2006) 1740–1744
- [1.77] Changle Wu, Xueliang Qiao, Jianguo Chen, Hongshui Wang, Fatang Tan, Shitao Li, Materials Letters 60 (2006) 1828–1832
- [1.78] M. Vafaei, M. Sasani Ghamsari, Mater. Lett., 61 (2007) 3265

CHAPTER 2

ANALYTICAL TECHNIQUES

2.1. INTRODUCTION

The preparation methods for the inorganic material and the organic photoactive blends are described in the results chapters reserved for each respectively. However, analytical techniques are paramount in extracting the relevant information describing the various properties of materials, and therefore this section describes the characterization techniques used to analyze the properties of ZnO, and hybrids of ZnO: P3HT: PCBM. Table 2.1 depicts the different techniques and the information that each technique provides.

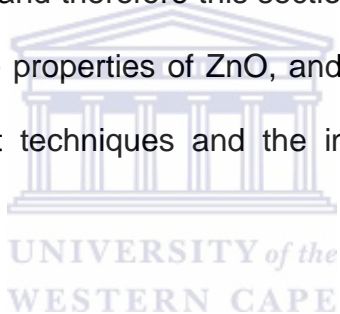


Table 2.1: Analytical techniques used for characterization.

Technique	Property	Information
TGA	Thermal	thermal stability
XRD	Structural	Crystallinity, Grain size and Orientation
HRTEM	Structural	Internal Structure and Particle size
HRSEM- EDS	structural, morphological & chemical	Surface morphology, Elemental Composition
AFM	Morphological	Surface morphology
Raman	vibrational, chemical	Vibrational Structure
FTIR	vibrational, chemical	Chemical Bonding
XPS	Chemical state	Elemental Composition
UV-vis	Optical	Electronic structure and optical properties
PL	Optical	Emission Properties

2.2. X-RAY DIFFRACTION

2.2.1. Introduction

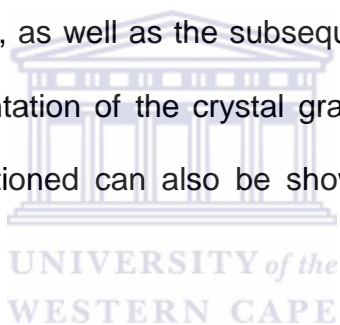
XRD (x-ray diffraction) reveals the structure, crystal orientation and spacing between atomic planes of particles and thin films. X-rays are electromagnetic radiation similar to light, but with much smaller wavelength. X-rays are generated by an x-ray tube, a vacuum tube that uses a high voltage to accelerate the electrons released by a hot cathode to a high velocity. The high velocity electrons collide with a metal target, the anode, creating the x-rays. When the electrons hit the target, x-rays are created by two different atomic processes [2.1]:

X-ray fluorescence: if the electron has enough energy it can knock an orbital electron out of the inner electron shell of a metal atom, and as a result electrons from higher energy levels then fill up the vacancy and x-ray photons are emitted. This process produces an emission spectrum of x-ray frequencies, sometimes referred to as the spectral lines. Usually these are transitions from upper shells into the K shell (called K lines), or into the L shell (called L lines).

Bremsstrahlung: radiation given off by the electrons as they are scattered by the strong electric field near the high-Z (proton number) nuclei. These X-rays have a continuous spectrum.

Diffraction is a phenomenon that occurs when waves interfere with a structure whose reoccurring distance is about the same as that of the incident wavelength. Upon

interaction constructive and destructive interference patterns result due to the scattering of the incoming wave fronts by the structure. The wavelength range of x-rays is about the same as that of the inter-atomic spacing found in three-dimensional crystalline structures, meaning that x-rays can be diffracted by these crystalline structures with each atom in the crystalline structure serving as a scattering center for the incoming wave fronts [2.1]. This phenomenon is known as x-ray diffraction (XRD) and can be used as a tool for the investigation of the fine, crystalline structure of matter. Most important for the purpose of this study are the identification of any crystalline phases present and the determination of the interlayer spacing d in ZnO nanocrystallites and P3HT and its blend with PCBM, as well as the subsequent hybrid mixtures. It can also supply information on the orientation of the crystal grains of the aforementioned. The films produced from aforementioned can also be shown to be polycrystalline, single crystalline or amorphous.



2.2.2. Theory

2.2.2.1. Crystal Structure and Bravais's Lattices

The atoms found in materials can be either randomly distributed, thus making the material amorphous or they can be arranged in a periodic pattern in three dimensions, resulting in the material being crystalline. When thinking about the atomic arrangement within a crystal, it is best to imagine the atoms as a set of imaginary points with a fixed relation in space. Figure 2.1 illustrates the above concept, referred to as a point lattice

and is defined as an array of points in space, so arranged that each point has identical surroundings [2.2].

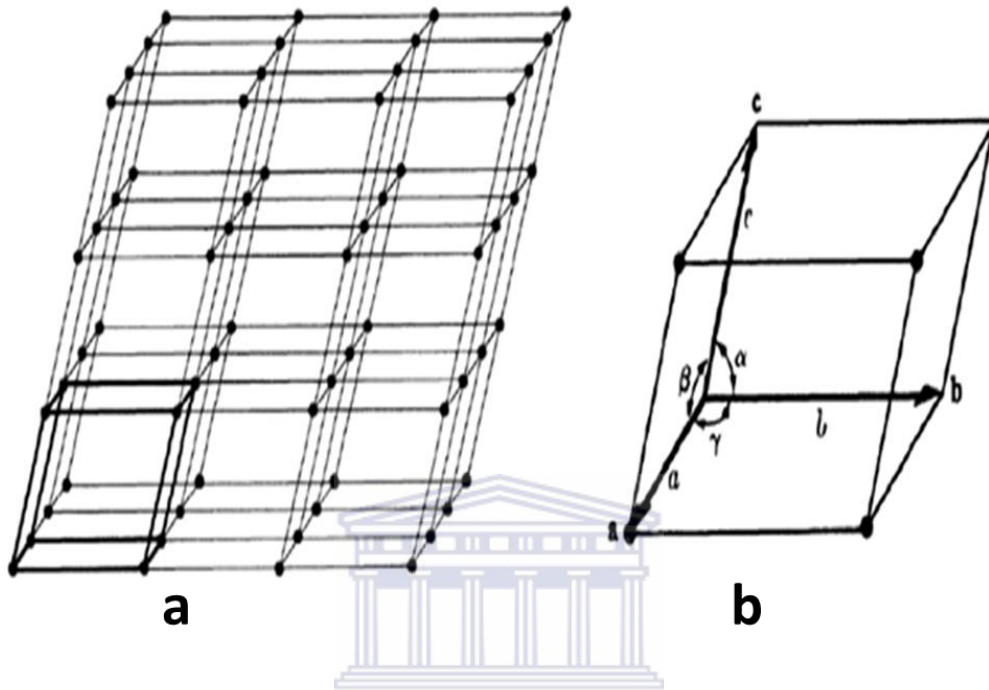


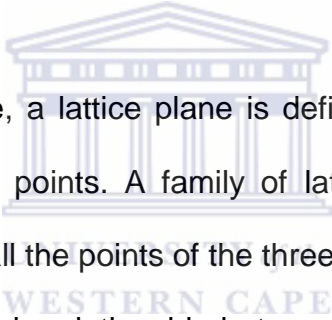
Figure 2.1: Schematic of: (a) its point lattice and (b) primitive cell and the angles between the translation vectors [2.2].

Three vectors a , b and c drawn from any lattice point produces a point lattice unit cell. These vectors, known as the crystallographic axes of the unit cell can also be described in terms of their lengths (a , b and c) and the angle between them (α , β and λ), known as the lattice constants or lattice parameters, as shown in Figure 2.1. Not only do the crystallographic axes define the unit cell, but it also defines the whole point lattice, which can be produced by repeated action of the vectors. Depending on the relationship between the lattice parameters (i.e. a , b , c , α , β and λ) one can distinguish between fourteen different point or Bravais lattices, as described in Table 2.2. The direction of

any vector within the Bravais lattice is given as a linear combination of the three crystallographic axes as:

$$\mathbf{x} = u\mathbf{a} + v\mathbf{b} + w\mathbf{c} \quad (2.1)$$

where \mathbf{a} , \mathbf{b} or \mathbf{c} is any vector in the Bravais lattice and u , v and w are the coordinates of any point on the vector. In short, equation (2.1) can be written as $[u \ v \ w]$. However, $[u \ v \ w]$ are always converted to a set of smallest integers, e.g. $[2 \ 2 \ 4]$ and $[\frac{1}{2} \ \frac{1}{2} \ 1]$ represents the same direction, with $[1 \ 1 \ 2]$ the preferred notation. Collectively, all of these vectors form the reciprocal space of the lattice, or reciprocal lattice.



Given any Bravais lattice, a lattice plane is defined as any plane containing at least three non-collinear lattice points. A family of lattice planes is a set of parallel planes, which together contain all the points of the three-dimensional Bravais lattice. For cubic systems, there is an intrinsic relationship between the family of lattice planes and the vectors in the reciprocal lattice, which provides a convenient way of specifying the orientation of the lattice planes in space.

Table 2.2: Description of the fourteen Bravais lattices [2.2].

	Axial length and angles	Bravais lattice
Cubic	Three equal axis at right angles $a = b = c, \alpha = \beta = \gamma = 90^\circ$	Simple Body-centered Face-centered
Tetragonal	Three angles at right angles, two equal $a = b \neq c, \alpha = \beta = \gamma = 90^\circ$	Simple Body-centered
Orthorhombic	Three unequal axis at right angles $a \neq b \neq c, \alpha = \beta = \gamma = 90^\circ$	Simple Body-centered Face-centered Base-centered
Rhombohedral	Three equal axes, equally Inclined $a = b = c, \alpha = \beta = \gamma \neq 90^\circ$	Simple
Hexagonal	Two equal co-planar axes at 120° , third axis at right angles $a = b \neq c, \alpha = \beta = 90^\circ, \gamma = 120^\circ$	Simple
Monoclinic	Three unequal axes, one pair not at right angles $a \neq b \neq c, \alpha = \gamma \neq 90^\circ \neq \beta$	Simple Base-centered
Triclinic	Three unequal axes, unequally inclined and none at right angles $a \neq b \neq c, \alpha \neq \beta \neq \gamma \neq 90^\circ$	Simple

2.2.2.2. Bragg's Law of Diffraction

The basis for x-ray diffraction is described by the Bragg equation. Bragg discovered that diffraction could be pictured as a reflection of the incident beam from the lattice planes, and subsequently developed a mathematical equation for the condition of reflection, which is equivalent to simultaneously solving the three Laue equations. This provides for a simpler and more workable expression of diffraction [2.3]. A beam of parallel X-rays penetrating a stack of planes of spacing d can be considered, at a glancing angle θ as depicted in figure 2.2. Each plane must be considered as reflecting a fraction of the incident beam [2.3].

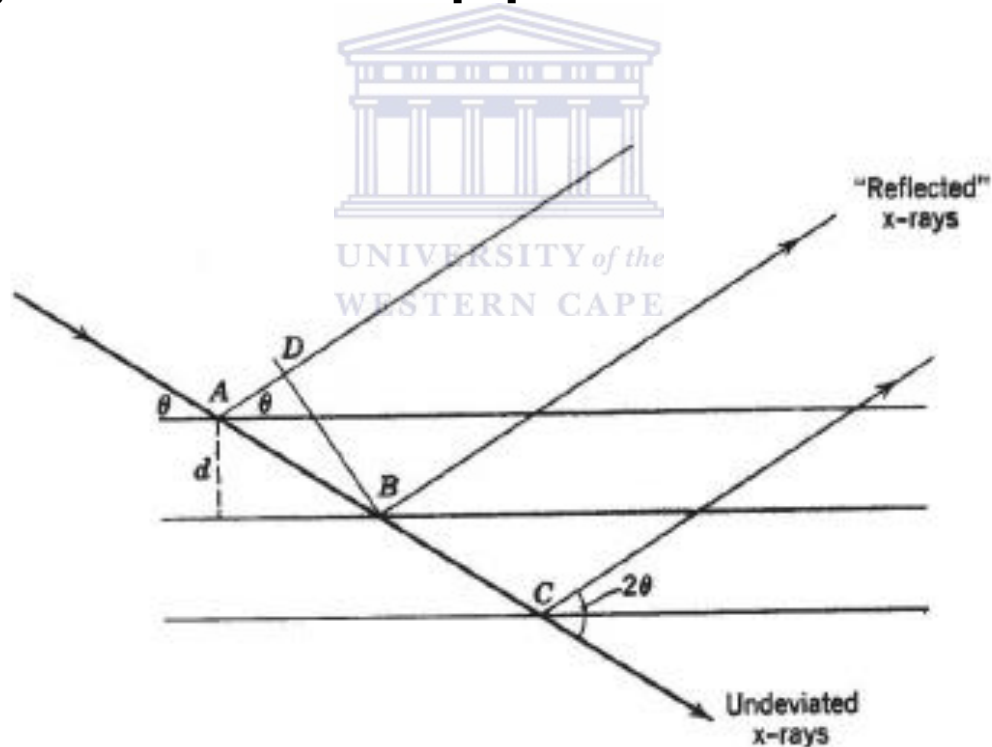


Figure 2.2: Schematic depiction of the condition of reflection for Bragg's law [2.3].

The reflected rays combine to form a diffracted beam if they happen to be in phase by an integer number of wavelengths – that is, if their path difference $AB - AD = n\lambda$, where $n = 1, 2, 3$.

AB and AD is given by:

$$AB = \frac{d}{\sin\theta}$$

and

$$AD = AB\cos 2\theta = \frac{d}{\sin\theta}(\cos 2\theta).$$

Therefore:

$$n\lambda = \frac{d}{\sin\theta} - \frac{d}{\sin\theta}(\cos 2\theta) = \frac{d}{\sin\theta}(1 - \cos 2\theta) = \frac{d}{\sin\theta}(2\sin^2\theta)$$

leading to

$$\therefore n\lambda = 2d\sin\theta \quad . \quad (2.2)$$

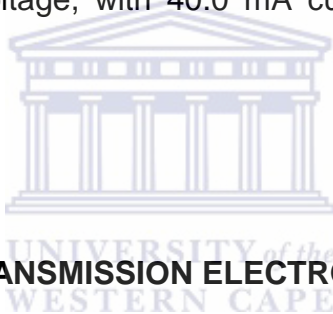
This is the Bragg condition for reflection **[2.3]**. The equation gives the angle θ , at which a set of planes of spacing d constructively reflects x-radiation of wavelength λ in the n^{th} order.

The interplanar spacing d , of a set of parallel crystallographic lattice planes, is defined by the dimensions of the crystal unit cell. There exist an infinite number of such families of parallel planes in a given crystalline lattice, and each is associated with a particular Bragg angle θ , as indicated in Figure 2.2. Each set of planes is characterized

by the three Miller indices hkl , and the resultant diffracted beam is termed the hkl miller indices.

2.2.3. Experimental set-up

X-Ray diffraction patterns were obtained at the CSIR, Pretoria, South Africa, by means of the reflection geometry of a PANalytical X'pert Pro PW3040/60 X-Ray diffractometer. The system was operated with a $\text{CuK}\alpha$ ($\lambda = 1.54060 \text{ \AA}$) monochromated radiation source at 45.0 kV voltage, with 40.0 mA current, to investigate the crystal structure of the nanoparticles.



2.3. HIGH RESOLUTION TRANSMISSION ELECTRON MICROSCOPY

2.3.1. Introduction

Transmission Electron Microscopy (TEM) has become a mainstay in the repertoire of characterization techniques for materials scientists, especially nowadays that nanoscale research demands high resolution imaging. TEM is a microscopy technique in which a beam of highly energetic electrons is focused on a specimen and an enlarged image appear on a fluorescent screen, photographic film, or computer screen. The image gives information about the surface of the specimen, the shape of

the specimen, the size of the particles, and importantly, the crystallographic information of the material.

2.3.2. Theory

2.3.2.1. Basic operation

A basic TEM consists of an electron gun which provides electrons, a series of electromagnetic lenses, a viewing screen coated with a layer of electron-fluorescent material, and a camera which must work in the vacuum within the microscope [2.4]. These components are assembled into a vertical 'microscope column'. A typical example is shown in Figure 2.12. The electron gun emits a diverging beam of electrons through the anode aperture. This beam can be deflected to be aligned parallel to the optical axis of the lens system. The deflector coils are controlled by the gun alignment controls, and the electron beam is focused down to a fairly small spot by the first condenser lens. The setting of this lens controls the ultimate spot size attainable by the condenser system, which is generally less than 1 μm . The second condenser lens projects the beam at the specimen in such a way that the area illuminated and the convergence angle can be controlled. Below this lens is a moveable aperture that selects the primary beam and cut out any scattered beams, thus giving a clear diffraction image. The best resolution and image sharpness is obtained by working with the smallest condenser lens aperture (<300 μm) while exiting the second condenser lens more strongly. However, this reduces the illumination level considerably.

The condenser stigmator placed below the condenser aperture compensates for astigmatism in the illumination system. In this same region are the 'wobbler' coils for aiding focusing and two sets of alignment coils in order to bring the beam exactly onto the optical axis in the crucial part of the microscope near the specimen. The specimen, objective aperture and objective stigmator coils are all placed inside the objective lens windings. The objective lens focuses on the specimen and forms an intermediate image at a magnification of about 50X. The objective aperture sits in the 'back focal plane' of the objective lens and enables the operator to allow particular groups of electrons to contribute to the final image. In the plane of the first intermediate image is the 'selected area' aperture, which allows a particular part of the image to be selected for examination and diffraction analysis. Below this aperture are three or four lenses whose function is to magnify the image or diffraction pattern and project it into the fluorescent screen. The electronics needed to control the electron gun, six or seven lenses and a vacuum system is quite complex. For this reason there is a tendency for modern electron microscopes to be controlled by a built-in computer, which results in a reduction in the number of manual controls.

For an electron beam incident on a specimen, each electron passing through the specimen has a number of possible fates **[2.4]**:

- (i) It is undeflected.
- (ii) It is deflected but loses no energy.
- (iii) It loses a significant amount of energy and is probably deflected.

The above processes contribute to the output image and all regions of the specimen will look the same. In order to create contrast in the image the scattered electrons must be separated from the unscattered electrons using the objective lens aperture.

In Figure 2.3, the fate of 100 electrons falling on a model specimen is illustrated. The numbers shows the electrons scattered through more than 0.5° and those of the unscattered electrons. Region (a) consists of 10 nm amorphous carbon, which is a light atom. Only 9 of the 100 electrons are weakly scattered and will be deflected by 0.5° or more. Region (b) is an area of twice the thickness and scatters slightly more strongly and only 17 electrons are significantly deflected. Region (c) is the same thickness as (b) but consists of amorphous lead, which is a very heavy atom; here the majority of electrons are deflected but through a small angle. Region (d) consists of the same thickness of crystalline lead. In this region diffraction can take place and the scattered electron beam will be reinforced in a certain direction, resulting in most of the scattered electrons traveling in specific directions at the Bragg angle θ_B to the unscattered beam.

When all 100 electrons achieve consent to travel down the microscope, the image produced by the lenses will be the same in regions (a), (b), (c) and (d), and thus there will be no contrast. If all the electrons that have been scattered through 0.5° by insertion of an aperture below the specimen are stopped as shown in (e), then regions (a) - (d) will look quite different. The brightness of the image of each region will be proportional to the number of unscattered electrons which pass through the aperture, so regions (a), (b), and (c) will appear to have brightness in the ratio 91:83:4. The lead will

appear dark, whereas thickness variations in the carbon regions will only give faint contrast [2.5].

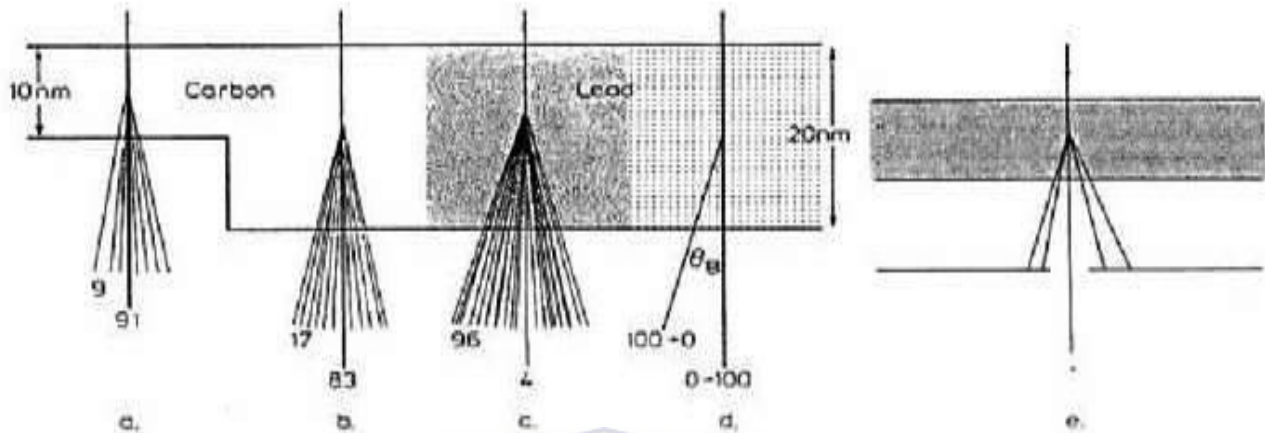


Figure 2.3: Schematic illustrating fate of 100 electrons falling on four different regions of a hypothetical specimen [2.5]. The different regions are: (a) 10 nm of amorphous carbon; (b) 20 nm of amorphous carbon; (c) 10 nm of amorphous lead; (d) 20 nm of crystalline lead; (e) the effect of inserting an objective aperture to stop all electrons scattered through an angle greater than 0.5° .

2.3.2.2. Electron diffraction

Common to all electron microscopes, a diffraction pattern of crystalline specimens inevitably forms in the back focal plane of the objective lens. In this plane all parallel 'rays' leaving the specimen in a specific direction pass through a point in the 'diffraction pattern' [2.5].

During normal imaging the diffraction pattern is unseen because the first intermediate lens is focused on the first intermediate image (Figure 2.4) and this is what is finally projected onto the screen. In diffraction mode the first intermediate lens is reduced so that it 'sees' the diffraction pattern in the back focal plane of the objective lens and projects magnified versions of this pattern instead to the projector system. There are two fundamentally different ways of examining the diffraction pattern from a selected area of the specimen. In the selected area diffraction technique a small area of the specimen is selected, although a larger area is being illuminated. In the alternative micro-diffraction technique the beam is condensed into a small spot so that the diffraction pattern comes from the whole of the (small) illuminated area. In this case the diameter selected on the specimen is the same as the diameter of the beam at the specimen. This is the only way to obtain a diffraction pattern from a region smaller than $1\ \mu\text{m}$ in diameter (down to a few nanometers). A diffraction pattern is obtained when the electron beam encounters crystalline material, resulting in strong preferential scattering in certain well-defined directions governed by Bragg's Law (equation 2.2) **[2.6]**.

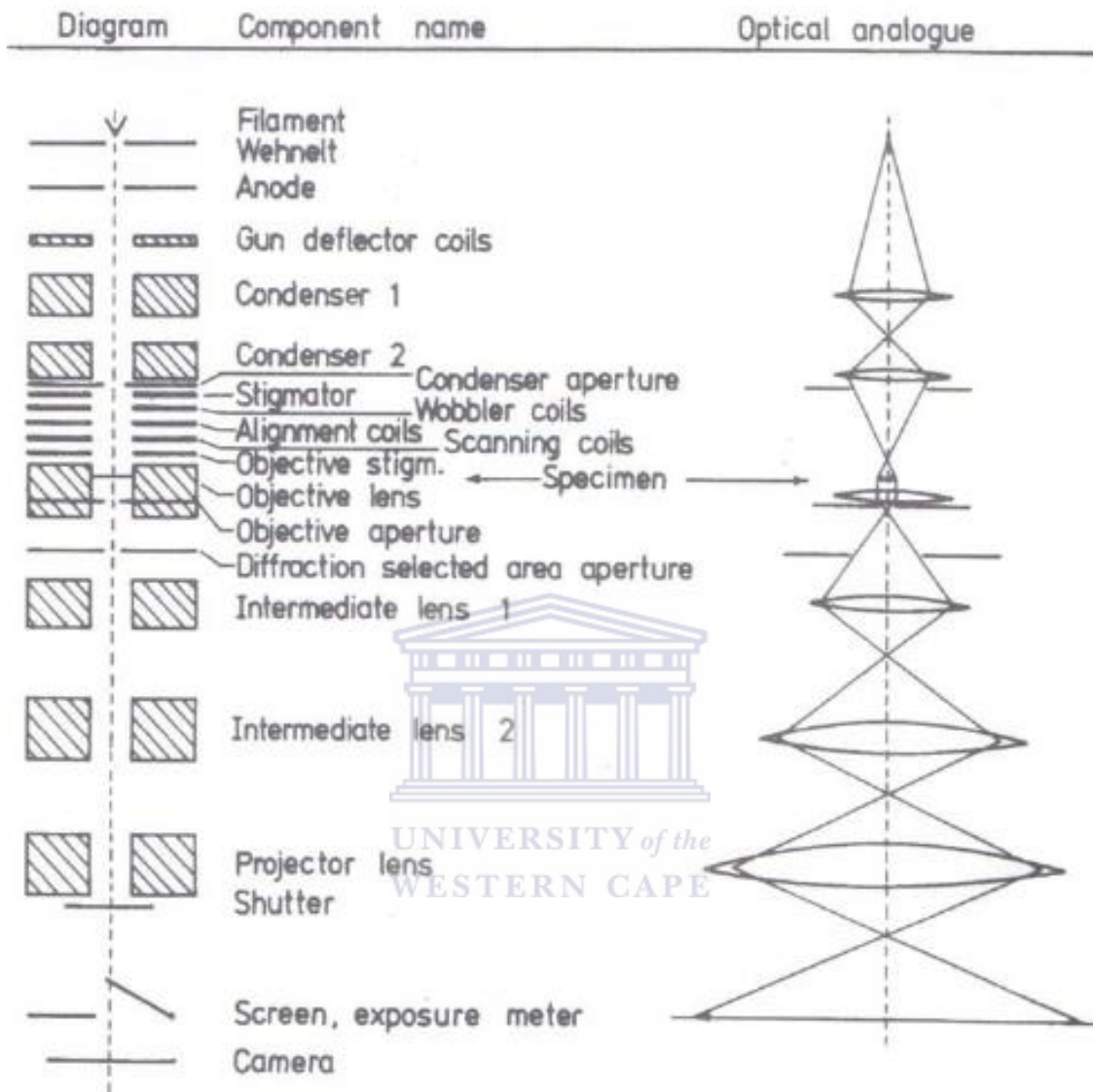
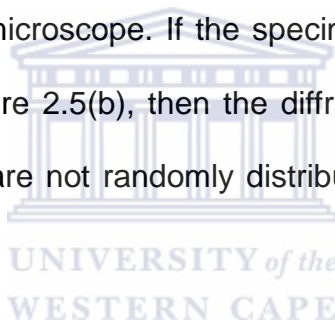


Figure 2.4: A cross-section of the basic components of HR-TEM. The optical analogue is also provided [2.6].

The Bragg condition is said to be satisfied when a crystal is orientated in such a way that the incident electron-beam satisfies the diffraction angle for the specific plane. Since most of the diffracted electrons are concentrated in these Bragg directions, a

crystal grain will appear bright if the diffracted beams pass through the objective aperture, and dark if stopped by the objective aperture. Thus, in a polycrystalline material some grains will appear bright and some dark, depending on their orientation with respect to the electron beam (see for example figure 2.5(b)). Different types of diffraction patterns arise from different specimen microstructures, as can be seen in Figure 2.5(a). The figure shows a single crystal (i.e. a specimen consisting of a single repeating array of atoms) orientated in such a way that several sets of planes are parallel to the beam. This gives rise to a diffraction pattern consisting of a regular array of bright spots. The arrangement of these spots depends upon the orientation of the atomic planes in the electron microscope. If the specimen contains several crystals of different orientations as in Figure 2.5(b), then the diffraction pattern is the sum of the individual patterns. The spots are not randomly distributed, but tend to fall on rings of constant radii.



If the specimen consists of a large number of small crystallites (grains) of similar crystal structure, but at different orientations to one another (i.e. a polycrystal as in Figure 2.5(c)) the diffraction pattern will consist of a series of sharp concentric rings. It can easily be seen that this pattern evolves from a large number of single crystal diffraction patterns, each rotated by a small amount with respect to one another. In the case of an amorphous material, the constituent atoms are arranged entirely randomly and without any distinct repeating structure. For such materials the diffraction pattern will contain no discrete maxima. It rather consists of diffuse diffraction rings around the bright central spot of unscattered electrons.

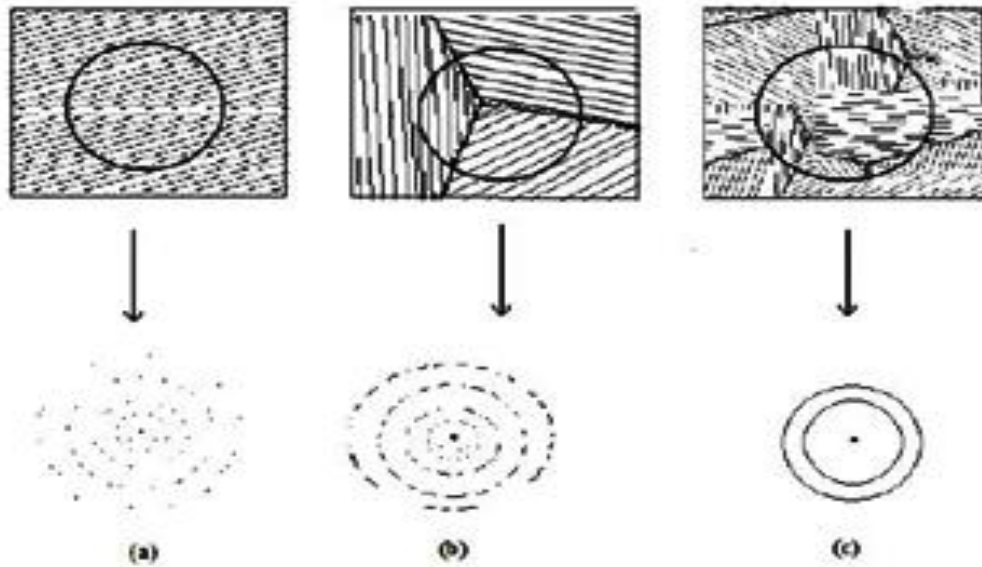


Figure 2.5: Types of diffraction pattern which arise from different specimen microstructure: (a) a single perfect crystal, (b) a small number of grains – notice that even with three grain spots circles begin to form, (c) a large number of randomly orientated grains, the spots have now merged into rings [2.6].

Using the standard Miller index notation to define planes and directions in the crystal, diffraction patterns can be interpreted. Using this notation for a cubic crystal for example the spacing of planes of the type (hkl) is given by:

$$d_{hkl} = \frac{a}{\sqrt{h^2+k^2+l^2}}, \quad (2.3)$$

where a is the lattice parameter of the unit cell and h, k and l the Miller indices.

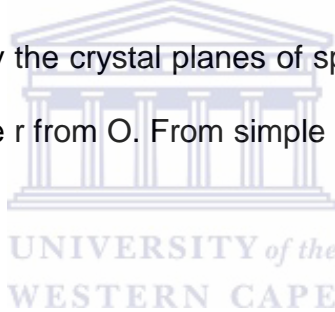
For first order diffraction i.e. $n = 1$, Bragg's law $n\lambda = 2d\sin\theta$ reduces to:

$$\lambda = 2d\sin\theta . \quad (2.4)$$

For small angles of θ , which is typical of electron diffraction, we can write $\sin \theta = \theta$, and equation (2.4) further reduces to:

$$\lambda = 2d\theta . \quad (2.5)$$

Consider now a beam of electrons impinging on a crystalline specimen as in figure 2.6. Some of the electrons pass through the specimen without interaction and hit the screen or film, which is a distance L from the specimen, at O . Other electrons are diffracted through an angle θ by the crystal planes of spacing d , and these electrons hit the film at A , which is a distance r from O . From simple geometry, it can be seen that for small angles of diffraction:



$$\frac{r}{L} = 2\theta . \quad (2.6)$$

Combining equations (2.5) and (2.6), we find:

$$rd = L\lambda . \quad (2.7)$$

$L\lambda$ is called the camera constant and is determined by analyzing a known crystal. From equation (2.7) it can be seen that the distance of a diffraction spot from the undiffracted spot, r , is therefore inversely proportional to the d -spacing of the diffracting planes. A table of the $L\lambda/dhkl$ values for different (hkl) planes can be drawn up. By measuring r directly in the pattern on the photographic plate and comparing it with the

values in the table, the pattern can be indexed, i.e. the respective h , k and l values can be determined [2.7].

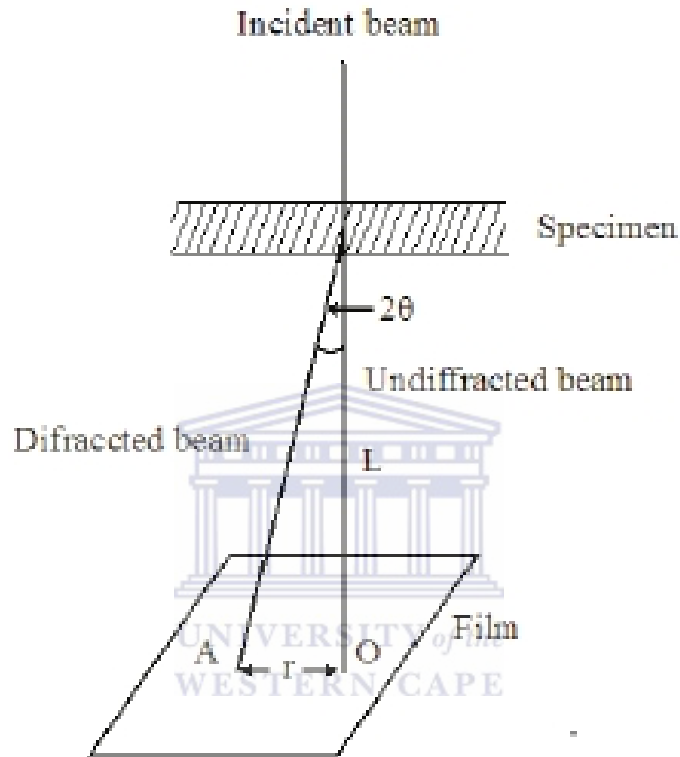


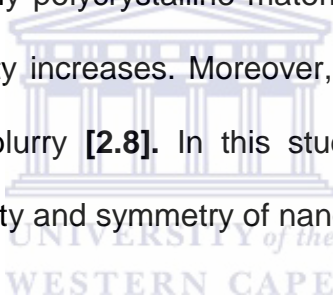
Figure 2.6: Schematic diagram showing the geometry of diffraction pattern formation [2.7].

The high-resolution transmission electron microscope (HR-TEM) has the edge over other conventional low-resolution transmission electron microscopes because it provides excellent analytical performance pertaining to nanoscale imaging for daily use in a multi-user environment. Moreover, the configuration of the instrument is easy to

operate combined with the capabilities for routine atomic resolution imaging of crystal lattices by coherent electron scattering [2.7].

2.3.2.3. Selected area electron diffraction

Selected area electron diffraction (SAED) can be used in the qualitative measure of crystallinity and symmetry of materials. In SAED, the electrons are scattered by electric fields associated with atoms in thin film sample. Diffraction patterns produced give single crystal diffractive contributions from multitudes of crystallographic arrangements. In addition, highly polycrystalline materials may become more complex as the degree of polycrystallinity increases. Moreover, amorphous materials results in patterns that are diffused or blurry [2.8]. In this study, SAED is limited to a rapid qualitative measure of crystallinity and symmetry of nanoparticles.



2.3.3. Experimental set-up

High resolution transmission electron microscopy (HR-TEM) was used to study the crystallinity and internal structure of the ZnO nanostructures. An FEI Tecnai G²20 FEG-TEM operated at 200kV in bright-field mode was used to capture high resolution images; whereas parallel beam selected area electron diffraction (SAED) patterns were used to study the crystallinity of the nanomaterials.

2.4. HIGH RESOLUTION SCANNING ELECTRON MICROSCOPY

2.4.1. Introduction

A Scanning Electron Microscope (SEM) is a type of electron microscope that allows for the observation and characterization of heterogeneous organic and inorganic materials on the nanometer (nm) to micrometer (μm) scale. It images the sample surface by scanning it with a high-energy beam of electrons in a raster scan pattern. The electrons interact with the atoms of the sample and produce signals that contain information on the sample's topography, composition and other properties such as electrical conductivity. The signals produced when an electron beam interacts with the samples are secondary electrons (SE), backscattered electrons (BSE), characteristic X-rays, cathodoluminescence, specimen current and transmitted electrons (see figure 2.7)

[2.9].

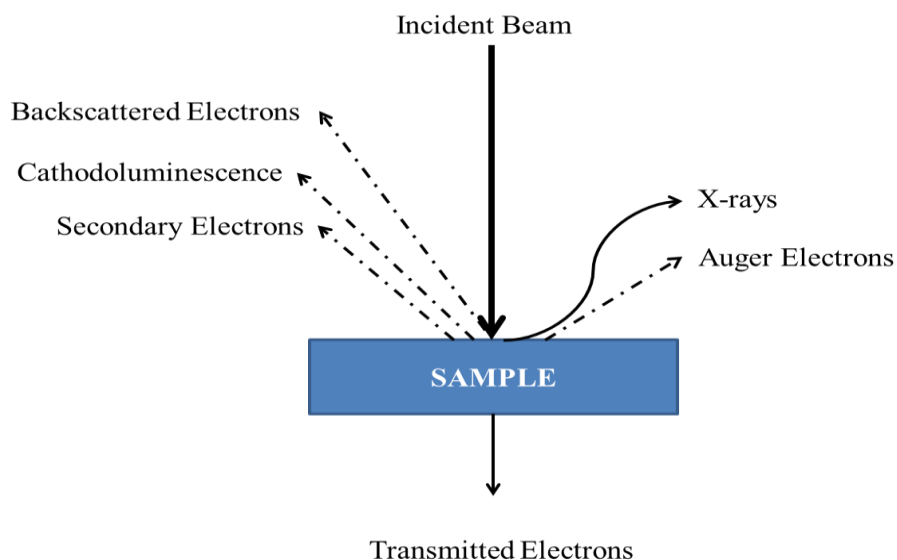


Figure 2.7: Schematic diagram of the signals generated during the incident beam – sample interaction [2.9].

2.4.2. Theory

2.4.2.1. Resolution

The resolution can be defined as the closest spacing of two objects which can be viewed through the microscope to be separate entities. Obtaining images at high magnifications without adequate resolution is not a desired result when operating the SEM since no additional valuable information can be obtained from the images. Mathematically, the limit of resolution, which is the smallest spacing at which two objects are resolved, can be described by Abbe's equation [2.10].


$$r = \frac{0.612\lambda}{n\sin\alpha}, \quad (2.8)$$

where r is the limit of resolution, λ is the wavelength of the incident beam, n is the refractive index of the medium between the object and the objective lens, and α is the aperture angle. The best resolution (i.e. the smallest r) can be achieved by decreasing λ or increase n or α .

2.4.2.2. Depth of field and working distance

The depth of field (DOF) can be referred to as the range of positions for the objects at which our eye cannot resolve a change in the sharpness of the image. The working distance in the SEM can be defined as the distance between the final condenser lens pole and the top part of the specimen [2.10]. It influences the depth of field for certain samples. A long working distance decreases the angle of the aperture,

resulting in greater depth of field, whereas a shorter working distance results in the sample being scanned with a wider angle (aperture solid angle, α); see figure 2.8

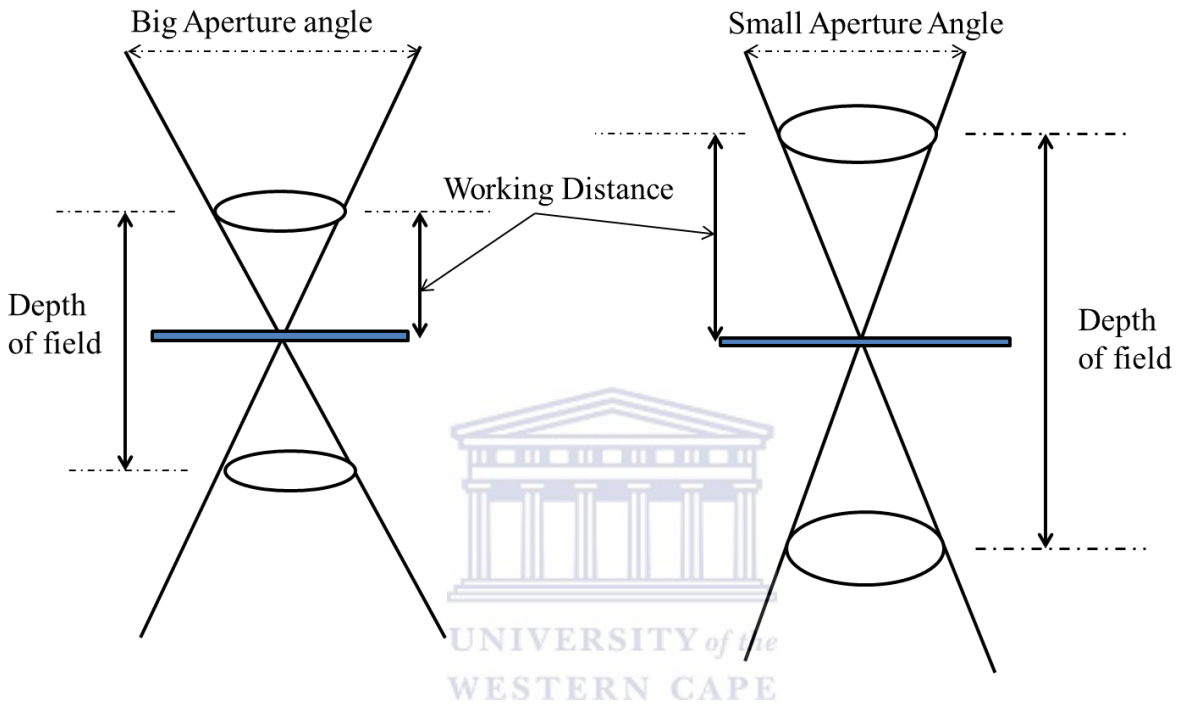


Figure 2.8: The effect of the working distance on the depth of field seen for the specimen [2.10].

The working distance also affects the spherical aberration of the imaging system which in turn influences the resolution of the final image. The spherical aberration results from the geometry of the electromagnetic lenses, which happen when electrons that are near to the beam axis refract less than one focal point, therefore resulting in an enlarged and non-focused spot. Decreasing the working distance reduces the spherical aberration, resulting in a smaller but more focused beam spot, which in turn yields an improved resolution for the final image [2.10].

2.4.2.3. Secondary electrons

When an incident electron beam interacts with a sample, the strongest region of the electron energy spectrum is due to secondary electrons (SE). The secondary electrons are produced when an incident electron excites the specimen electron and loses some energy in the process. The excited electron will undergo elastic and inelastic collisions as it moves towards the surface and it will escape the surface if it still has sufficient energy. Their energies are a function of E_0 and work function (E_w), which determines the amount of energy required to remove electrons from the surface of materials. Coating a non-conductive specimen with a carbon, gold or gold-palladium layer maximizes the number of secondary electron emissions. As illustrated in figure 2.9, secondary electrons are emitted in energies less than 20 keV. It represents a small fraction of the electrons emitted from the sample [2.11].

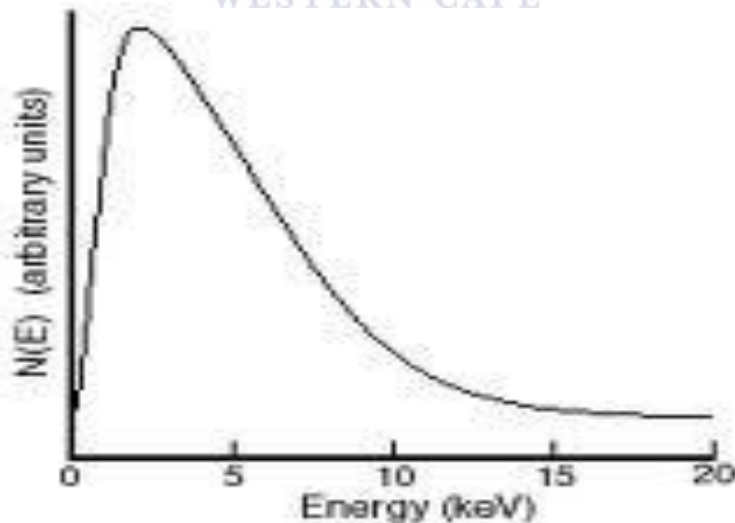


Figure 2.9: Energy distribution of secondary electrons [2.11].

In many materials the mean free path of secondary electrons is approximately 10 Å. Even though electrons are generated throughout the excited region by the incident beam, only electrons that originate within 10 Å when escaping the specimen will be detected as secondary electrons. The interaction volume is very small compared to BSE and X-rays. As a result SE gives a better resolution than BSE or X-rays and is effectively the same as the electron beam size [2.11].

2.4.2.4. Effect of accelerating voltage

For low accelerating voltages (5 kV), the beam interaction with the specimen is in regions close to the surface. It gives detailed information of the surface compared to the images obtained at higher accelerating voltages (15-20 kV), in which the beam penetrates beneath the specimen surface, revealing the information about the interior of the sample [2.12].

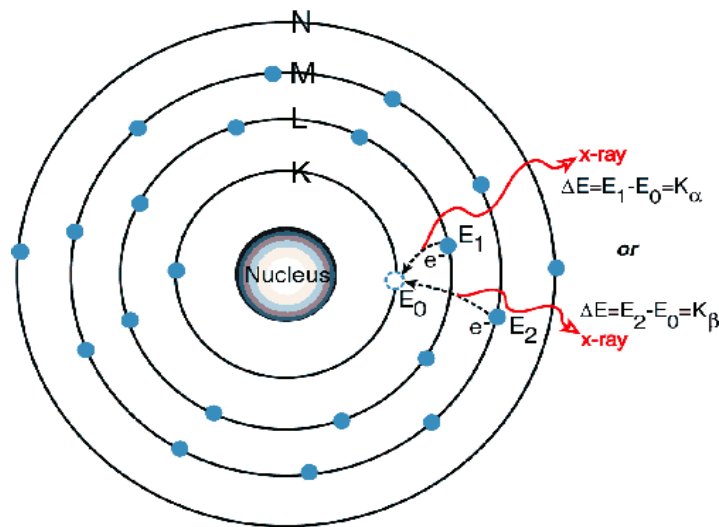
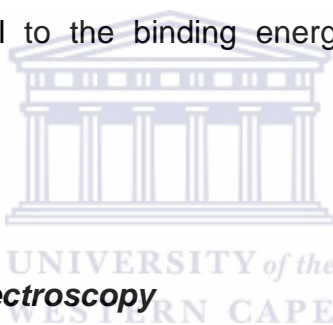


Figure 2.10: Characteristic x-ray emission by an atom [2.12].

When an inner shell electron is excited to leave an atom or to go into a higher unoccupied level, characteristic X-rays are emitted. The electron will be replaced by one of the outer shell electrons conserving energy by emitting an X-ray photon. If an electron is removed from the K-shell (1s) it can be replaced by an electron from either 2p, 3p or any higher occupied state. The transition energy will be released as X-radiation and the emission lines labeled as K_{α} , K_{β} , etc [2.13]. The X-ray emission for any specimen can provide an analysis of specimen elements constituents, normally in the regions of $1\mu\text{m}$ diameter and $1\mu\text{m}$ depth under normal operating conditions. The K_{α} and K_{β} lines have the highest energy X-ray photons from each atom because the energy is nearly closely equal to the binding energy of the 1s electron (see the representation in figure 2.10).



2.4.2.5. Energy dispersive spectroscopy

Energy Dispersive Spectroscopy (EDS) makes use of the X-ray spectrum emitted by a solid sample bombarded with a focused beam of electrons to obtain a localized chemical analysis. All elements from atomic number 4 (Be) to 92 (U) can be detected in principle, though not all instruments are equipped for 'light' elements ($Z < 10$). Qualitative analysis involves the identification of the lines in the spectrum and is fairly straightforward owing to the simplicity of X-ray spectra. Quantitative analysis (determination of the concentrations of the elements present) entails measuring line intensities for each element in the sample and for the same elements in calibration standards of known composition. [2.14]

By scanning the beam in a television-like raster and displaying the intensity of a selected X-ray line, element distribution images or 'maps' can be produced. Also, images produced by electrons collected from the sample reveal surface topography or mean atomic number differences according to the mode selected. Scanning electron microscopy, which is closely related to the electron probe, is designed primarily for producing electron images, but can also be used for element mapping, and even point analysis, if an X-ray spectrometer is added. There is thus a considerable overlap in the functions of these instruments [2.15].

High resolution scanning electron microscope (HR-SEM) brings some advantages over low-voltage SEM. For example, the (field-emission gun) FEG-SEM is capable of producing high primary electron brightness and small spot size even at low accelerating potentials [2.15]. HR-SEM is equipped with charge compensation (CC) used for viewing uncoated, non-conducting specimens. Moreover, HR-SEM has plasma cleaning (PC) which is only used *in situ* in the HR-SEM, but can be applied to all specimens *ex situ*. The advantage of PC is that it can be used to clean special surfaces after contamination build-up. Contamination free surfaces are vital for HR-SEM work.

2.4.3. Experimental set-up

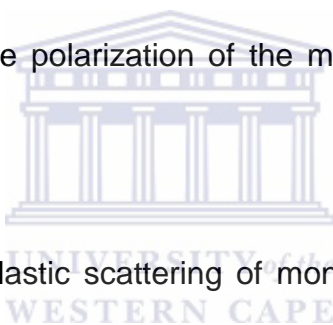
Scanning electron microscopy (SEM), coupled with energy dispersive x-ray spectroscopy (EDS) was used to study the morphology and elemental composition of the synthesized nanoparticles, as well as thin films. A Zeiss Auriga field-emission gun (FEG-) SEM operated at 5kV using an in-lens secondary electron detector was used for

high resolution imaging, whereas an Oxford Instruments X-Max solid-state silicon drift detector was used for the EDS analyses.

2.5. RAMAN SPECTROSCOPY

2.5.1. Introduction

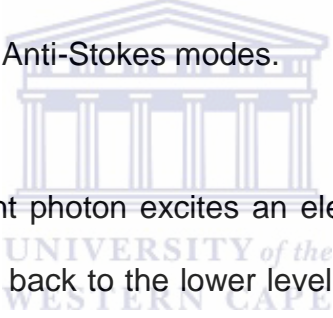
The Raman spectroscopy technique is used in this work to study the modes of vibration and rotation of physical systems. This technique is based on the principle of elastic and inelastic scattering of monochromatic electromagnetic radiation incident on the sample, which results in the polarization of the molecules in the physical system [2.16].



The technique is based on inelastic scattering of monochromatic light coming from a laser source. The inelastic scattering refers to the frequency of the photons in the monochromatic light that change upon interaction with the sample. The photons of the laser source are then absorbed and reemitted by the sample. The frequency of the reemitted photons shifts up or down in comparison with the original monochromatic frequency and this is called the Raman Effect. The down-shifted and up-shifted components are called Stokes and anti-Stokes lines, respectively. The shift gives information about the vibrational, rotational, and other low-frequency modes in a system [2.17].

2.5.2. Theory

The Raman Effect is based on the molecular deformation in the electric field E which is determined by the molecular polarizability α . The laser beam can be considered as an oscillating electromagnetic wave with electrical vector E . When the laser beam impinges on the sample, the electric dipole moment $P = \alpha E$ then induces molecule deformation. Because of this deformation the molecules start to vibrate with a characteristic frequency ν_m [2.16]. The monochromatic laser light with a frequency of ν_m excites molecules and transforms them into oscillating dipoles. Figure 2.11 shows the oscillating dipoles that are emitted by light at three different frequencies namely the Rayleigh scattering, Stokes and Anti-Stokes modes.



In each case, the incident photon excites an electron into a higher virtual state upon which the electron decays back to the lower level, emitting a scattered photon. In Rayleigh scattering the molecule with no Raman-active modes absorbs a photon with a frequency ν_m and the electron decays back to the same basic vibrational state from which it started. In the Raman scattering modes, namely Stokes and Anti-Stokes, the electrons excite to a different virtual level. The Stokes mode occurs when a photon with frequency ν_m is absorbed by a Raman active molecule which interacts in the basic vibrational state. This is excited to a Raman-active mode with frequency ν_n and results in the frequency of scattered light that is reduced to $\nu_m - \nu_n$. In the case of the Anti-Stokes mode, a photon with frequency ν_m is absorbed by a Raman-active molecule which interacts in the basic vibrational state and the excess energy of the excited Raman-active mode is then released. The electron decays to the basic vibrational state,

resulting in the frequency of scattered light of $\nu_0 + \nu_m$. Stokes lines are much more intense than anti-Stokes lines and are commonly used in spectroscopy because the electron in the most common temperature range is most likely to be in the lowest energy state, according to the Boltzmann distribution [2.17].

A Raman spectrum is a plot of intensity of Raman scattered radiation as a function of its frequency difference from the incident radiation (generally in units of wavenumber, cm^{-1}). This frequency difference is called the Raman shift. Because it is a difference value, the Raman shift is independent of the frequency of the incident radiation.

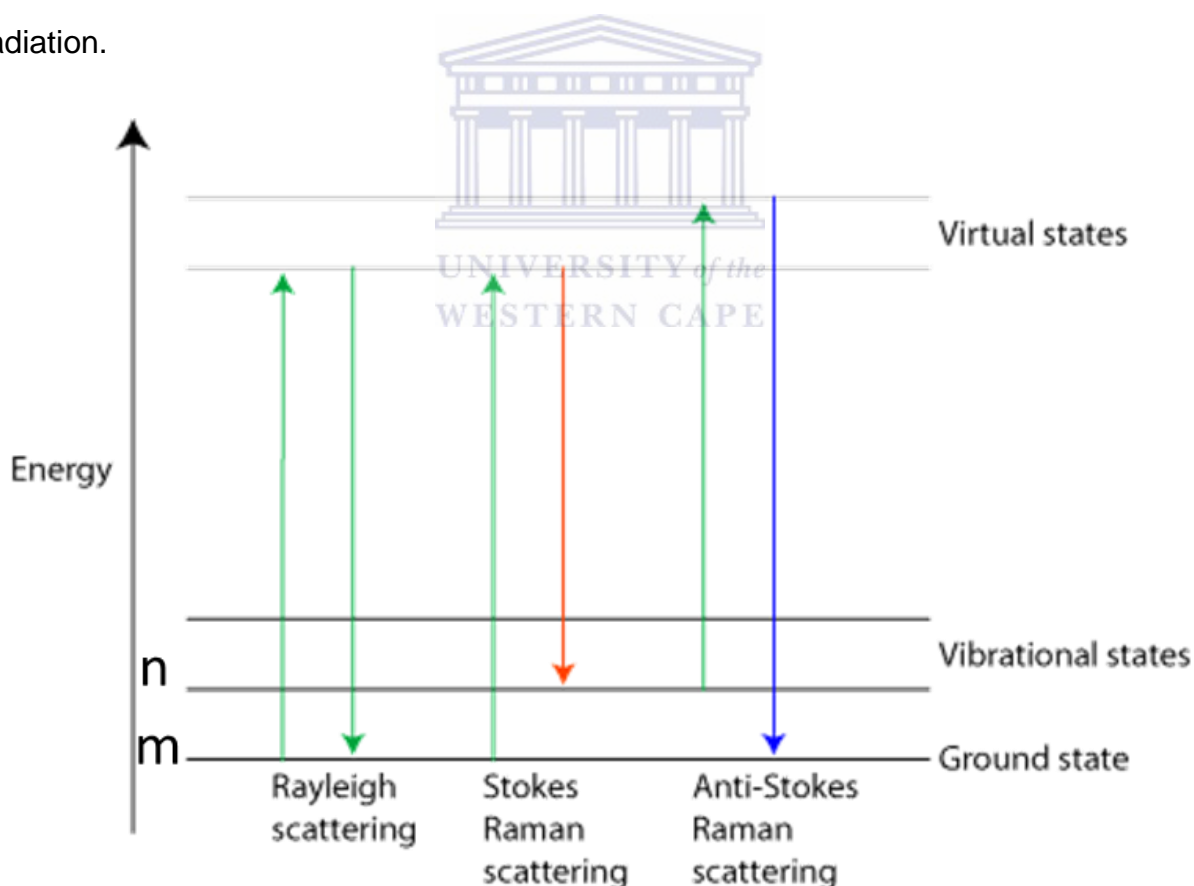


Figure 2.11: Diagram of the Rayleigh and Raman scattering processes [2.17].

2.5.3. Experimental set-up

Figure 2.11 shows a typical set-up for Raman spectroscopy. A monochromatic visible laser is used as an excitation source. The laser is passed through the Fabry-Perot etalon pinhole and is measured by the spectrometer. The laser gets directed through a series of mirrors till it reaches the beam splitter and the notch filter, where it gets reflected into the microscope onto the sample. The scattered radiation from the sample is reflected back into the optics onto the notch filter through the grater where it is captured by the charge-coupled detector (CCD) as shown in figure 2.12 [2.17]. A computer equipped with advanced software gives an output of the digitally acquired information in the form of a spectrum.

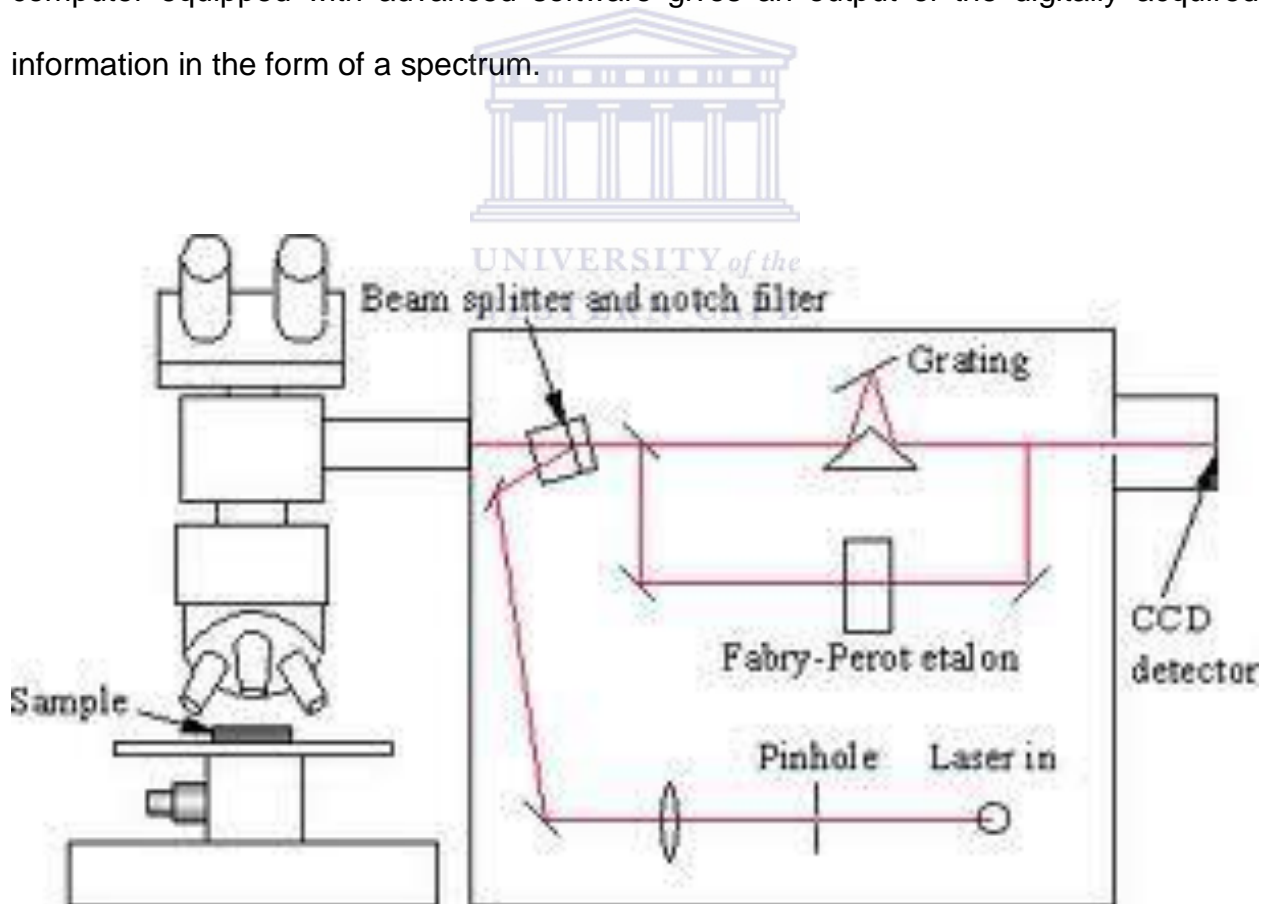


Figure 2.12: A schematic diagram of a Raman spectrometer [2.18].

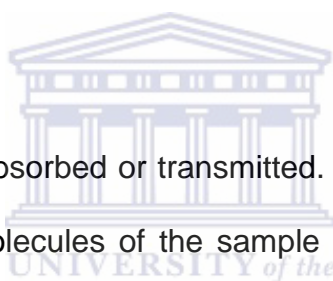
2.6. UV-VIS SPECTROSCOPY

2.6.1. Introduction

UV-Vis spectroscopy (UV-VIS) is a technique in which light is used in the visible, ultraviolet and the near infrared regions. In this region of the electromagnetic spectrum, molecules undergo electronic transitions. Emission spectroscopy deals with the transitions from the excited state to the ground state whereas absorption spectroscopy measures the transitions from the ground to the excitation state [2.19].

2.6.2. Theory

Light can be reflected, absorbed or transmitted. In a solution, when the beam of light is passed through, the molecules of the sample material can undergo electronic transitions from the ground state to the excited state. The transmittance is defined as the ratio of the intensity entering the sample (I_0) and the intensity passing through the sample (I_T) at a certain wavelength, as shown in figure 2.13.



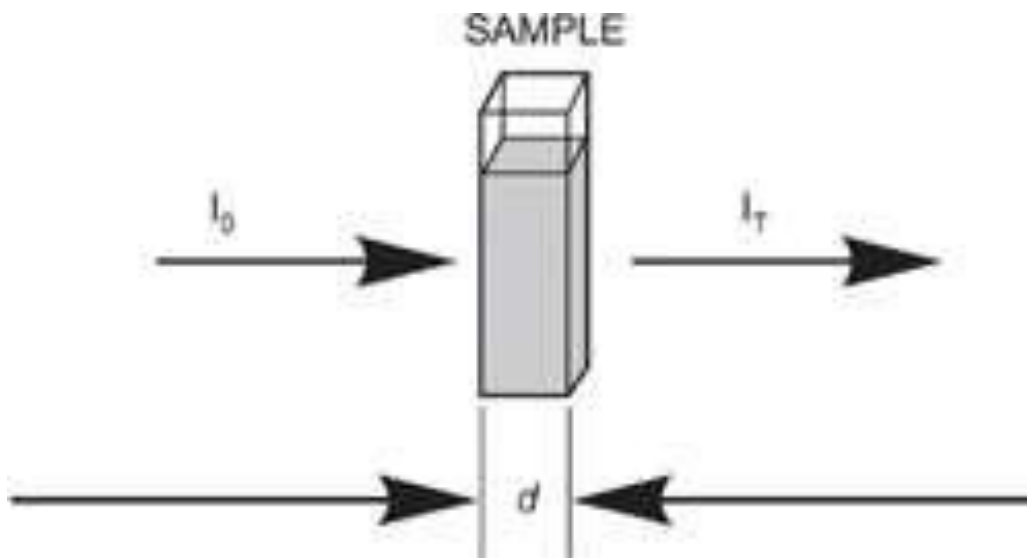


Figure 2.13: A Beer-Lambert example [2.19]

The percentage transmittance (%T) is expressed as follows:

$$\%T = \left(\frac{I_0}{I_T} \right) \times 100 . \quad (2.9)$$

Absorbance (A) of the sample is the negative logarithm of the transmittance and it is given by equation 2.10

$$A = -\log (T) . \quad (2.10)$$

The Beer-Lambert Law gives a linear relationship between the concentration (c) and the absorbance (A) for a solution provided the path length (d) is kept fixed. ϵ is a constant known as the molar absorptivity [2.19].

This equation is obtained as follows:

$$A = -\log(T) = \epsilon \cdot c \cdot d \quad (2.11)$$

Absorption of visible radiation corresponds to the excitation of outer electrons. There are different types of electronic transitions which can be considered, namely transitions involving pi (π), sigma (σ), and nonbonding (n) electrons, transitions involving charge transfer electrons, and transitions involving d and f electrons.

During energy absorption by molecules their electrons jump from their ground to the excited state. In a molecule, the atoms rotate and vibrate with respect to each other. These vibrations and rotations have discrete energy levels, which can be considered as being packed on top of each other as shown in figure 2.14.

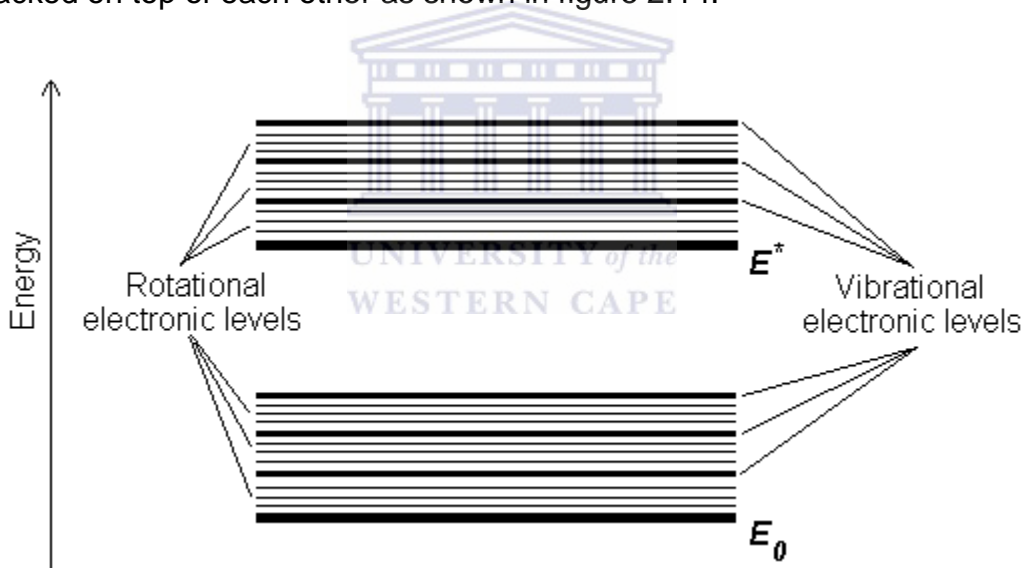


Figure 2.14: Rotational and vibrational electronic level of a molecule [2.19].

Absorption of UV-Vis radiation in organic molecules is not allowed for certain functional groups known as chromophores, which contain valence electrons of low excitation. The spectrum of the molecule containing these chromophores can be

complex because the superposition of rotational and vibrational transitions of the electronic transitions gives a combination of overlapping lines. This would appear as a continuous absorption band as seen in figure 2.15.

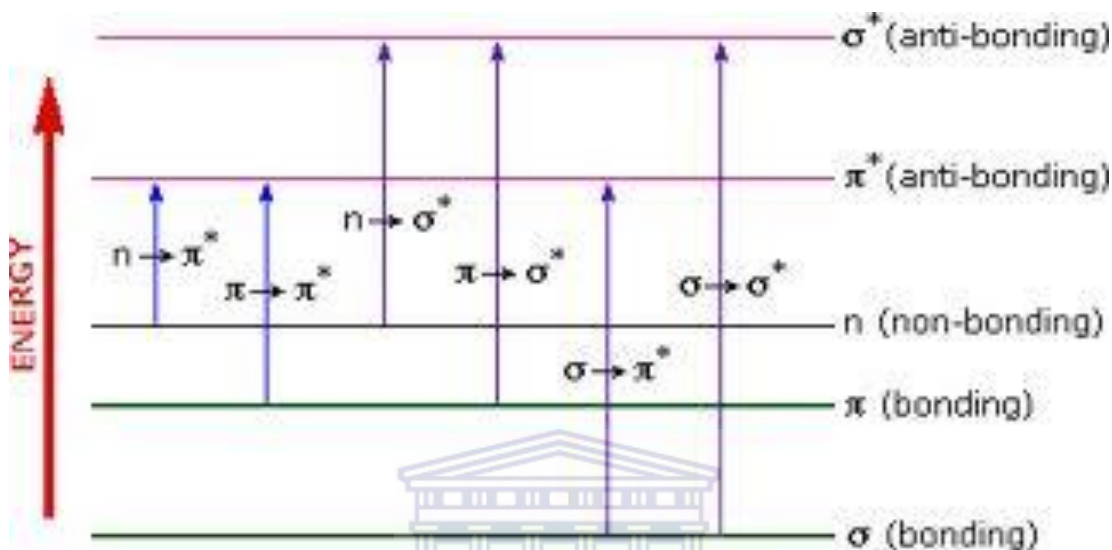


Figure 2.15: Possible electronic transition in a molecule [2.20].

UNIVERSITY of the
WESTERN CAPE

A brief discussion of the different transitions is given below [2.20].

(i) $\sigma \rightarrow \sigma^*$ Transitions

An electron in a bonding s orbital is excited to the anti-bonding orbital σ^* by absorption of radiation. These transitions require a large amount of energy and it corresponds to radiant frequencies in the ultraviolet region. The transitions for $\sigma \rightarrow \sigma^*$ are not seen in a typical UV-Vis spectrum.

(ii) $n \rightarrow \pi^*$ and $\pi \rightarrow \pi^*$ Transitions

Absorption spectroscopy of organic compounds is mostly based on the transition of π or n electrons to the π^* excited state because the absorption peaks fall in the

ultraviolet-visible region of the spectrum namely, 200 – 700 nm. These transitions need an unsaturated group in the molecule providing π electrons.

(iii) $n \rightarrow \sigma^*$ Transitions

Such transitions are produced in the saturated compounds containing atoms with unshared electron pairs. It needs less energy than that of the $\sigma \rightarrow \sigma^*$ transitions. This transition is found in the region between 150 and 250 nm [2.20].

Peaks from $n \rightarrow \pi^*$ transitions are shifted to shorter wavelength with an increase of solvent polarity which results in a blue shift. This arises from increasing solvation of the lone pair which lowers the energy of the n orbital. Sometimes the reverse is observed for $\pi \rightarrow \pi^*$ transition which results in a red-shift. This is due to the attractive polarization forces between the solvent and the absorber that leads to lower energy levels of both the excited and un-excited states. This effect is much greater for the excited state; the energy difference between the excited and un-excited states is shifted to give longer wavelengths [2.20].

2.6.3. Experimental set- up

A typical spectrophotometer is made up of a light source, a sample holder, a diffraction grating or monochromator to separate the different wavelengths of light, and a detector. The radiation source is often a Tungsten filament (300-2500 nm), a deuterium arc lamp that is continuous over the ultraviolet region (190-400 nm), or more recently light emitting diodes (LED) and Xenon arc lamps for the visible wavelengths. The detector is typically a photodiode or a charge-coupled (CCD) device. Photodiodes

are used with monochromators, which filter the light so that only light of a single wavelength reaches the detector. Diffraction gratings are used with the CCD, which collects light of different wavelengths on different pixels [2.20].

There are two types of UV-VIS instruments, namely the single and double beam spectrophotometer as depicted in figure 2.16 and figure 2.17, respectively. In a single beam instrument, all of the light passes through the sample and I_0 is measured by removing the sample. In the double beam instrument the light split in two beams before reaching the sample. The one beam is used as reference while the other beam goes through the sample. Both beams pass through both detectors simultaneously to be measured [2.20].

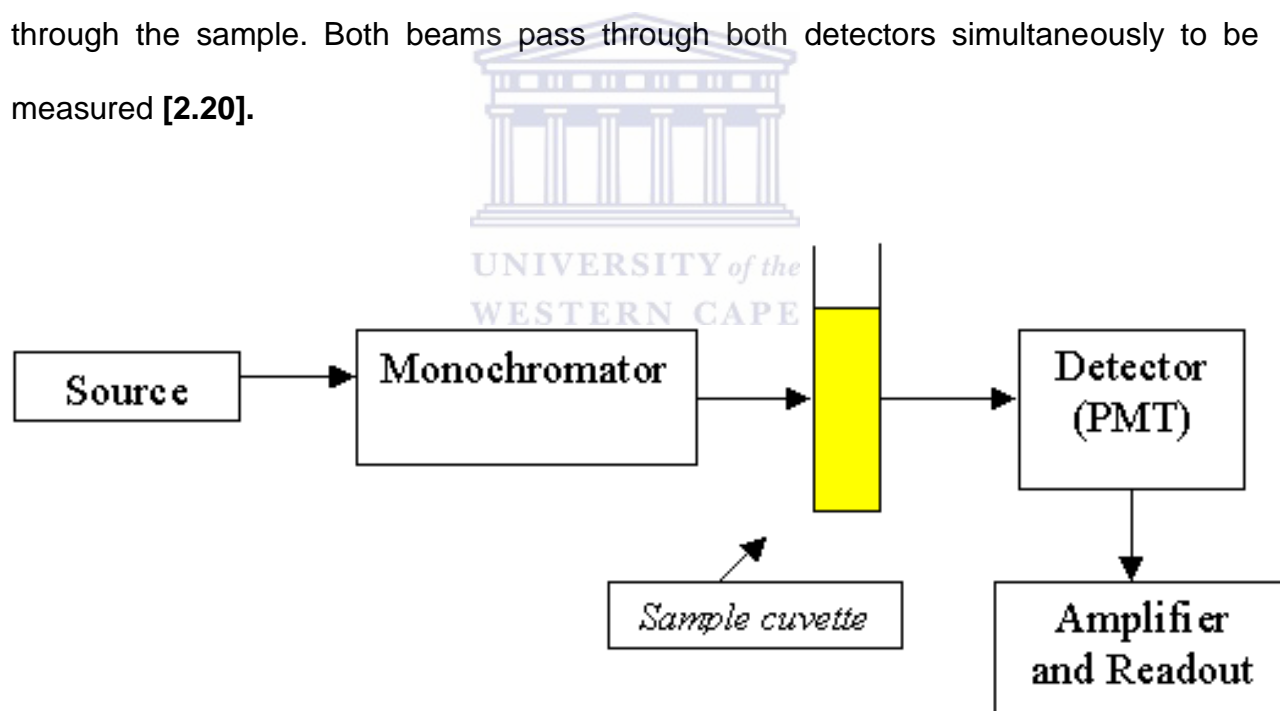


Figure 2.16: Schematic of a single- beam UV-Vis spectrophotometer [2.20].

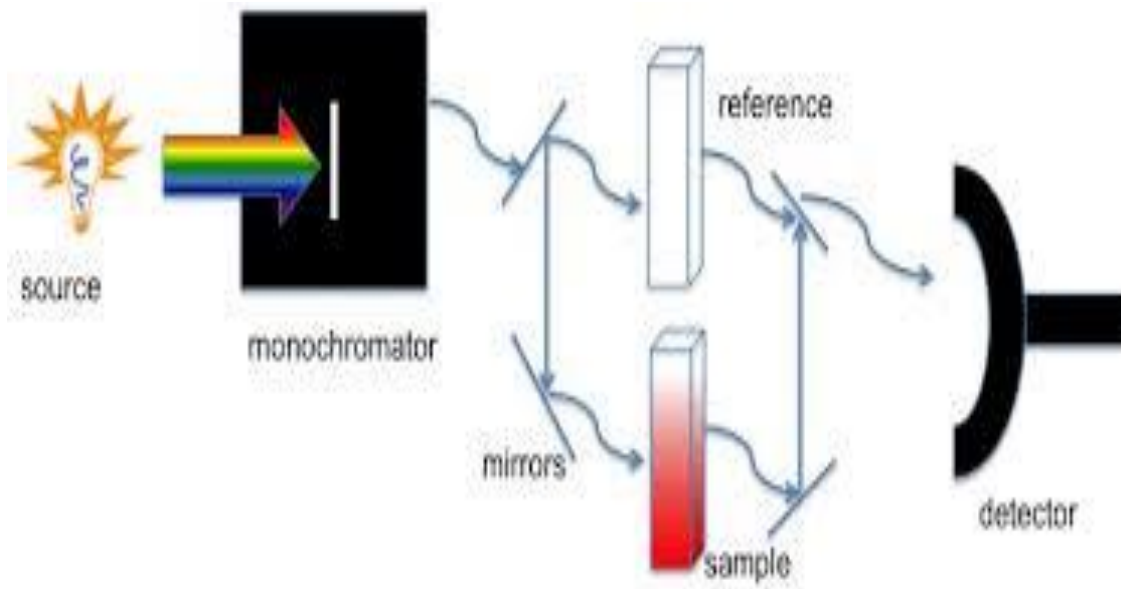


Figure 2.17: Schematic of a double- beam UV-Vis spectrophotometer [2.20].

The absorbance spectra of ZnO nanoparticles were recorded using a Cary 1E instrument for the nanoparticles in solvent. Also, the thin films absorbance was measured with, as well as the reflection and transmittance by M-probe & Cary1E instruments respectively. The Perkin Elmer Lambda 750 S UV-Vis spectrophotometer at CSIR, Pretoria was used to measure the absorbance of the hybrid thin films.

2.7. FOURIER TRANSFORM INFRARED SPECTROSCOPY

2.7.1. Introduction

Fourier Transform Infrared Spectroscopy (FTIR) is a non-destructive analytical technique that uses the photons in the infrared region of the electromagnetic spectrum. These photons have sufficient energy to induce amplified molecular vibrations in the infrared (IR) - active side of the sample's molecules. During this process there is a

change in the dipole moment of the infrared (IR) active molecule, which results in a signature spectrum of the molecule under investigation when measured [2.21].

2.7.2. Theory

When a beam of electromagnetic radiation is incident on a material, the beam can be absorbed, transmitted or reflected depending on its frequency, and the molecular structure of the material being irradiated. Beams of different frequency can have different effects on the molecules of the substance that is being irradiated. When a beam of electromagnetic radiation which has a frequency in the 1.2×10^{13} Hz to 1.2×10^{14} Hz (infrared frequency) band is passed through a sample, it effects a transition from one molecular vibrational energy to the next on the IR active molecule [2.22].

The photons of electromagnetic radiation possess energy, hence when a molecule absorbs electromagnetic radiation it gains energy to make a quantum transition from energy level E_1 to E_2 . The frequency of the absorbed radiation is associated with the transition energy by Planck's law which is

$$E_1 - E_2 = hv = \frac{hc}{\lambda} \quad (2.12)$$

If there exists an allowed transition that is related to the frequency of the incident radiation by Planck's constant, then the radiation will be absorbed; if the transition is forbidden (does not satisfy the Planck's equation) then the incident radiation will be transmitted.

When molecules vibrate, they do so with a frequency characteristic to the constituent elements. Only certain molecular vibrational motions are allowed as

permitted by quantum mechanics. For example, in the case of thin films of hydrogenated silicon (Si:H) irradiated by an IR radiation, different IR active hydrogen-silicon bonding configurations will absorb IR photon energy in different specific regions of the spectrum. The hydrogen atom that is bonded to silicon in the Si matrix produces a local vibrating dipole, this is because of the difference in the electronegativity between the hydrogen atom, which is negatively charged, and the silicon atom which is positively charged [2.22].

In this harmonic oscillator of Si-H, the dynamic dipole moment changes when an IR photon is absorbed by a Si-H oscillator. This results in a vibrational state with a larger vibrational dipole moment; this change in dynamic dipole moment and the concentration of the bonded hydrogen atoms will contribute to the spectral band and its intensity in the IR spectra [2.21]. A similar analogy can be made for IR-active bonds in other materials. Figure 2.18 shows the typical setup of the FTIR experiment.

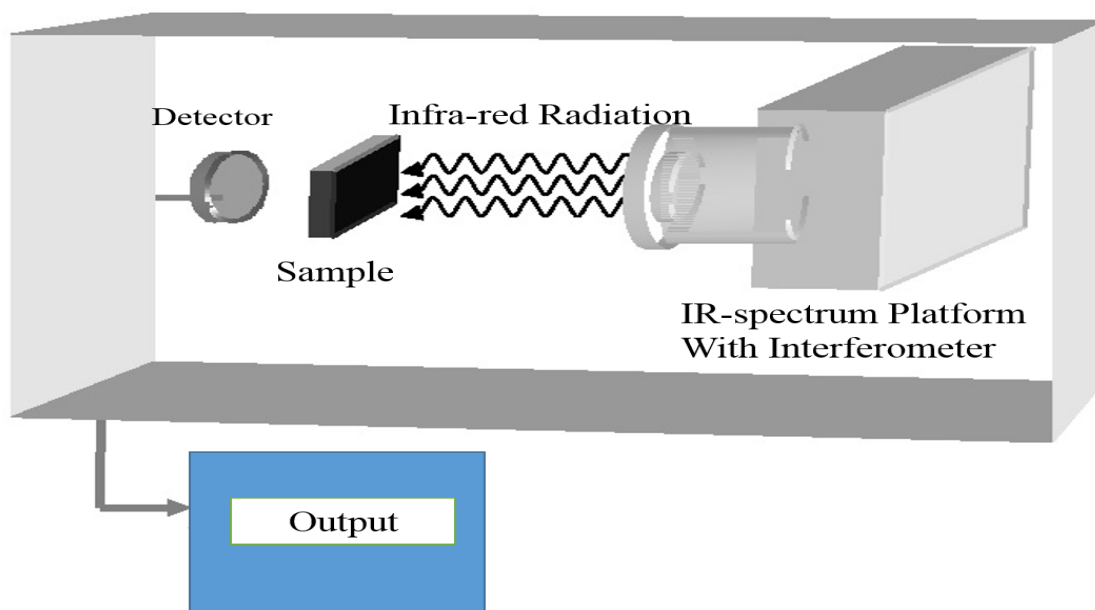


Figure 2.18: Schematic of FTIR experimental setup [2.21].

2.7.3. Experimental set- up

FTIR absorption spectra were collected in transmission geometry from 400 – 4000 cm^{-1} with a spectral resolution of 1 cm^{-1} , using a Perkin-Elmer Spectrum 100 FTIR spectrophotometer (UWC, Chemistry department). Unlike glasses, semiconductors like silicon have good infrared transparency and are not sensitive to humidity. Hence the substrate chosen for the characterization of thin films are mono-crystalline silicon (c-Si) wafers of orientation $\langle 100 \rangle$. Infrared transmission $T(\omega)$ as a function of vibrational frequency ω was measured by first collecting a background spectrum of the c-Si substrate which is used to correct the background signal.

2.8. X-RAY PHOTOELECTRON SPECTROSCOPY

2.8.1. Introduction

XPS, also known as ESCA (Electron Spectroscopy for Chemical Analysis), is the most widely used surface analysis technique because of its relative simplicity, in both use and data interpretation [2.23]. The sample is irradiated with mono-energetic x-rays causing photoelectrons to be emitted from the sample surface. An electron energy analyzer determines the binding energy of the photoelectrons. From the binding energy and photoelectron peak intensity, the elemental identity, chemical state, and quantity of an element are determined. The information XPS provides about surface layers or thin film structures is of value in many industrial applications including: polymer surface modification, catalysis, corrosion, adhesion, semiconductor and dielectric materials, electronics packaging and thin film coatings used in a number of industries [2.24].



2.8.2. Theory

XPS uses an electromagnetic wave that interacts with a material or atoms while simultaneously measuring its kinetic energy (E_K) [2.25]. It measures electrons that escape the surface of a material from 1 to 10 nm. An electron of a given electronic level is described by its binding energy, E_B , which is obtained using the energy conservation law [2.25]:

$$E_B = h\nu - E_K - \phi , \quad (2.13)$$

where E_B is the binding energy, $h\nu$ is the energy of the excitation x-rays, E_K is the kinetic energy of the emitted photoelectrons and ϕ is the energy given off by photoelectron emission process. The binding energy E_B is described by the difference between the total energy at the initial state and the energy of the photoelectron emission process. The resulting spectra reflect the electronic structure of a material, giving information on the electron configuration and energy levels within the atoms.

2.8.3. Experimental set- up

XPS is operated in ultra-high vacuum (UHV) conditions [2.25]. Its basic requirements for a photoemission experiment (XPS or UPS) are:

- ❖ A source of fixed-energy radiation - an x-ray source for XPS or a He discharge lamp for UPS.

- ❖ An electron energy analyzer – which can disperse the emitted electrons according to their kinetic energy and measure the flux of emitted electrons of a particular energy.
- ❖ A high vacuum environment – to enable the emitted photoelectrons to be analyzed without interference from gas phase collisions.

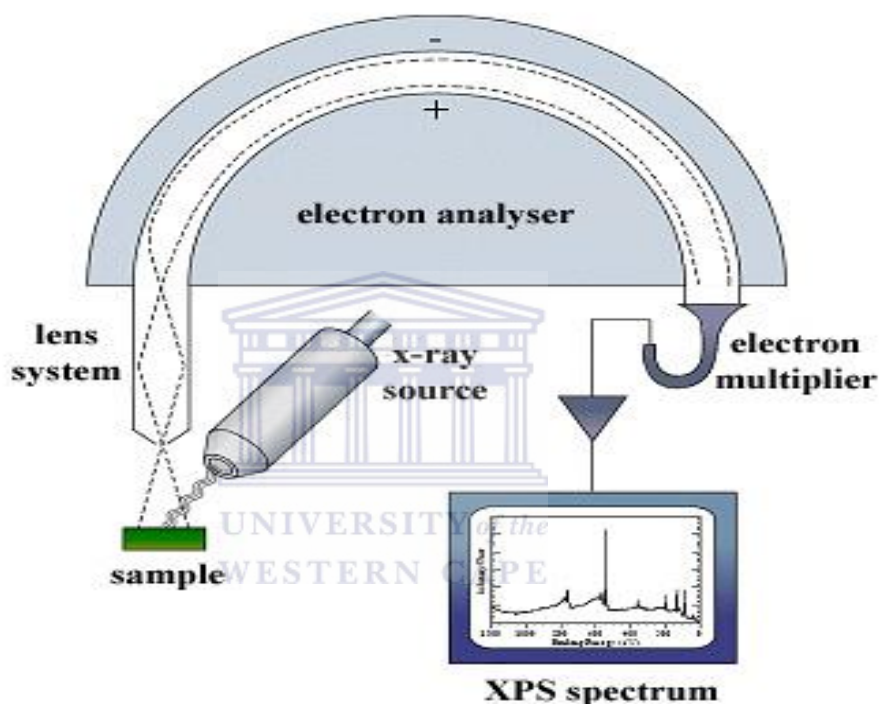


Figure 2.19: Schematic diagram depicting X-ray photoelectron spectroscopy [2.23].

X-ray photo-electron spectroscopy (XPS) measurements were performed at the University of the Free State using a PHI 5000 Versaprobe-Scanning ESCA Microprobe, utilising monochromatic Al K α radiation ($h\nu = 1486.6$ eV) as excitation source. The pressure during data acquisition was typically below 1×10^{-8} Torr.

2.9. PHOTOLUMINESCENCE SPECTROSCOPY

2.9.1. Introduction

Photoluminescence (PL) is the spontaneous emission of light from a material under optical excitation [2.24]. The excitation energy and intensity can be chosen to probe different excitation types and also different parts of the sample. PL analysis is nondestructive. The technique requires very little sample preparation or environmental control. When light of sufficient energy is illuminating a material, photons are absorbed and (electronic) excitations are created. These excited electrons relax and a photon is emitted. The PL can be collected in the form of an energy spectrum and analyzed to provide information about the photo-excited states. The PL spectrum reveals transition energies and the PL intensity gives a measure of the relative rates of radiative recombination. Variation of the PL intensity upon change of external parameters, e.g. temperature, excitation energy, power of excitation, can be used to further characterize electronic states and bands. PL investigations can be used to characterize a variety of materials parameters, which will be introduced respectively as follows [2.26]:

(i) Band gap determination

The most common radiative transition in semiconductors is between states in the conduction and valence bands of a semiconductor. Band-gap determination is particularly useful when working with new compound semiconductors.

(ii) Impurity levels and defect detection

Radiative transitions in semiconductors also involve localized defect levels. The PL energy associated with these levels can be used to identify specific defects, and the PL intensity can be used to determine their concentration.

(iii) Recombination mechanisms

As discussed above, the return to equilibrium, also known as "recombination" can involve both radiative and non-radiative processes. The PL intensity and its dependence on the level of photo-excitation and temperature are directly related to the dominant recombination process. Analysis of the PL spectrum helps to understand the underlying physics of the recombination mechanism.

(iv) Material quality

In general, non-radiative processes are associated with localized defect levels, whose presence is detrimental to material quality and subsequent device performance. Thus, material quality can be measured by quantifying the amount of radiative recombination.

2.9.2. Experimental set- up

A typical PL set-up consists of an optical source and a power meter or a spectrophotometer. As shown in figure 2.20, a laser (which is the excitation source), provides a stable and well defined source of monochromatic light that is directed onto a sample. When the light moves through the sample, photons are absorbed and excitation

and emission occur. This is then passed through the lens through the spectrometer and finally onto the photo detector [2.27].

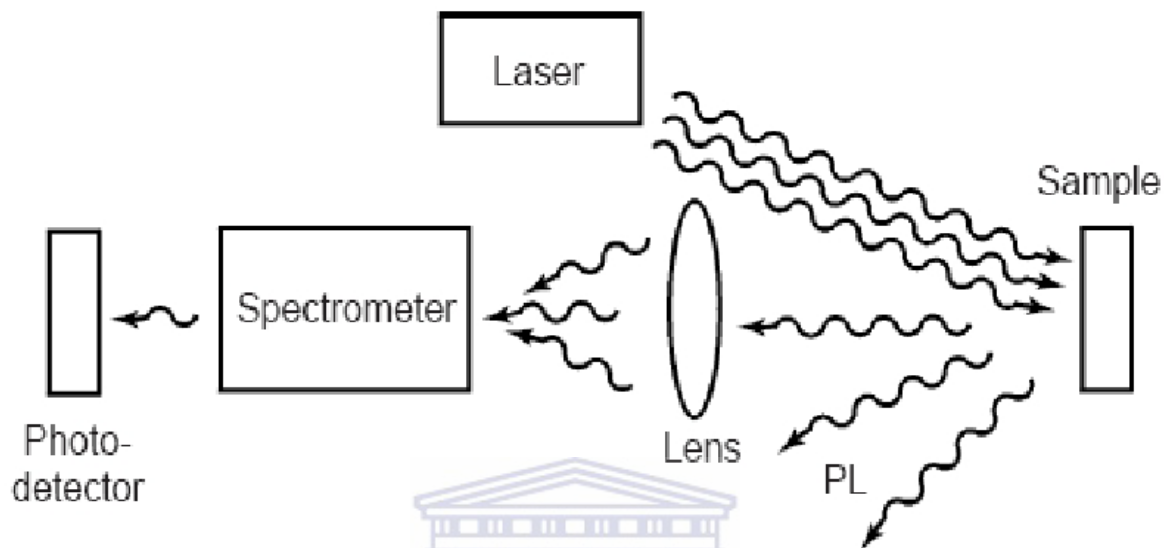


Figure 2.20: A typical experimental set-up for PL [2.27].



PL was investigated using a Perkin-Elmer LS2 Fluorescence Spectrometer in the range from 340 – 800 nm with an excitation source of 320 nm at the CSIR, Pretoria, South Africa.

2.10. ATOMIC FORCE MICROSCOPY

2.10.1. Introduction

Atomic Force Microscopy (AFM) is a high resolution type of scanning probe microscopy which exhibits a resolution on the order of fractions of a nanometer. It

demonstrates a much better resolution which is 1000 times better than the optical diffraction limit [2.28]. According to *Dillon et al* [2.29], AFM modes provide opportunities for measurements of surface properties and tip-sample interactions. Surface charge density, potential, conductivity, and capacitance are some important electrical surface properties measured by AFM modes. Additional modes are also possible for the analysis of magnetic and thermal properties of the sample although specific probes may be required. Measurements of surface properties and tip-sample interactions are extremely important for the investigation of, for instance, surface electronic states, corrosion processes and surface chemistry in general. AFM modes can also be used as a tool for lithographic applications.



2.10.2. Theory

The main advantages of AFM compared to the other microscopic techniques are the larger resolution (going down to the atomic resolution), almost no sample preparation, large range of materials that can be measured and the non-destructive nature of the method [2.28-2.29]. Some others methods have also been developed, such as magnetic force microscopy (MFM), electric force microscopy (EFM), scanning thermal microscopy (STM), and near-field scanning optical microscopy (NSOM). However, all these methods are basically only extensions of the basic AFM scheme [2.29]. Information about the surface of a sample can be gained by employing atomic force microscopy (AFM). The information about the surface roughness can be used to extrapolate information on the growth mode of a given sample. A typical setup for an AFM is shown in figure 2.21.

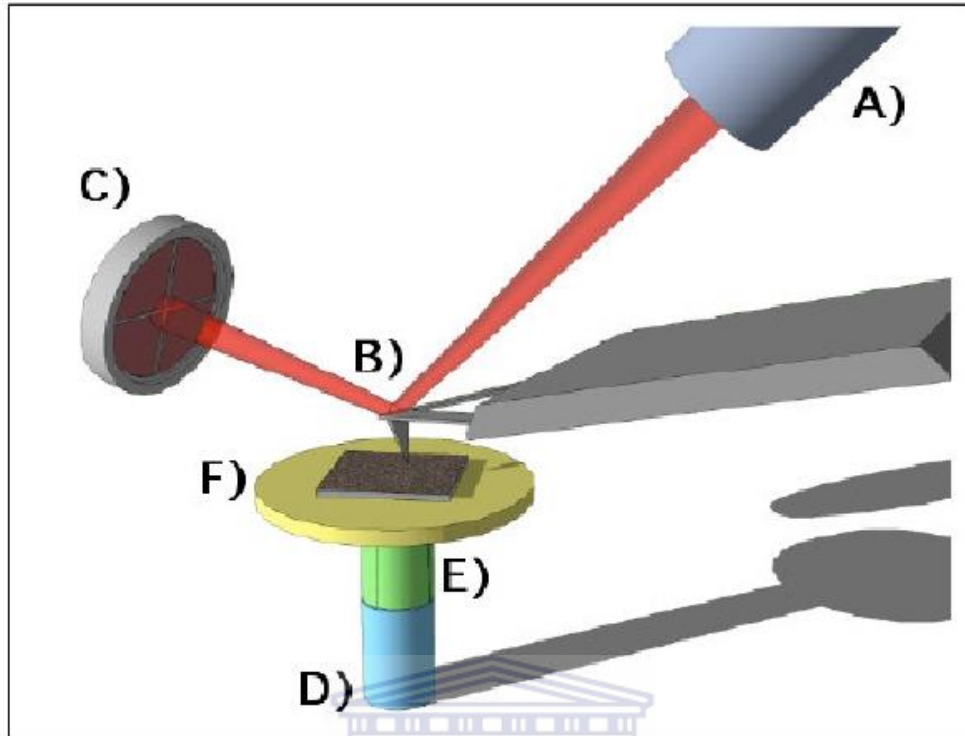


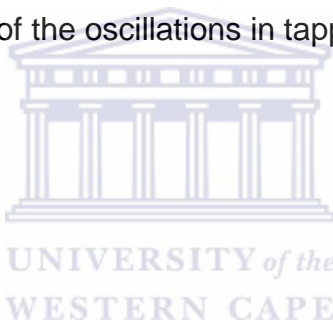
Figure 2.21: A cartoon illustrating the AFM working principle [2.28].

UNIVERSITY of the
WESTERN CAPE

In the figure (A) is the laser focusing a laser beam at the top end of a cantilever (B), from where it is reflected at the center of a 4 quadrants photodiode (C). Any cantilever deformation (bending or torsion) will be easily detected as spot movements on the photodiode. At the end of the cantilever a very sharp tip is in close proximity with the sample surface (F). The sample surface is moved below the tip using an x- and y-piezoscanner (E). During the rastering process the tip bends (or changes its resonant frequency) as a function of surface morphology. A z-piezoscanner (D) approaches or moves away from the surface (F) from the tip in order to maintain constant bending or resonant frequency. Voltages needed to perform these corrections are used to reconstruct surface topography during imaging.

The sample surface (F) is placed under the (ideally) atomically sharp tip of a cantilever (B). The tip is brought into close proximity of the sample surface. The forces between the tip and the sample lead to a deflection of the cantilever according to Hooke's law, where the spring constant of the cantilever is known. Typically, the deflection is measured using a laser spot (A) reflected from the top of the cantilever into an array of photodiodes (D). If the tip were kept at constant height, there would be a risk that the tip would collide with the surface, causing damage. Therefore, in most cases a feedback mechanism is employed to adjust the tip-to-sample distance. This way it is possible to keep the force between the tip and the sample constant. Generally, the sample is mounted on a piezoelectric tube. With this tube the sample can be moved in the z direction, thus maintaining a constant force. The image recorded in this way resembles the surface topography of the sample. Many different modes of operation have been developed over the years for the AFM. The most commonly used ones are contact mode, non-contact mode, and dynamic contact mode. In contact mode operation, the force between tip and the surface is kept constant during scanning by maintaining a constant deflection. For the non-contact mode it is possible to have the cantilever oscillating at or close to its resonance frequency by means of an external force. The tip-sample interaction force modifies the oscillation. Information on the sample characteristic can be gained through monitoring the changes in the oscillation with respect to the external reference. The problem with this mode is that most samples develop a liquid meniscus layer. Keeping the tip close to the surface while at the same time preventing it from getting stuck in the meniscus layer is a big problem in ambient conditions. To circumvent this problem, the dynamic contact mode was developed by

Zhong et al. [2.30]. In this mode, the cantilever is oscillated with so much force, that even though it gets into direct contact with the surface on each oscillation, it gets detached from it again. The non-contact and dynamic contact mode operation can be used for example, either under frequency modulation or the more common amplitude modulation. When measuring with frequency modulation, information about a sample's characteristics is provided by monitoring changes in the oscillation frequency. Amplitude modulation, which is better known as intermittent contact or tapping mode, provides information on the sample surface topography by monitoring changes in the oscillation amplitude. It is also possible to discern between different kinds of materials on the surface by analyzing the phase of the oscillations in tapping mode.



2.10.3. Experimental set-up

Atomic Force Microscopy (AFM) images of the top surface of thin films of ZnO, P3HT, PCBM, P3HT:PCBM blends and ZnO:P3HT:PCBM hybrids spin coated on Si (110) substrates in a tapping mode were analysed using a Veeco AFM system (Digital Instruments) at ambient conditions (CSIR, Pretoria).

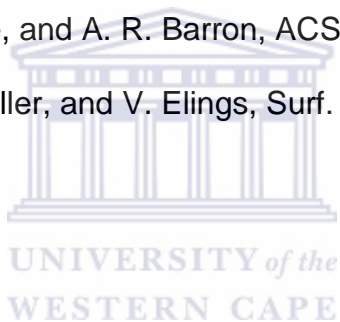
2.12. REFERENCES

- [2.1] A. R. West, *Solid State Chemistry and its Applications*, Wiley, New York (1984).
- [2.2] B. D. Cullity, in “*Elements of X-ray diffraction*”, Addison-Wesley Publishing Company, Reading, Massachusetts (1978)

- [2.3] O. G. Palanna, Engineering Chemistry, Tata McGraw Hill Education Pvt. Ltd., New Delhi, (2009)
- [2.4] International Tables for X-ray Crystallography. Vol. IV; Kynoch Press: Birmingham, UK (1974).
- [2.5] P. J. Goodhew, J. Humphrey, R. Beanland, Electron Microscopy and Analysis – Third Edition, Taylor and Francis, London, (2001)
- [2.6] D. Chescoe, P. J. Goodhew, The Operation of the Transmission Electron Microscopy, Royal Microscopical Society and Oxford University Press, New York, 1984
- [2.7] H.H. Willards, L.L. merritt Jr. J.A. Dean and F.A. Settle Jr. Instrumental Methods of Analysis 7th Edition, Wadsworth Publication. Co. (1988)
- [2.8] D. Shindo and K. Hiraga, High-Resolution Electron Microscopy for Material Science, Springer, New York (1998).
- [2.9] J. Goldstein, Scanning Electron Microscopy and X-ray Microanalysis, Third Edition, Springer 2003
- [2.10] A. Hibbs, Confocal Microscopy for Biologists, Twayne Publishers, Boston (2004).
- [2.11] J. Pawley, Handbook of Biological Confocal Microscopy, Twayne Publishers, Boston (2006).
- [2.12] D. Semwogerere and E. R. Weeks, Encyclopedia of Biomaterials and Biomedical Engineering Confocal Microscopy, Taylor Francis (2005).
- [2.13] C. Sheppard, Confocal Laser Scanning Microscopy, Twayne Publishers, Boston (1997).

- [2.14] Russ, J. C. Fundamentals of Energy Dispersive X-ray Analysis, Butterworths. London (1984).
- [2.15] Goldstein, J. I., et al. Scanning Electron Microscopy and X-ray Microanalysis, 3rd ed, Plenum Press, New York (2003).
- [2.16] W. Demtröder, Laser Spectroscopy Basic Concepts and Instrumentation, Springer, New York (2003).
- [2.17] E. Smith, G. Dent, Modern Raman Spectroscopy - A Practical Approach, John Wiley & Sons Ltd., England, (2005)
- [2.18] D. W. Mayo, F. A. Miller, and R. W. Hannah, Course Notes on the Interpretation of Infrared and Raman Spectra, Wiley-VCH, Hoboken, NJ (2003).
- [2.19] O. G. Palanna, Engineering Chemistry, Tata McGraw Hill Education Pvt. Ltd., New Delhi, (2009)
- [2.20] D. A. Skoog, F. J. Holler, and S. R. Crouch, Principles of Instrumental Analysis, 6th edition, Brooks Cole (2006).
- [2.21] Lau, W.S. Infrared characterization for microelectronics. World Scientific. ISBN 9810223528 (1999).
- [2.22] Properties of Amorphous Silicon and its Alloys. Edited by Tim Searle. An INSPEC Publication, Emis Data Review series. ISBN 0852969228
- [2.23] J. Bockris, Modern Electrochemistry 2A, 2nd ed., Springer (2001).
- [2.24] N. S. Sariciftci, Primary Photoexcitations In Conjugated Polymers Molecular Exciton Versus Semiconductor Band Model, World Scientific Publishing Company, Singapore (1997).

- [2.25]. N. Ikeo, Y. Iijima, N. Niimura, M. Sigematsu, T. Tazawa, S. Matsumoto, K. Kojima, Y. Nagasawa, Handbook of X-ray Photoelectron Spectroscopy, JEOL, (1991)
- [2.26] D. C. Harris, Quantitative Chemical Analysis, 7th Ed, W. H. Freeman and Company, New York (2006).
- [2.27] T. H. Gfroerer, Photoluminescence in Analysis of Surfaces and Interfaces, John Wiley & Sons Ltd, Chichester, 2000.
- [2.28] S. H. Cohen and M. L. Lightbody. Atomic Force Microscopy/Scanning Tunneling Microscopy 2. Plenum, New York (1997).
- [2.29] E. P. Dillon, C. A. Crouse, and A. R. Barron, ACS Nano, , 2, 156 (2008).
- [2.30] Q. Zhong, D. Innis, K. Kjoller, and V. Elings, Surf. Sci. Lett. 290, L688. (1993).



CHAPTER 3

STRUCTURAL AND OPTICAL PROPERTIES OF ZnO GROWN BY HYDROTHERMAL METHOD

3.1. INTRODUCTION

Zinc oxide (ZnO) is a wide band gap group II-VI semiconductor with unique physical and chemical properties, such as high chemical stability, high electrochemical coupling coefficient, broad range of radiation absorption and high photostability [3.1]. A broad energy band gap (3.37 eV), high binding energy (60 meV), which can ensure an efficient exciton emission at room temperature under low excitation energy, and high thermal and mechanical stability at room temperature [3.2] make it attractive for potential use in electronics, optoelectronics, laser and solar cells technology. ZnO nanostructures are generally grown by both physical and chemical methods like pulsed laser deposition, sputtering, and the hydrothermal method.

Among the various techniques, the hydrothermal method is a simple and inexpensive route to grow ZnO nanostructures. The hydrothermal method offers the advantage that it can form various types of morphologies by regulating the growth environment conditions [3.3-3.5], or adopting additive and changing pH in the nanostructures growth process [3.6-3.8]. However, ZnO nanostructures are rarely combined with low band gap polymer solar cells into devices with an explicit result; hence in this work highly crystalline ZnO nano-structures, composed of well-defined

pyramidal shapes were successfully synthesized using a simple hydrothermal method for applications in organic-polymer based solar cells.

3.2. EXPERIMENTAL DETAILS

3.2.1. Synthesis of ZnO nanoparticles

To synthesize ZnO-nanostructures, about 3.0 g of zinc nitrate hexahydrate ($\text{Zn}(\text{NO}_3)_2 \cdot 6\text{H}_2\text{O}$, Sigma-Aldrich, South Africa) was added to 80 ml of ethylene glycol (Aldrich) in a 250 ml round-bottom flask. In addition, 0.8 g of polyvinylpyrrolodine (Sigma-Aldrich, South Africa) as a structure directing template agent was also added, and the reaction mixture pH was adjusted to 10 using ammonium hydroxide (NH_4OH) (Sigma-Aldrich, South Africa). The reaction mixture was stirred continuously under reflux for 24 hours; the obtained precipitate was collected by filtration, washed thoroughly, and then dried at 120 °C for 12 hours.

3.2.2. Characterization

Thermo-gravimetric analyses (TGA) were carried out on a 3.5 mg sample of ZnO nanostructures using a TA Q500 thermo-gravimetric analyser. Measurements were performed in an oxygen atmosphere at a heating rate of 10 °C/min from room temperature to 950 °C (CSIR, National Centre for nanostructured Materials (NCNSMs), Pretoria).

X-ray diffraction (XRD) patterns were collected in reflection geometry at 2θ -values ranging from $10 - 90^\circ$, with a step size of 0.02° , using a PANalytical® X-ray powder diffractometer operating at 45 kV and 40 mA. Monochromatic Copper (Cu) $K\alpha_1$ radiation with a wavelength of 0.154 nm was used as the X-ray source (CSIR-NCNSMs, Pretoria).

An FEI Tecnai F20 field emission high-resolution transmission electron microscope (HR-TEM), operated at 120 kV was employed to examine the internal structure and crystallinity of the different samples. Specimens for HR-TEM analysis were prepared by transferring a small drop of each solution of ZnO on a holey-carbon copper grid and dried at ambient conditions (University of the Western Cape).

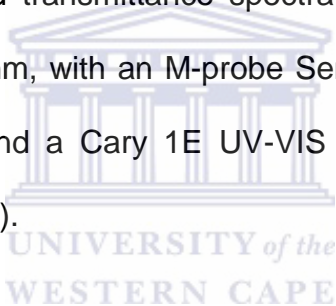
A Horiba Jobin Yvon HR800 Raman spectrometer was used to collect Raman spectra in backscattering geometry at room temperature in the region $100 - 3000\text{ cm}^{-1}$, with energy resolution of 0.4 cm^{-1} , using a 514.5 nm Ar^+ -ion laser (CSIR-NCNSMs, Pretoria).

A Zeiss Auriga field-emission gun (FEG-) SEM operated at 5kV using an in-lens secondary electron detector was used for high resolution imaging, whereas an Oxford Instruments X-Max solid-state silicon drift detector was used for the energy dispersive x-ray (EDS) analyses (University of the Western Cape).

Photoluminescence (PL) was investigated using a Jobin-Yvon NanoLog spectrometer in the range from 330 - 800 nm with an excitation source of 325 nm at the CSIR-NCNSMs, Pretoria.

Topography analyses were carried out using a Veeco AFM system (Digital Instruments) atomic Force Microscopy (AFM) in a tapping mode at ambient conditions (CSIR, Pretoria).

The absorbance spectrum of ZnO nanoparticles in ethanol solution was recorded using a Cary 1E UV-VIS spectrophotometer (University of the Western Cape), whereas the absorbance spectrum of spin-coated ZnO on Corning 7059 glass was recorded with a Perkin-Elmer LAMDA 750S UV-VIS spectrophotometer (CSIR-NCNSMs, Pretoria) in the range from 200 – 800 nm with a spectral line width of 1 nm. Additional optical reflectance (on c-Si wafer) and transmittance spectra (on Corning 7059 glass) were measured between 315 - 900 nm, with an M-probe Semiconsoft instrument and with a spectral resolution of 1 nm, and a Cary 1E UV-VIS spectrophotometer respectively (University of the Western Cape).



3.3. RESULTS AND DISCUSSION

3.3.1. Thermal analysis

The thermal stability of ZnO nanostructures was investigated using thermogravimetric analysis (TGA) in air as shown in Figure 3.1. A weight loss of about 1.5% is observed when the sample is heated below 100 °C. Above 100 °C, about 8% of weight loss is observed. This initial weight loss between 50 and 200 °C is ascribed to the removal of physically and chemically adsorbed water molecules. At higher temperature, between 200 and 350 °C, an increase in weight loss is noticeable, which can be due to

the decomposition of hydroxide groups [3.9]. A weight change above 700 °C might be due to the change of the crystal structure, i.e., the crystallization of ZnO. A larger exothermic peak around 490 °C, due to the crystallization of ZnO was reported by Chen et al. [3.10].

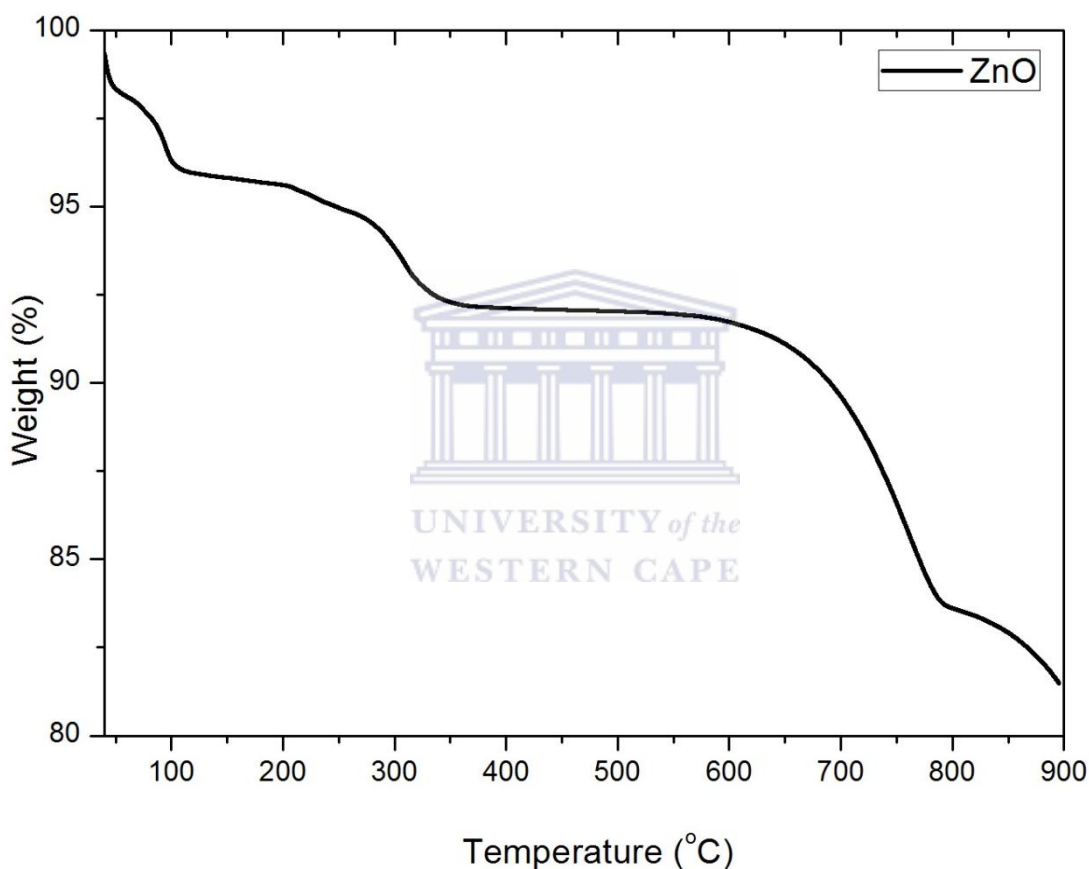


Figure 3.1: TGA analyses of ZnO nanostructures.

3.3.2. Structural Properties

Figure 3.2 represents the X-ray diffraction pattern of ZnO powder. It is observed that all the peaks correspond to the wurtzite structure of ZnO [3.11]. No other diffraction

peaks from impurities and residues are detected, indicating that the as-synthesised sample is pure ZnO without an impurity phase. Peak broadening can be used to explain the particle sizes as reported in [3.12], a definite line broadening of the XRD peaks indicates that the prepared material consist of particles in the nanoscale range [3.12, 3.13]. From the XRD patterns analysis, it is possible to determine peak intensity, position and width, full-width at half-maximum (FWHM) data in order to quantify the charge transfer mechanism.

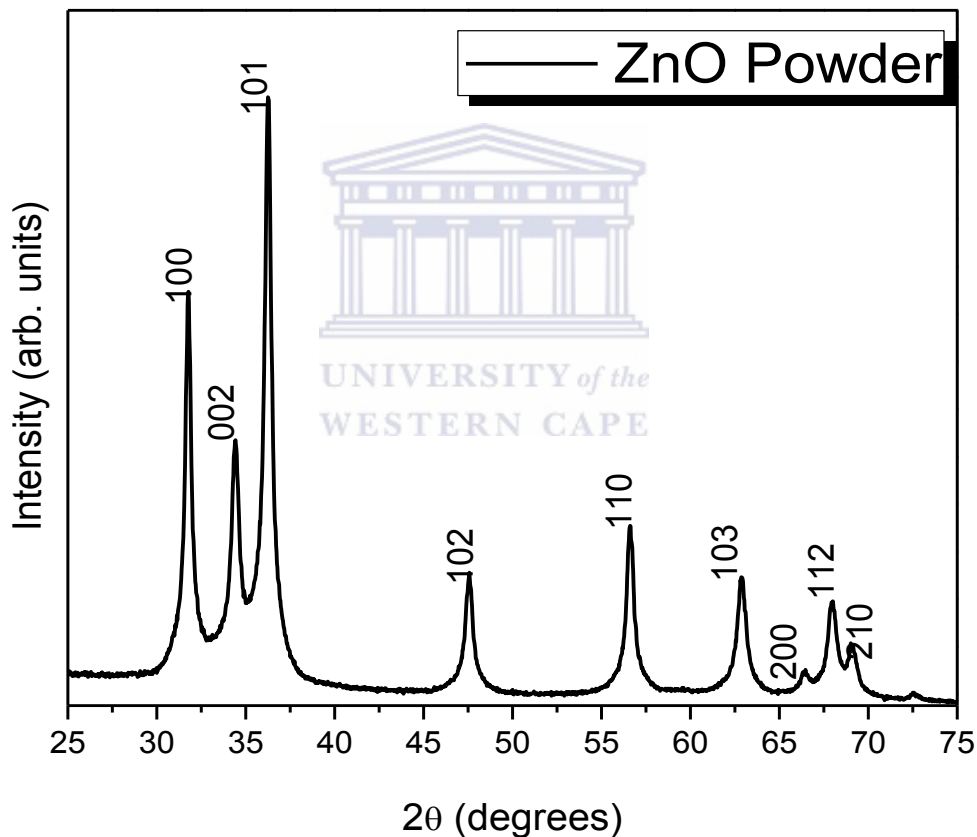


Figure 3.2: XRD patterns of ZnO powder.

The (101) diffraction peak appears to be dominant (Figure 3.2), implying that the majority of crystallites have a preferred growth along the (101) plane. Therefore, the

evolution of the (101) diffraction peak was used to obtain quantitative data analysis, which is summarized in Table 3.1. The interplanar spacing d and particle size D was calculated using Bragg's Law and the Debye-Scherrer formula (3.2), respectively, by:

$$n\lambda = 2d \sin\theta \quad (3.1)$$

and

$$D = \frac{0.9\lambda}{\beta \cos \theta} \quad (3.2)$$

where λ , n , θ and β is the wavelength of the incident beam (1.54060 Å for the $\text{CuK}\alpha$), the interference order, the Bragg diffraction angle and the full-width-at-half-maximum (FWHM) of the diffraction peak, respectively. From the interplanar spacing and the set of lattice parameters (hkl), the lattice constants for a hexagonal wurtzite structure a and c was calculated from [3.2]:

$$d_{hkl} = \frac{a}{h^2+k^2+l^2} \quad (3.3)$$

and

$$\frac{1}{d^2} = \frac{4}{3} \left(\frac{h^2+hk+k^2}{a^2} \right) + \frac{l^2}{c^2} \quad (3.4)$$

The values of the experimental parameters of a and c will be compared to the standard parameters of ZnO, as shown in table 3.1, while table 3.2 draws comparison between d-spacing.

The diffraction peaks located at 31.84°, 34.52°, 36.33°, 47.63°, 56.71°, 62.96°, 68.13°, and 69.18° have been indexed as hexagonal wurtzite phase of ZnO with lattice constants $a = b = 0.324$ nm and $c = 0.521$ nm (JPCDS card number: 36-1451). The XRD pattern further confirms that the synthesized ZnO powder was free of impurities as it does not contain any characteristic XRD peaks other than ZnO. The average particle size (D) of the sample was found to be 20.5 nm, which is derived from the FWHM of the more intense peak corresponding to the (101) plane located at 36.25° using Scherrer's formula. The volume of the unit cell for the hexagonal system has been calculated from the following relation [3.2]:

$$V = 0.866 * a^2 * c \quad (3.5)$$

Table 3.1: Summary of the lattice constants of the synthesized ZnO powder.

Material	Calculated			JCPDS: 36-1451	
	a(Å)	c(Å)	V (Å ³)	a (Å)	c(Å)
Zinc Oxide	3.2452	5.3006	48.3421	3.2498	5.2066

Table 3.2: Summary of the peak position and d-spacing of ZnO powder.

Film	Calculated			JCPDS: 36-1451		
ZnO	2 θ	(hkl)	d (Å)	2 θ	(hkl)	d (Å)
	31.7284	(100)	2.8179	31.7701	(100)	2.8143
	34.3923	(002)	2.6055	34.4423	(002)	2.6018
	36.26513	(101)	2.4751	36.2530	(101)	2.4759
	47.602	(102)	1.9087	47.5399	(102)	1.9111
	56.5825	(110)	1.6252	56.6034	(110)	1.6247
	62.8715	(103)	1.4769	62.8646	(103)	1.4771
	66.3867	(200)	1.4070	66.3874	(200)	1.4071
	68.0071	(112)	1.3773	67.9638	(112)	1.3781

The crystalline nature and the internal structure of the nanoparticles have been further investigated by HR-TEM. Figure 3.3 depicts the respective HR-TEM images of the nanoparticles obtained at their respective magnifications. It is clear from the low magnification images that the ZnO nanoparticles tend to agglomerate into larger particles. High magnification shows a random collection of small and larger pyramid-

shaped structures intermixed together which makes it tempting to link such a shape to the hexagonal wurzite confirmed by XRD results. The agglomeration suggests that the particle size of the ZnO nanoparticles might not be uniformly even.

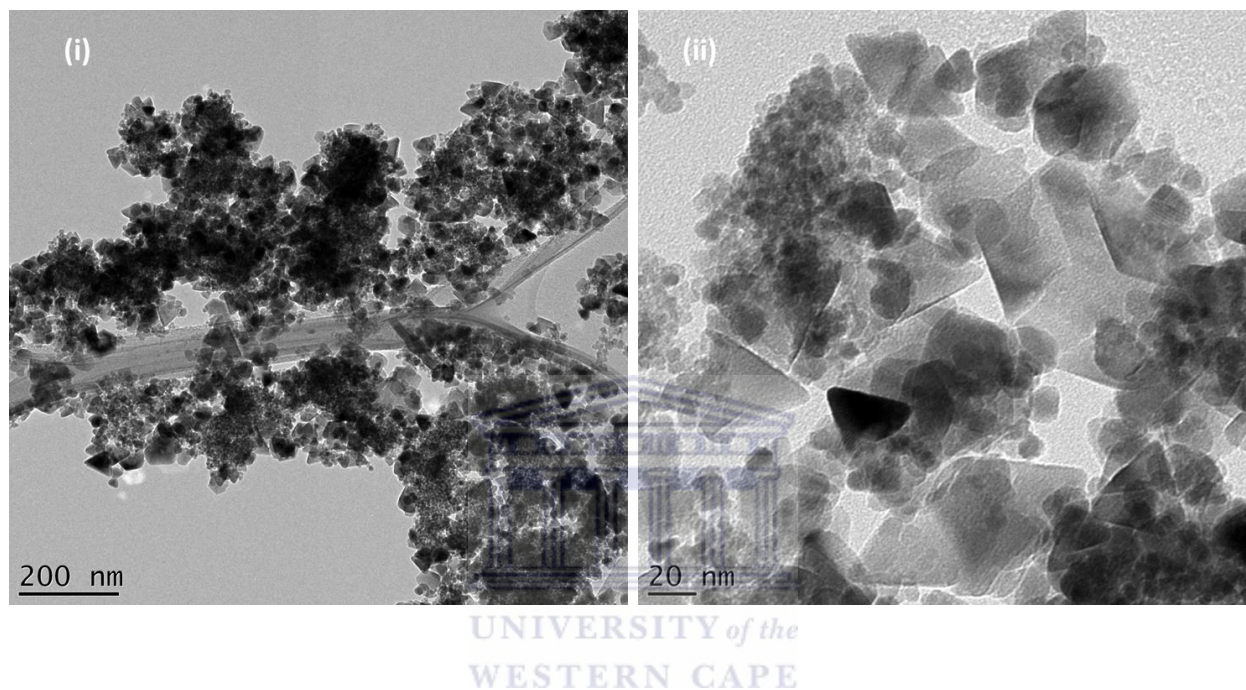


Figure 3.3: HR-TEM images of ZnO nanoparticles prepared with ethanol solvent, (i) Images taken at low magnification and (ii) high magnification image.

HRTEM nanoscale features of an individual ZnO nanoparticle in Figure 3.4 shows a polycrystalline lattice with d-spacing of 0.2768 nm, which is consistent with the (100) reflections of a hexagonal wurzite structure. This is consistent with the XRD results presented in table 3.2. From the diffraction rings of the SAED pattern shown in Figure 3.4b, (100), (002), (102), (110), (103) and (200) planes of the ZnO nanoparticles were identified.

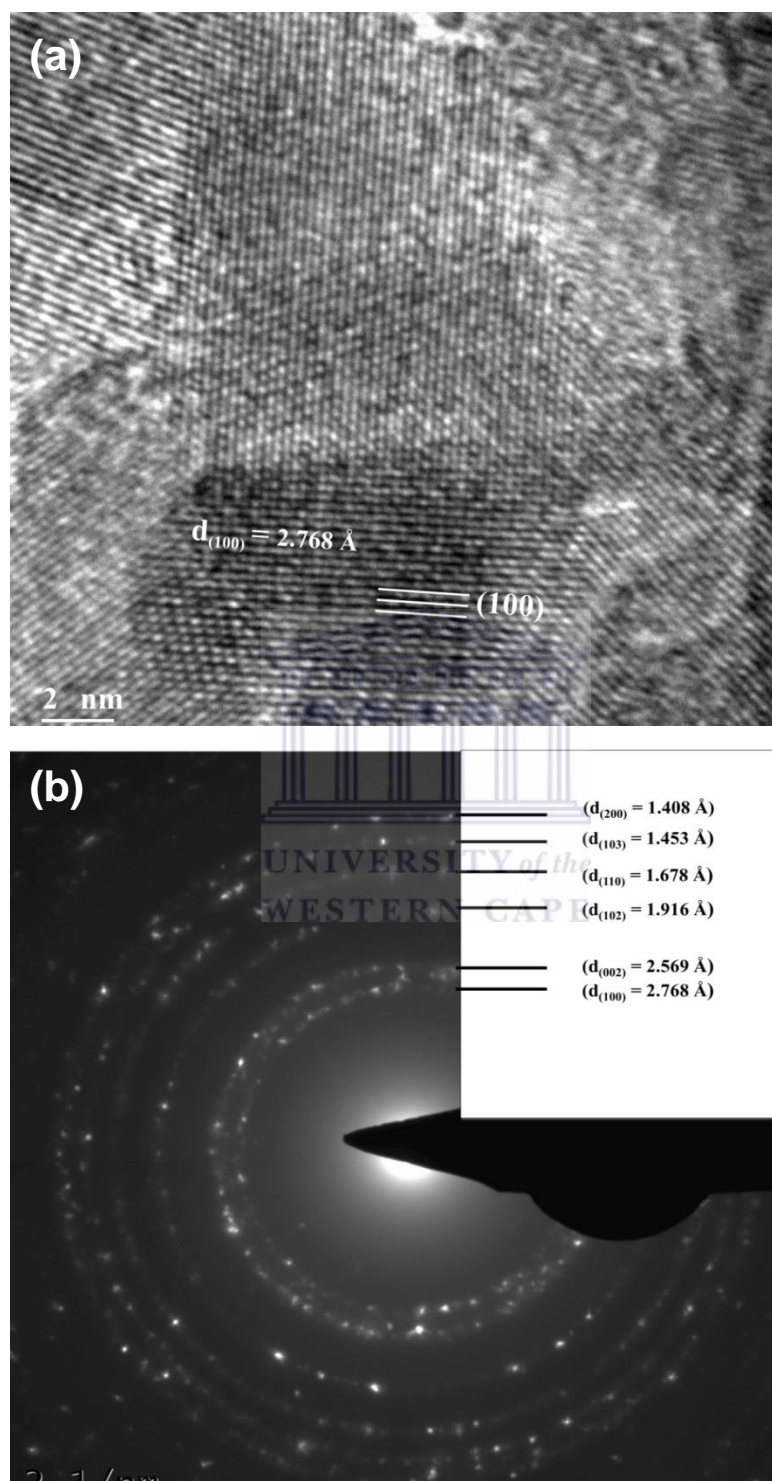


Figure 3.4: (a) HRTEM micrograph and (b) selected area electron diffraction (SAED) micrograph of a highly crystalline ZnO nanoparticle.

Table 3.3 displays the d-spacing data obtained by XRD and HRTEM and both techniques are in agreement; this comparison further confirms that the synthesized ZnO is indeed polycrystalline and has a hexagonal wurtzite structure.

Table 3.3: Comparison of d-spacing between XRD and HRTEM.

	XRD	HRTEM
(hkl)	d (nm)	d (nm)
(100)	2.817	2.768
(002)	2.606	2.569
(102)	1.908	1.916
(110)	1.625	1.678
(103)	1.476	1.453
(200)	1.407	1.408

Figure 3.5 shows the Raman spectrum of the ZnO nanostructures. The presence of a sharp, strong, non-polar optical phonon E_{2H} mode at 437 cm^{-1} shows that the products are wurtzite hexagonal ZnO structure. The presence of a high intensity E_2

mode and weak E_1 (LO) mode in the spectrum of ZnO structures indicates increased Raman scattering due to good crystal quality, and this is consistent with XRD results. Previous studies indicated that the E_1 (LO) mode at 583 cm^{-1} is derived from the formation of defects of oxygen vacancies [3.14]. Two very small peaks around 332 and 376 cm^{-1} are ascribed to the $E_{2H}-E_{2L}$ (multi-phonon) and A_{1T} modes; respectively [3.15 - 3.16].

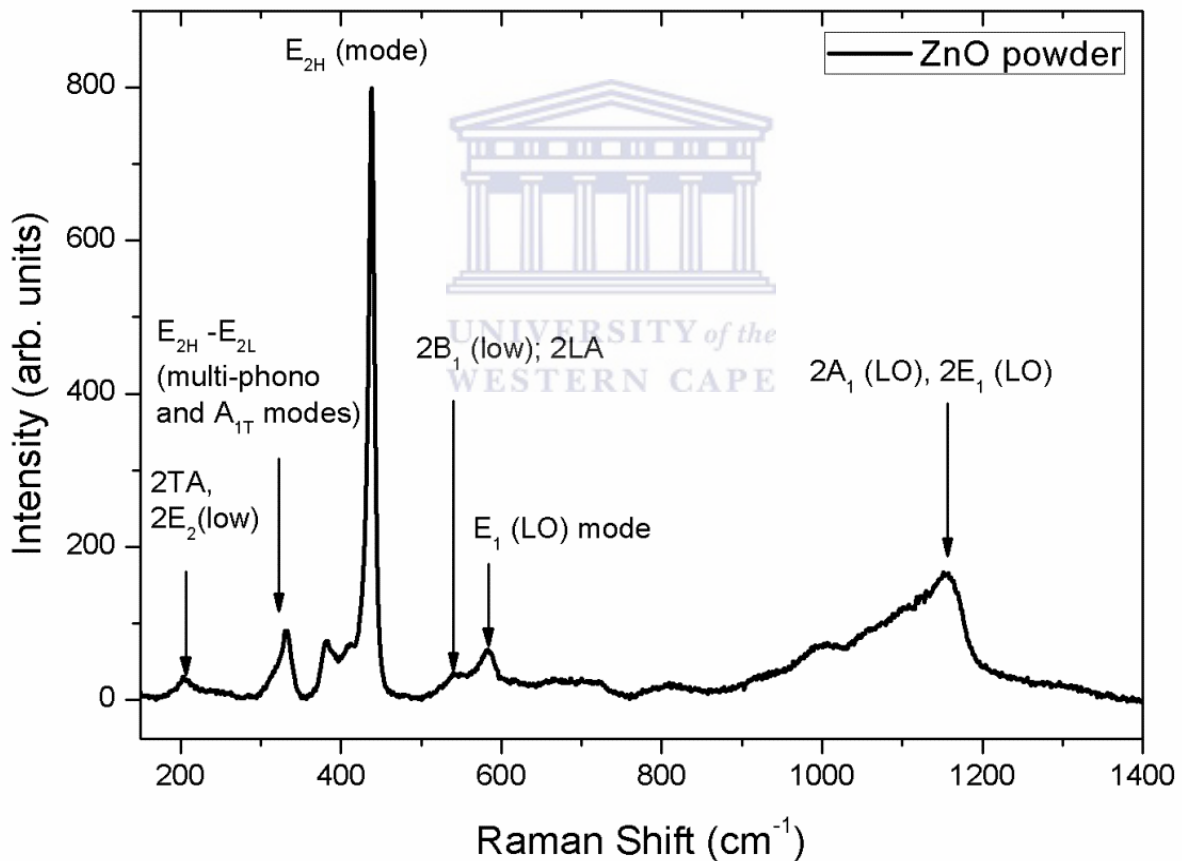


Figure 3.5: Raman spectrum of the as-synthesized ZnO-nanostructures.

3.3.3. Surface Morphology

Scanning electron microscopy (SEM) is a very important and useful tool to study the morphology of the crystals. Figure 3.6 displays the surface morphology of ZnO nanostructures spin coated on a silicon substrate as obtained from a field emission (FE)-SEM. The nanoparticles are agglomerated to one another and their shape was found to be spherical. The nanoparticles size range from 10 to 63 nm, with an average diameter of 37.02 nm.

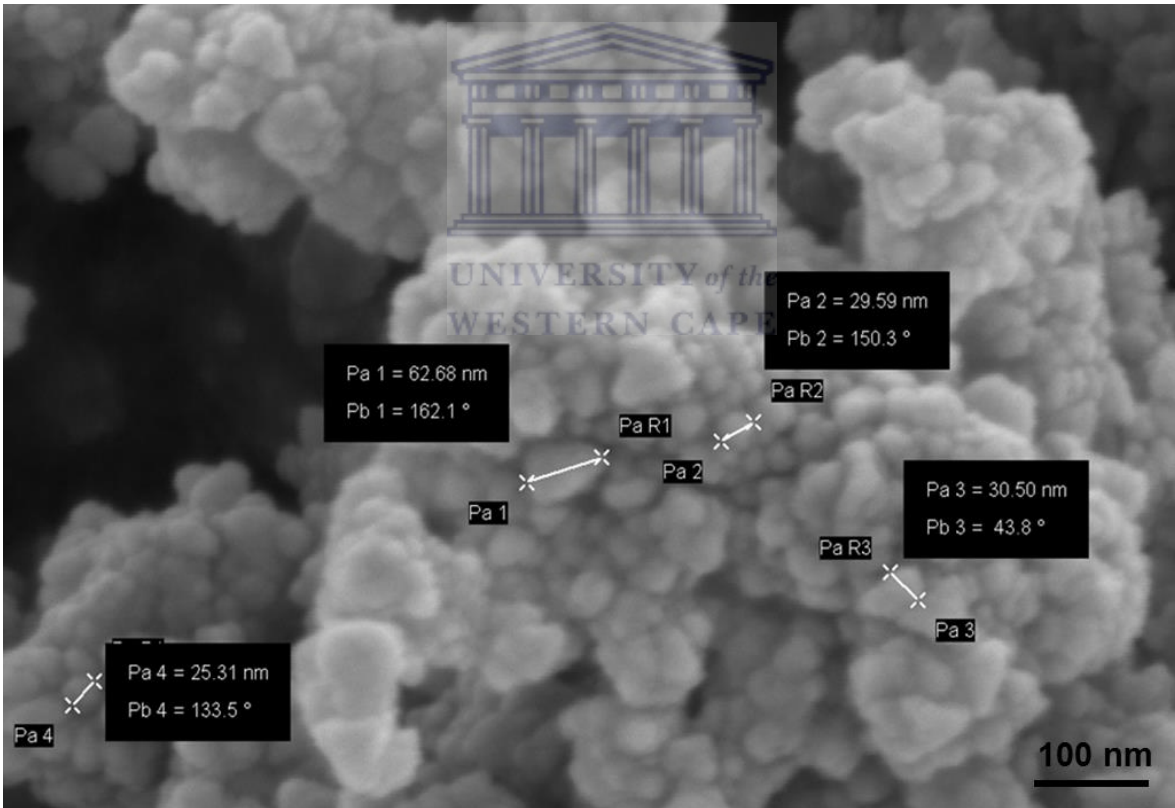


Figure 3.6: SEM image of zinc oxide nanoparticles.

EDX was used to confirm the presence of ZnO and to confirm that there were no undesirable chemical residues from the synthesis route remaining in the sample (figure 3.7). The EDX indeed confirmed the purity of the ZnO with no signals from impurity elements. The presence of Ni is accounted for, as a nickel grid was used.

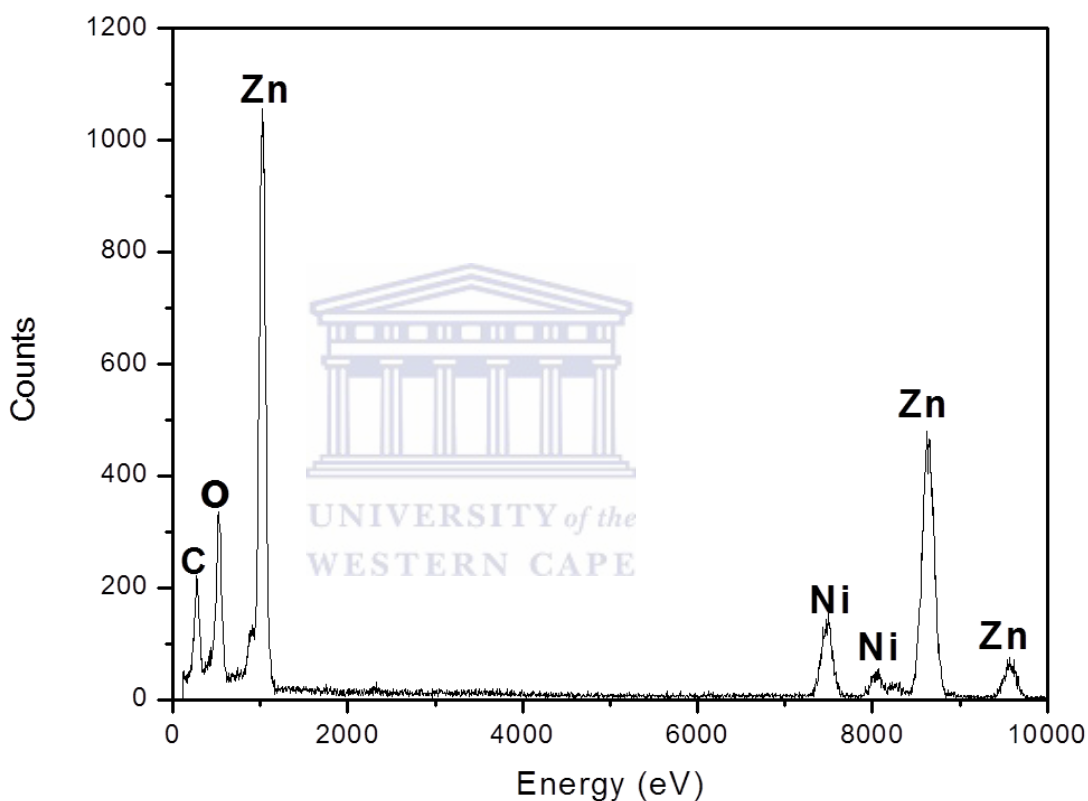


Figure 3.7: EDX spectrum of ZnO nanoparticles.

Figure 3.8 shows a representative XPS broad scan survey spectrum of the ZnO nanostructures which reveals only the elements Zn, O, and C. The detected carbon is related to the carbon tape used during the measurements and the carbon adsorbed on the surface during the exposure of the sample to the ambient atmosphere. It further

excludes the presence of any other impurities. Quantitative XPS analysis reveals that the ZnO films are stoichiometric with Zn/O atomic ratio very close to that of ZnO single crystal. XPS spectrum lines of O 1s and Zn were taken for quantitative analysis. The representative spectrum is shown in figure 3.8. As seen in the O 1s peak, there appears a shoulder on the high binding energy side of the main O 1s peak at ≈ 530.4 eV. The binding energy component (400 - 600 eV) can be attributed to oxygen zinc hydroxide $\text{Zn}(\text{OH})_2$ [3.17].

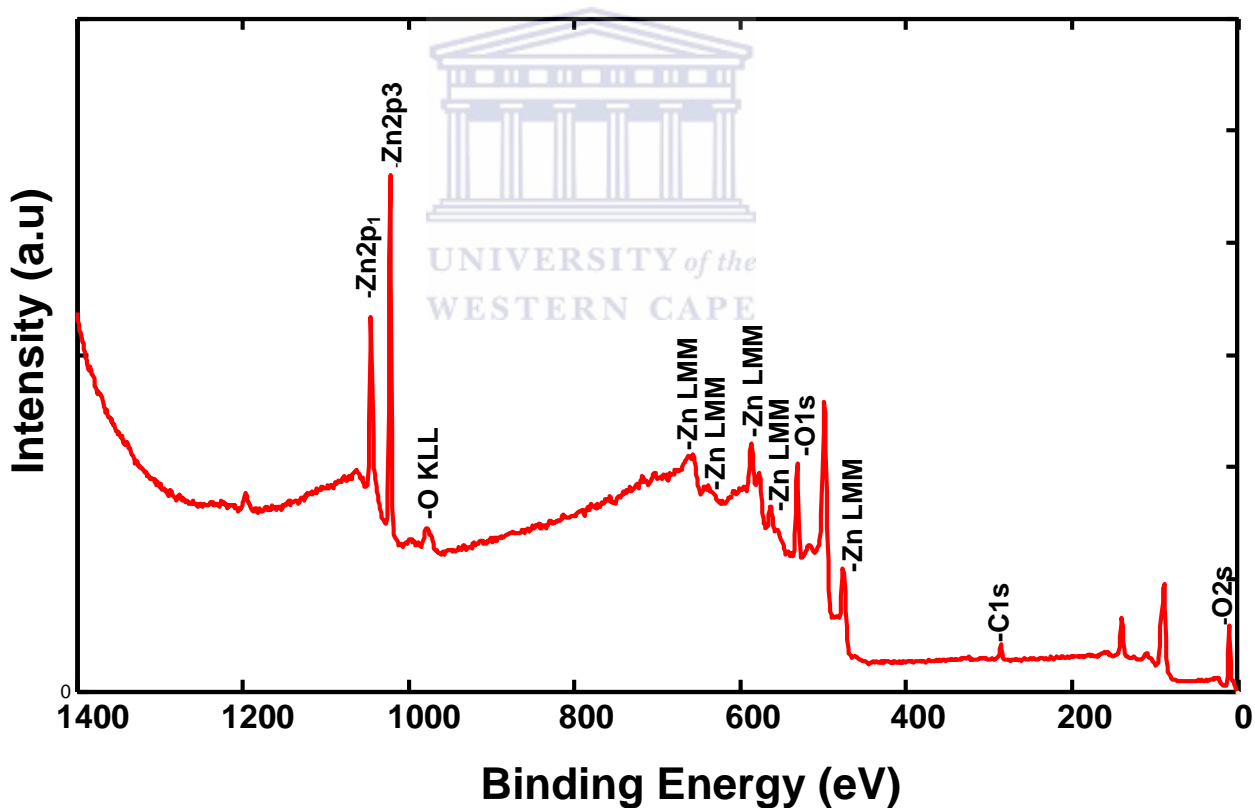
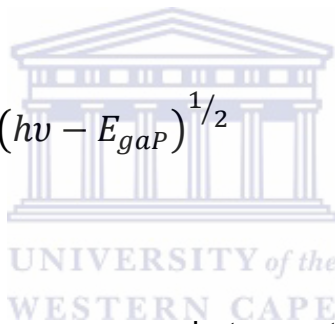


Figure 3.8: XPS survey scan of ZnO nanostructures.

3.3.4. Optical properties

Figure. 3.9 shows the UV-vis absorption spectrum of ZnO nanostructures. The absorption spectrum shows an absorption band around 360 nm, which blue-shifted relative to the bulk exciton absorption (373 nm) [3.18]. This blue-shift is due to the quantum confinement effect. The optical energy gap (E_{gap}) in Fig. 3.9 (b) was derived by assuming a direct electronic transition between the edges of the valence and conduction bands, for which the variation in the absorption coefficient with the photon energy $h\nu$ is given by [3.19]:

$$\alpha(h\nu) = A(h\nu - E_{\text{gap}})^{1/2} \quad (6)$$



E_{gap} denotes the optical energy gap between the valence and the conduction band. “Tauc” plots of α^2 versus $h\nu$; given by extrapolation of the linear region of the resulting curve, give a value for E_{gap} . The calculated value of the direct optical energy gap is 3.22 eV. The absorption edge is inversely proportional to the energy gap as demonstrated by the ZnO film absorption edge being higher to that ZnO powder.

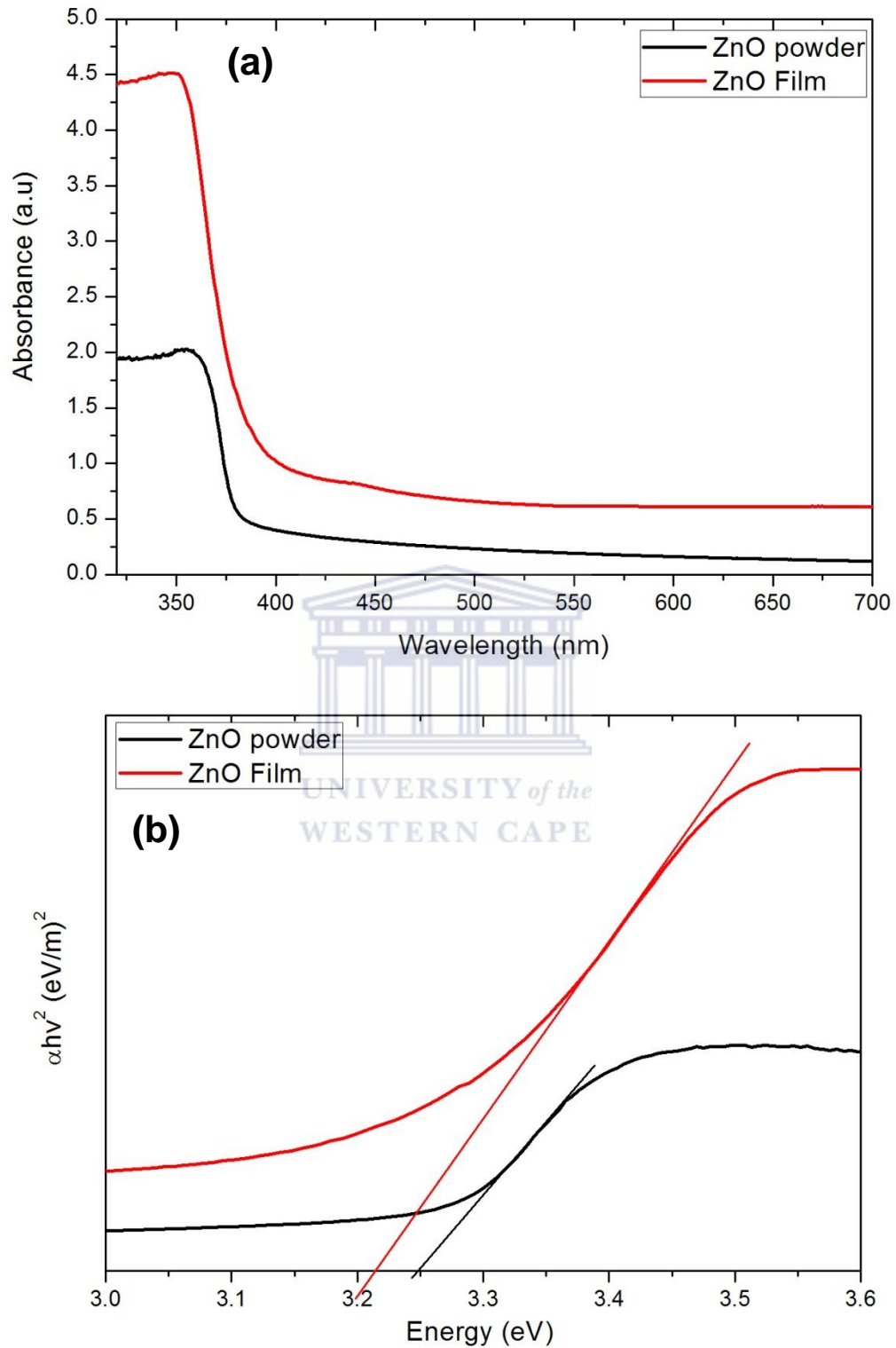


Fig. 3.9: (a) UV-Vis absorption of ZnO and (b) $(\alpha h\nu)^2$ versus photon energy ($h\nu$) plot

Photoluminescence (PL) is a process by which a substance absorbs photons and reradiates it through various mechanisms. Therefore this technique is widely used to investigate the energy levels of materials, thereby providing fundamental information on the electronic properties and impurity levels of these materials. Figure 3.10 demonstrates the PL spectrum of the ZnO nanostructures measured at room temperature with the excitation wavelength of 330 nm. The PL spectrum in Figure 3.10(a) and the de-convoluted spectra using Gaussian fit in Figure 3.10(b) exhibits an ultraviolet (UV) near-band-edge (NBE) emission at 390 nm and a blue emission band around 415 nm which is assigned to electronic transitions from the Zn interstitial levels (Zn_i) to the valence band [3.20]. A strong violet-blue emission centred at 445 nm is related to the interstitial zinc in the ZnO [3.21-3.22]. The de-convoluted spectrum in Figure 3.10(c) shows a defect related green-orange band around 480-750 nm. However, the origin of broad-band emission is still controversial and several kinds of defects and vacancies have been reported to be responsible for this emission such as oxygen vacancies with different charged states, zinc vacancies, zinc interstitial, and adsorbed molecules [3.23-3.25]. From Figure 3.10 (c) it can clearly be seen that the de-convoluted spectrum shows three peaks at ~480-545 nm, 545–605 nm and 605-750 nm related to singly ionised oxygen vacancies (V_O^+) and/or zinc vacancies (V_{zn}), doubly ionised oxygen vacancies (V_O^{++}) and oxygen interstitials (O_i) respectively.

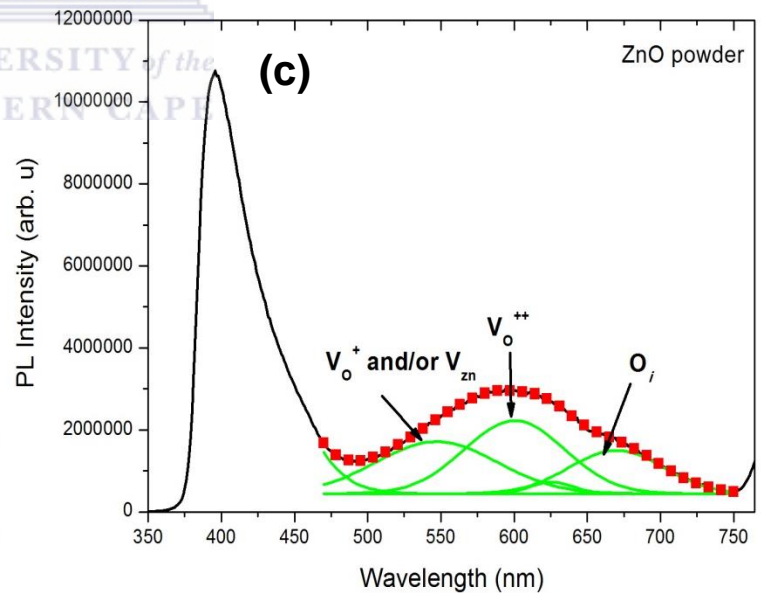
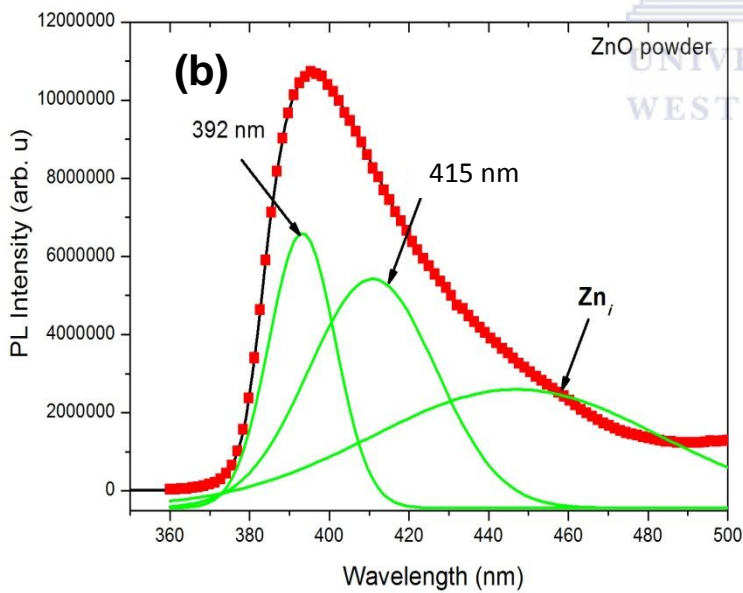
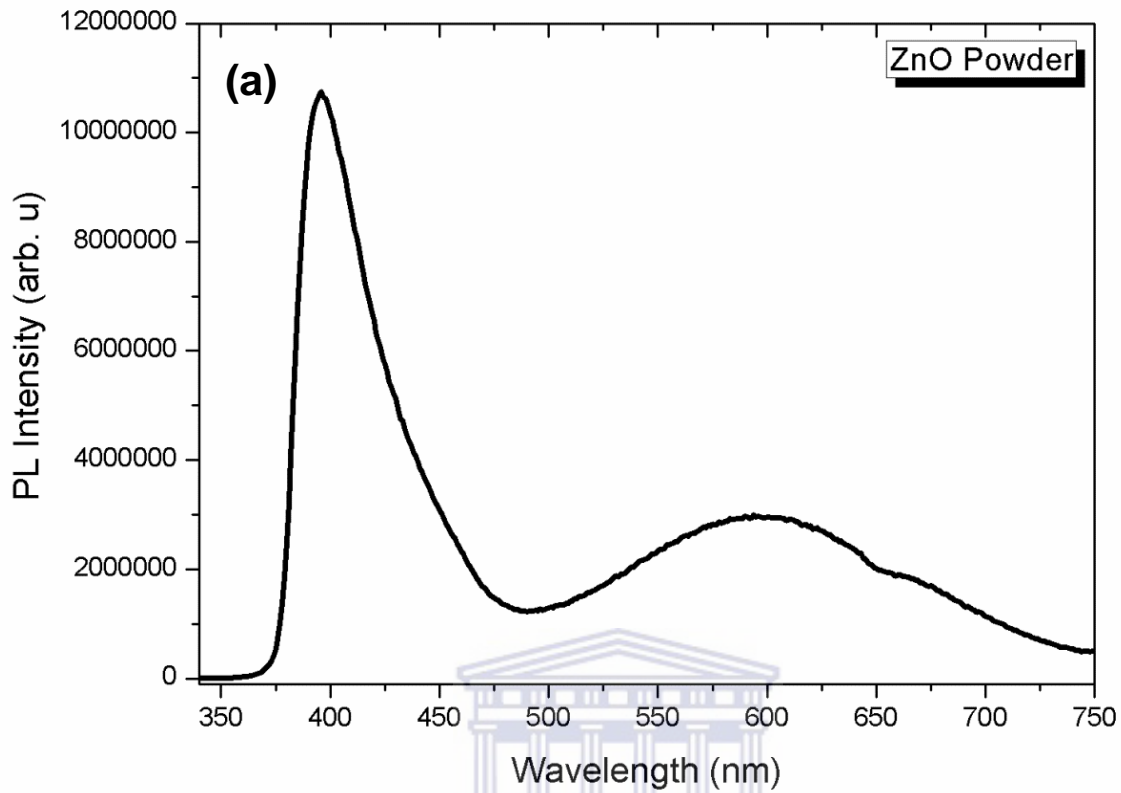


Figure 3.10: (a) Room-temperature PL spectrum of the as-prepared ZnO nanostructures, (b-c) Gaussian fits of each PL spectrum (the black lines are the experimental results and the red squares are Gaussian fits).

3.3.4.1. Reflectance Properties

Reflectance and transmittance properties of ZnO as a promising material for blue and ultraviolet light emitting devices are worth exploring, because of its wide-band gap of 3.37 eV and large exciton binding energy (60 meV). Thin films with embedded ZnO nanoparticles are found to be highly transparent throughout the visible region and the thermal stability is better. The optical absorption of the nanoparticles films in the UV region is quite high and this aspect highlights the prospects of applications of these films in hybrid solar cell devices.

From Figure 3.11, when ZnO is spin-coated on a bare silicon substrate the wavelength shift is insignificant but the reflectance decreases by a reasonable margin. Which suggest that the low reflectance of ZnO makes it a suitable candidate to absorb light. Furthermore, the sudden decrease of reflectance at a particular wavelength corresponding to the optical band-gap means that the particles are fairly enough distributed on the substrate after spin-coating[3.26].

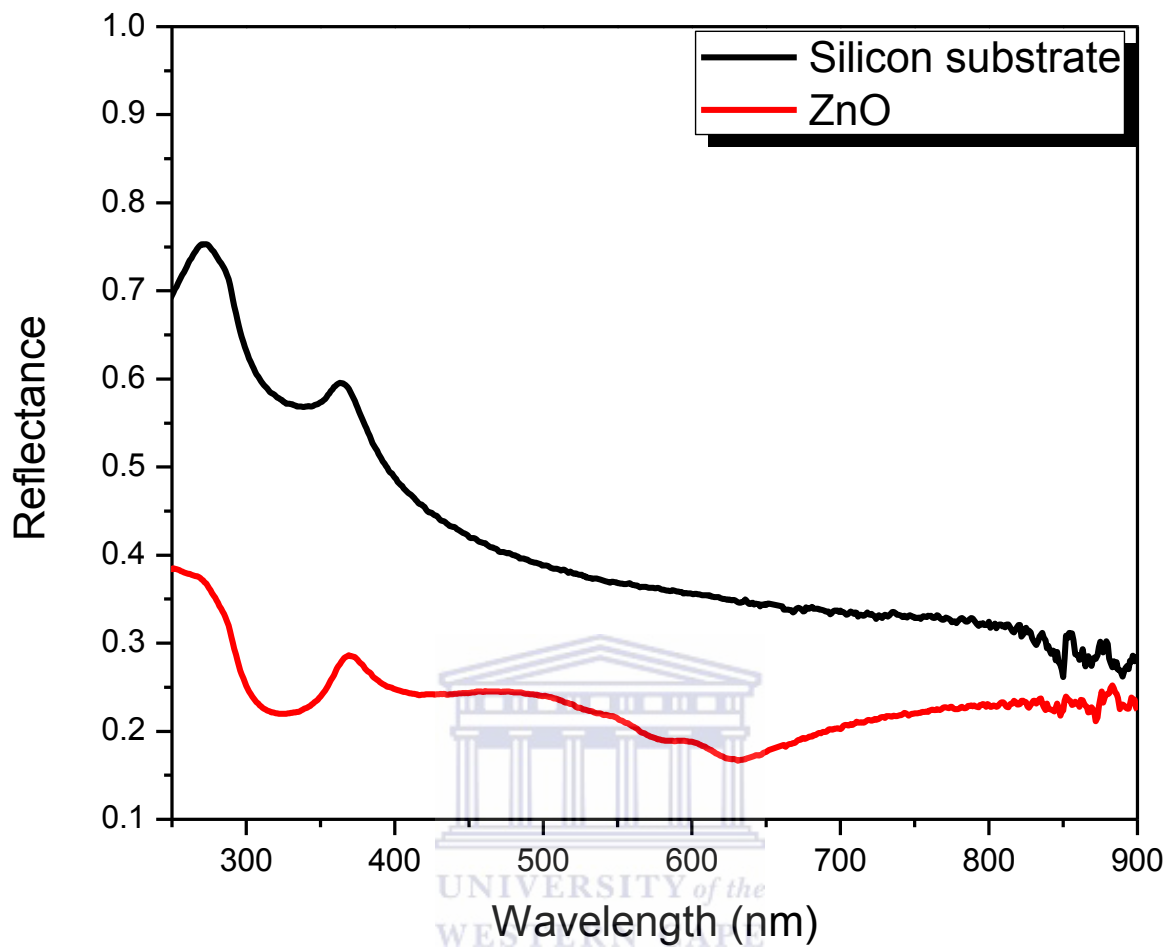


Figure 3.11: Reflectance spectra of ZnO on Silicon substrate.

3.3.4.2. Transmittance Properties

For ZnO to enhance a solar cell not only must it show low reflectance but it must also show less transmittance in order to ensure that absorbance takes place. Figure 3.12 show that the studied films have a high transmission coefficient in the visible and near-infrared range. In the visible domain, maximum transmittance is ranged between 85 and 90%. Therefore, the optical transmittance increase of 88% to 95% in the visible

range can be correlated with the improved crystallinity of ZnO nanoparticles. This assumption is in accordance with the results reported by Ramamoorthy *et al.* [3.27], which revealed that the ZnO films, with textured and better aligned nanoparticles have superior transmission as compared to randomly orientated nanoparticles and also have an improved electrical conductivity.

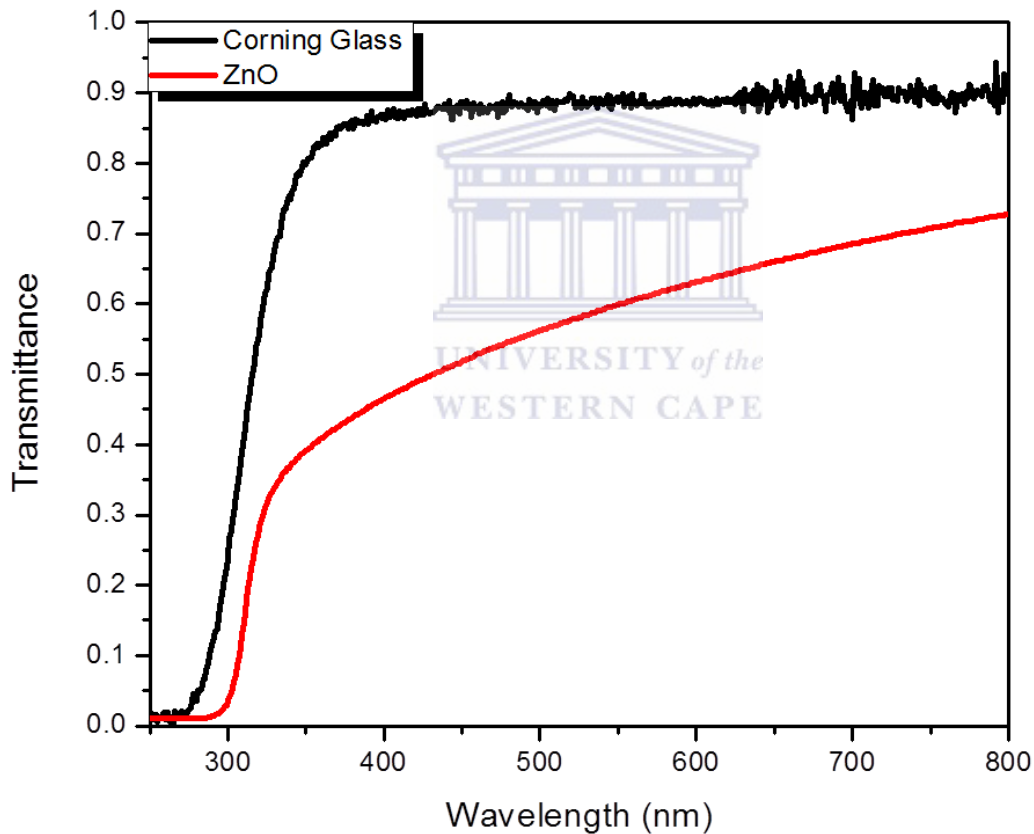


Figure 3.12: Transmittance spectra of ZnO on glass substrate.

3.4. CONCLUSION

The structural, optical and vibrational properties of ZnO were investigated using thermo-gravimetric analyses (TGA), x-ray diffraction (XRD), high-resolution transmission electron microscopy (HR-TEM), scanning electron microscopy, ultraviolet-visible (UV-VIS) spectroscopy, photoluminescence spectroscopy and Raman spectroscopy.

XRD results confirmed that the nanostructures are ZnO nanoparticles without any impurities and have a hexagonal wurtzite structure. HR-TEM and selected electron diffraction patterns also confirmed that the as-prepared materials are polycrystalline in nature. UV-vis absorption spectra showed that the absorption band of the ZnO is around 360 nm, which blue-shifted relative to the bulk exciton absorption (373 nm). This blue-shift is due to the quantum confinement effect. The optical properties of ZnO nanoparticles make it suitable for incorporation in the organic blends, which is explored in chapter 4.

3.5. REFERENCES

- [3.1] M.H. Huang, S. Mao, H. Feick, et al., *Science* (2001)
- [3.2] M.H. Koch, M. Janos, R.N. Lamb, et al., *J. Lightwave Technology*, (1998)
- [3.3] M. Mo, J.C. Yu, L. Zhang, S.K.A. Li, *Adv. Mater.* 17 (2005) 756.
- [3.4] S. Kar, B.N. Pal, S. Chaudhuri, D. Chakravorty, *J. Phys. Chem. B* 110 (2006) 4605.
- [3.5] B.P. Zhang, K. Wakatsuki, N.T. Binh, Y. Segawa, N. Usami, *J. Appl. Phys.* 96 (2004) 340.
- [3.6] G. Haiyong, Y. Fawang, L. Jinmin, Z. Yiping, W. Junxi, S. J. *Phys. D: Appl. Phys.* 40 (2007) 3654.
- [3.7] Y.W. Heo, V. Varadarajan, M. Kaufman, K. Kim, D.P. Norton, F. Ren, P.H. Fleming, *Appl. Phys. Lett.* 81 (2002) 3046.
- [3.8] Y. Tak, K. Yong, *J. Phys. Chem. B* 109 (2005) 19263.
- [3.9] D.E. Motaung, G.F. Malgas, C.J. Arendse, S.E. Mavundla, *Mater. Chem. Phys.* 135 (2012) 401.
- [3.10] K.J. Chen, T.H. Fang, F.Y. Hung, L. W. Ji, S.J. Chang, S.J. Young, Y.J. Hsiao, *Appl. Surf. Sci.* 254 (2008) 5791.
- [3.11] P. Rai, Jo, J.-N.; Lee, I.-H.; Yu, Y.-T. *Mater. Chem. Phys.* 124 (2010) 406.
- [3.12] J. Zhou, F. Zhao, Y. Wang, Y. Zhang, L. Yang, *J. Lumines.* 122-123 (2007) 195.
- [3.13] Z. M. Khoshhesab, M. Sarfaraz, and M. A. Asadabad, *Metal-Organic and Nano-Metal Chemistry* 41 (2011) 814.
- [3.14] G. J. Exarhos, S K. Sharma, *Thin Solid Films* 270 (1995) 27.
- [3.15] J.J. Wu, S.C. Liu, *J. Phys. Chem. B* 106 (2002) 9546.

- [3.16] Z. Yang, Z. Z. Ye, Z. Xu and B. H. Zhao, *Physica E: Low-Dimensional Systems and Nanostructures* 42 (2009) 116.
- [3.17] Suh, S., Miinea, L. A., Hoffman, D. M. et al., *J. Mater. Sci. Lett.* 20 (2001) 115.
- [3.18] D.E. Motaung, G.H. Mhlongo, S.S. Nkosi, G.F. Malgas, B.W. Mwakikunga, E. Coetsee, H.C. Swart, H.M.I. Abdallah, T. Moyo, S.S. Ray, *ACS Appl. Mater. Interfaces* 6 (2014) 8981.
- [3.19] X. Zhang, X.M. Li, T.L. Chen, J.M. Bian, C.Y. Zhang, *Thin Solid Films* 492 (2005) 248.
- [3.20] G.H. Mhlongo, D.E. Motaung, S.S. Nkosi, H.C. Swart, G.F. Malgas, K.T. Hillie, B.W. Mwakikunga, *Appl. Surf. Sci.* 293 (2014) 62.
- [3.21] X. Zhang, Y. Xia, T. He, *Mater. Chem. Phys.* 137 (2012) 622.
- [3.22] H.B. Zeng, W.P. Cai, J.L. Hu, G.T. Duan, P.S. Liu, *Appl. Phys. Lett.* 88 (2006) 171910.
- [3.23] B. Panigrahy, M. Aslam, D.S. Misra, M. Ghosh, D. Bahadur, *Adv. Funct. Mater.* 20 (2010) 1161.
- [3.24] Y.G. Sun, M. Fuge, N.A. Fox, D.J. Riley, M.N.R. Ashfold, *Adv. Mater.* 2005, 17, 2477.
- [3.25] A.B. Djuris̃ic, Y.H. Leung, K.H. Tam, Y.F. Hsu, L. Ding, W.K. Ge, Y.C. Zhong, K.S. Wong, W.K. Chan, H.L. Tam, K.W. Cheah, W.M. Kwok, D.L. Phillips, *Nanotechnology* 18 (2007) 095702.
- [3.26] L.I. Berger, *Semiconductor Materials*, CRC Press, Boca Raton, FL. (1997).
- [3.27] K. Ramamoorthy, C. Sanjeeviraja, M. Jayachandran, K. Sankaranarayanan, P. Misra, L.M. Kukreja, *Curr. Appl. Phys.* 6103 (2006)

CHAPTER 4

EFFECT OF ZnO AS AN ADDITIONAL ELECTRON ACCEPTOR ON THE PHOTOVOLTAIC PROPERTIES OF P3HT:PCBM: ZnO TERNARY STRUCTURE

4.1. INTRODUCTION

During the last decade, organic solar cells (OSCs) have attracted substantial research interest due to the numerous advantages they offer, namely low cost, light weight, large-area fabrication possibilities, and its mechanically flexibility [4.1 - 4.4]. The primary focus in OSC research is centred on improving the power conversion efficiency (PCE) and stability under simulated sunlight [4.5 - 4.9]. Bulk-heterojunction (BHJ) cells, consisting of an interpenetrating network of electron donor material such as poly(3-hexylthiophene) (P3HT) and acceptor material ([6,6]-phenyl- C₆₁-butyric acid methyl ester (PCBM) have already achieved PCE as high as 8.3% and 10% respectively [4.10-4.12].

However, this PCE is still limited compared to conventional silicon based PV cells. This is due to low mobility of charge carriers with a short exciton diffusion length in the active layer [4.13 - 4.14]. Hence, hybrid solar cells have been considered as one of the most promising concepts to address this shortcoming, allowing for organic semiconductor blends as above, mixed with inorganic nanostructures or nanoparticles. These nanoparticles will be used as additional acceptors of electrons released from the polymer donor material, with the hope to increase mobility, and ultimately the PCE. In addition, the successful development of hybrid solar cells with enhanced PCE will offer

less expensive devices as it employs low cost materials to enhance the PCE. Previous studies prepared ZnO nanoparticles through spin-casting from chloroform solution by blending with P3HT to form hybrid structure and reported an efficiency of about 0.59% [4.15]. Recent results showed high efficiencies of 3.39% in devices using ZnO nanoparticles with a modified anode material [4.16]. Ikram et al. [4.17] reported a PCE of about 2.83% using a P3HT:PCBM:ZnO ternary system. In this work we will demonstrate the effect of the incorporation of various concentrations of ZnO nanostructures into the P3HT:PCBM polymer matrix which, although similar in some respects to reference [4.17], utilizes the type of ZnO nanoparticles described in chapter 3 of this thesis, i.e. the pyramidal-shaped nano-ZnO grown in our laboratories. The surface morphological, structural, and optical property modifications upon the addition of ZnO to the P3HT:PCBM blend are studied in detail using XRD, HR-TEM, Raman, and UV-vis spectroscopy, and they are correlated with the photovoltaic properties. In addition the effect of solvent on the properties of the active layer is also studied.

4.2. SAMPLE PREPARATION

Sample preparations were done according to the following procedure. Indium tin oxide (ITO)-coated glass, Corning 7059 glass and silicon (Si) substrates were ultrasonically cleaned with in acetone and isopropanol, and then rinsed in de-ionized water. Photoactive layers were prepared by mixing P3HT (5 mg or a weight percentage of 50%) with PCBM (5 mg), and blending them with different wt. ratios (5 mg and 10 mg) of ZnO and dissolving the constituents in either chloroform or dichlorobenzene solution. A complete dissolution between the blends and hybrid structures was attained

by stirring the solutions overnight at 50 °C. For solar cell preparation the active layers of P3HT:PCBM and P3HT:PCBM:ZnO with different ZnO concentrations (0.2-3 wt. ratio) were deposited on a thin layer (90 nm) of TiO₂, giving a thickness in the range of 100-120 nm. The spinning rate and time of spin-coating were between 2500 and 3000 rpm and 30 s respectively. See section 4.3.3.4 for a comprehensive description of solar cell preparation.

4.3. RESULTS AND DISCUSSION

4.3.1. Thermal Analysis

Thermo-gravimetric analysis (TGA) was used to characterize the thermal stability of P3HT blended with PCBM and various ZnO concentrations. The TGA analysis shows three decomposition temperatures for the P3HT and its blended structures. The first stage of decomposition is mild and it occurs around 150-300 °C with a maximum weight loss of <1%. The first decomposition is ascribed as detachments of lighter fragments like C-S units, which are followed by the abstraction of hydrogen attached to a carbon atom that is adjacent to a double bond, leading to backbone, side chain and sulphur oxidations [4.18]. A significant degradation is observed around 395-500 °C, with the weight loss of 60% for P3HT and 40 % for P3HT:PCBM and the hybrid P3HT:PCBM:ZnO (1:1:0.2 and 1:1:1 wt. ratio). In contrast the P3HT:PCBM:ZnO (1:1:2 wt. ratio) showed only 10% degradation. The final degradation occurs around 505 °C with a weight loss of <38% for P3HT and >50% for the P3HT:PCBM and P3HT:PCBM:ZnO (1:1:0.2 wt. ratio), while the P3HT:PCBM:ZnO (1:1:1 and 1:1:2 wt.

ratios) showed a final weight loss of $\geq 30\%$ respectively. This degradation is related to the decomposition of the thiophene rings (main chains) in the polymeric materials [4.19]. Therefore, we can conclude that the P3HT becomes more stable with the increase in the concentration of ZnO.

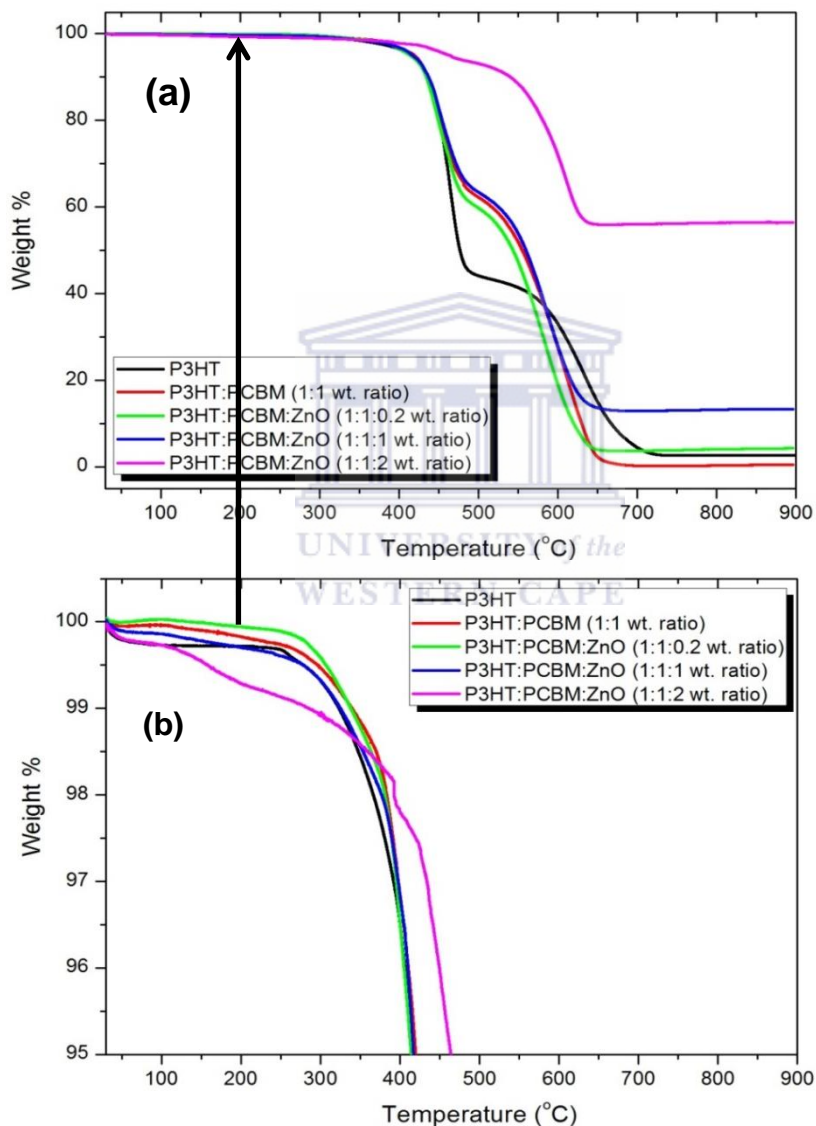


Figure 4.1: TGA of (a) P3HT and its blends, and (b) corresponds to the inset of Figure 4.1a.

4.3.2. Effect of chloroform as a casting solvent

4.3.2.1. Structural properties

Fourier transform infrared spectroscopy (FTIR) has proven to be a very influential technique in investigating the transformation in the chemical structure of P3HT, P3HT:PCBM and different ratios of the P3HT:PCBM:ZnO hybrid. Figure 4.2 depicts the raw absorbance spectrum of a P3HT thin film, prepared with chloroform as solvent. Table 4.1 gives a summary of the absorption bands for P3HT thin film. The peaks at 731 cm^{-1} and 819 cm^{-1} (not observed in our results, but visible in Figure 4.2b [4.20]) are assigned to the CH_3 rocking vibrations and C-H out of plane mode respectively. The bands at $1045\text{-}1100\text{ cm}^{-1}$ are assigned to $\text{C}=\text{S}^+-\text{O}^-$ residues [4.21]. The absorption band at 1460 cm^{-1} is attributed to the C-C symmetric stretching mode while the anti-symmetric stretching mode C=C peak is at 1509 cm^{-1} . Finally, the absorption bands at 2858 cm^{-1} and 2937 cm^{-1} are assigned to the CH_2 in-phase stretching mode and CH_2 out-of-phase stretching mode respectively [4.20].

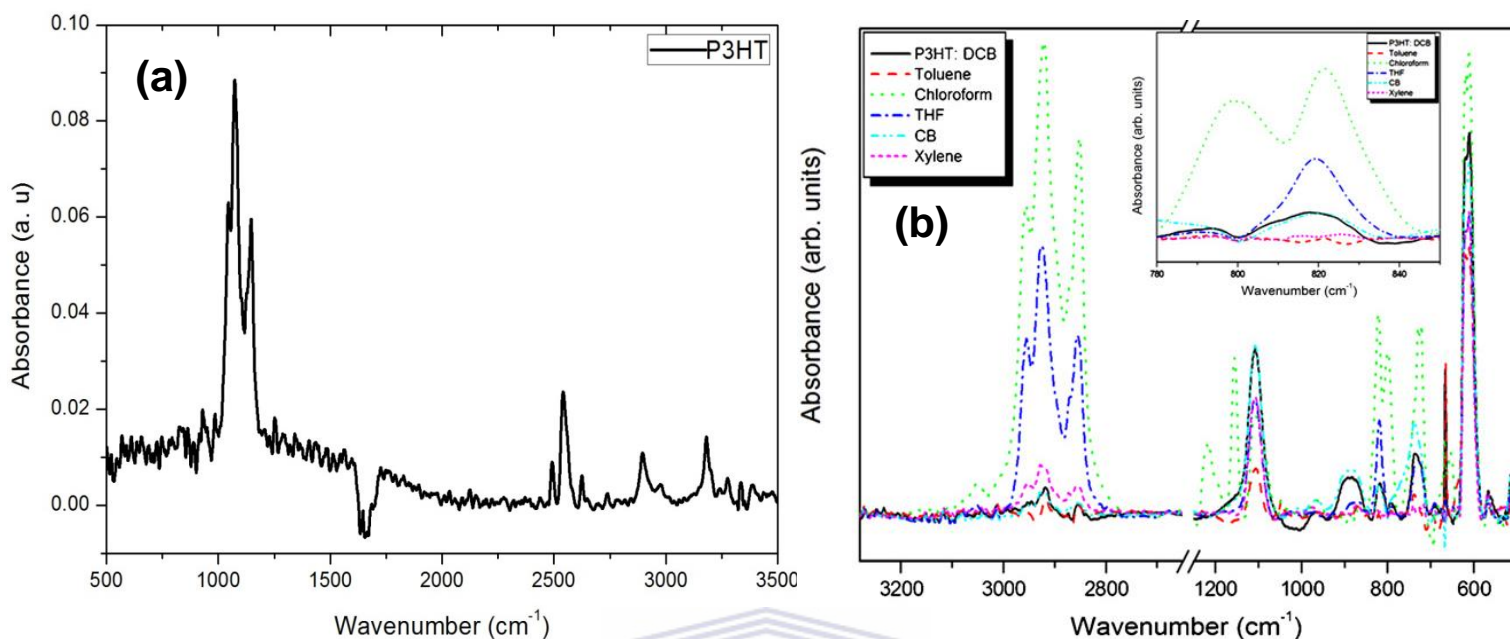
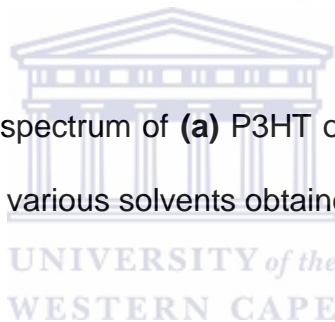


Figure 4.2: FTIR absorbance spectrum of (a) P3HT obtained from our results and (b) P3HT dissolved in various solvents obtained in ref [4.20].



Furukawa et. al. [4.22] suggested that the effectiveness of the conjugation length of the backbone can be estimated by calculating the ratio (R) of the asymmetric C=C stretching peak to the symmetric C-C stretching peak. The average conjugation length of a polymer can be defined as the length over which the backbone planarity is maintained without interruption and this defines the chemical group that gives colour to a molecule, and hence the effective conjugation length along the polymer backbone of P3HT can be interpreted as the length of a completely undisturbed alternating single bond/double bond segment, being planar and allowing maximum overlap of the π -electrons. This can be represented by:

$$R = \frac{I_{1509}}{I_{1460}} \quad (4.1)$$

Where I_{1509} is related to the intensity of antisymmetric stretching mode C=C peak while I_{1460} is related to intensity of C-C symmetric stretching mode. Therefore from this equation the calculated R-value for P3HT amounts to 0.42 and remains constant after blending with an equal weight percent of PCBM and incorporating different ratios of ZnO, which suggest that the effective conjugation length of the P3HT is not altered and therefore our results suggest that the structural order of the P3HT is maintained.

Table 4.1: FTIR absorption bands and assignments for P3HT.

P3HT wavenumber (cm ⁻¹)	Assignment
731	CH ₃ rocking vibrations [4.20]
819	C-H out of plane mode
1460	C-C symmetric stretching mode
1509	C=C antisymmetric stretching mode
2858	CH ₂ in-phase stretching mode
2937	CH ₂ out-of-phase stretching mode

Shrotriya et al. [4.23] suggested an alternative approach to investigate charge transfer by studying the shift in position of the absorption band assigned to the C-H deformation vibration associated with the thiophene ring in P3HT. To investigate the evolution of the structural properties upon blending the P3HT with PCBM and various concentrations of ZnO, FTIR analysis was carried out (Figure 4.3). Therefore, the shift in the position of the 823 cm^{-1} peak can be used to study the charge transfer process in P3HT:PCBM:ZnO.

The dominance and chemical structure of P3HT are illustrated by the symmetric shape of the peak at approximately 819 cm^{-1} as shown in Figure 4.3b. The P3HT shoulder at 823 cm^{-1} does not vary much for the 1:1:1 wt. ratio hybrid but shifts to higher wavenumber when the ZnO weight ratio increases by a factor of 3, denoting that incorporation of ZnO in the polymer matrix has altered the P3HT structure. In addition, the peak intensity at 1075 and 1150 cm^{-1} increases with an increase in ZnO concentration inside the polymer (figure 4.3c). This change in vibration energy might be due to the charge transfer that occurs between the sulphur atom in P3HT, PCBM and ZnO molecules.

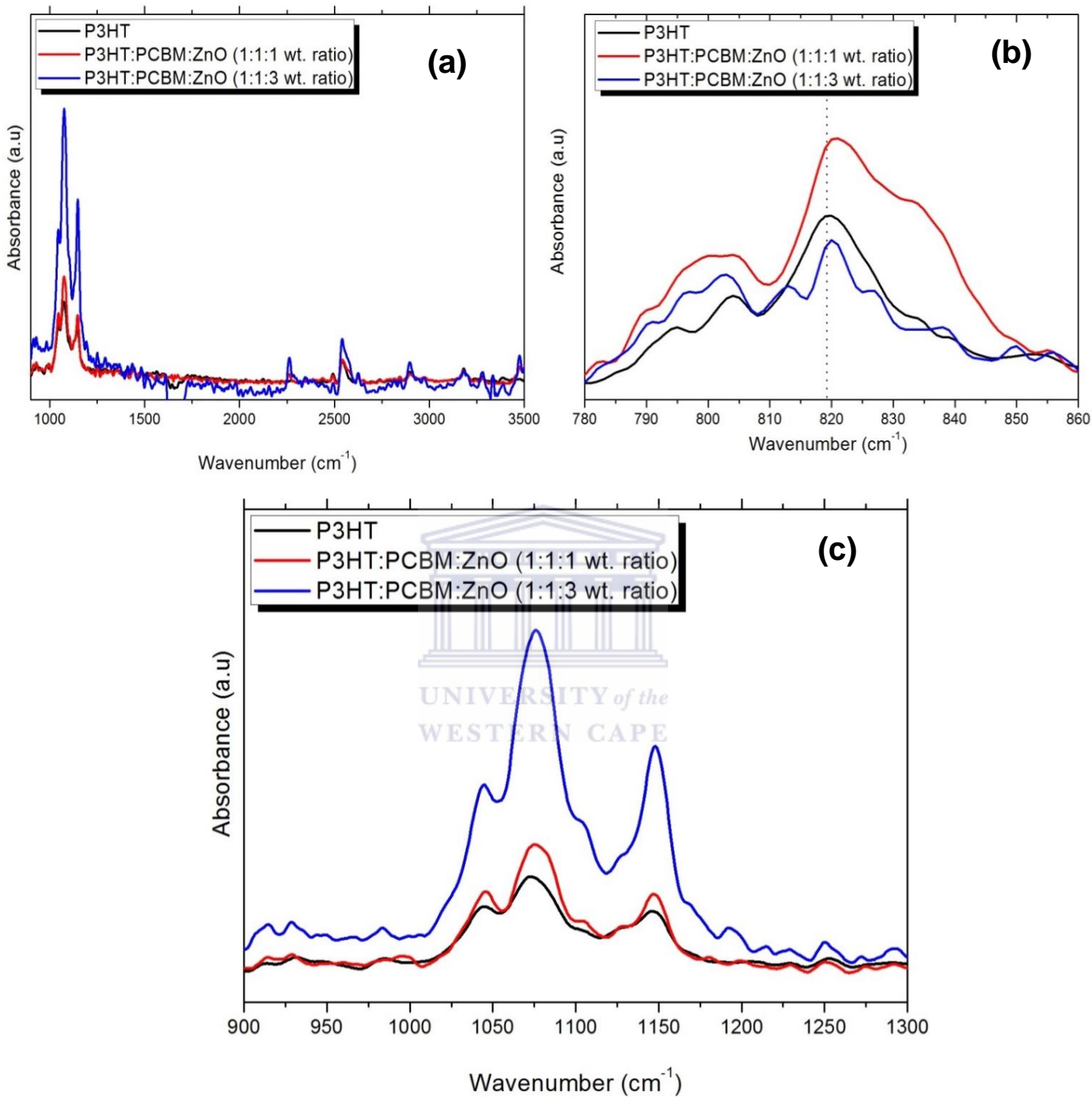


Figure 4.3: FTIR absorbance spectra of (a) P3HT and P3HT:PCBM:ZnO hybrids, (b) and (c) corresponds to an inset of Fig. 4.3 (a).

4.3.2.2. Surface morphology

It is well known that the organic solar cell performance is highly dependent on the surface morphology. Therefore scanning electron microscopy (SEM) was used to investigate the effects of chloroform as a solvent on the morphology of P3HT and P3HT:PCBM:ZnO hybrids. Figure 4.4a shows the morphology of P3HT and it should be noted that chloroform as a solvent has low ability to break the thiophene bond [4.24]. Figure 4.4b shows an SEM image of P3HT:PCBM:ZnO (1:1:1 wt. ratio) material; note the unevenly distributed material through the film. This lack of distribution can be associated with the inability of the chloroform to properly dissolve the material. This necessitated a further investigation into the surface morphology of the material by atomic force microscopy.

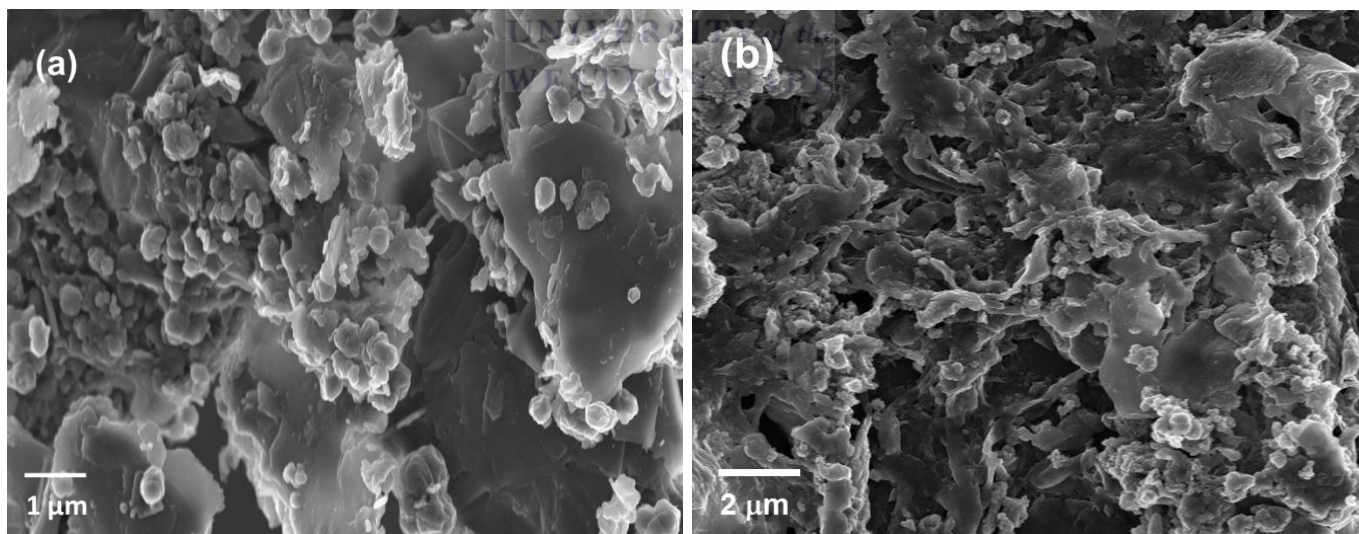
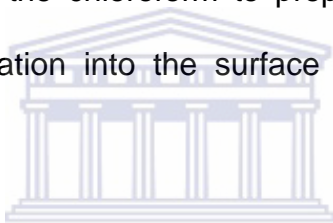


Figure 4.4: Scanning electron microscope image of (a) P3HT and (b) P3HT:PCBM:ZnO films spin-coated from a chloroform solvent.

Atomic force microscope (AFM) analyses were carried out to complement the SEM results on the effect of solvent on different materials (pristine P3HT, P3HT:PCBM and different hybrids structures). Figures 4.5 and 4.6 show the topographic images of the above mentioned materials in 2D and 3D. Table 4.2 shows the summary of the root mean square surface roughness (rms) values of pure P3HT and its blended films. It is clear from Figure 4.5(a) and (b) that the pure P3HT depicts a smooth surface resulting in an average roughness of 0.81 nm. However, the blended film of equal ratio of P3HT:PCBM shows small particles across the film surface (Figure 4.5c and d). When incorporating the ZnO in a 0.2:1:1 wt. ratio more particles are observed which results in an rms of 12.81 as shown in Figure 4.6a and b. Figure 4.6c and d shows that when increasing the loading of ZnO in the polymer matrix much coarser texture with broad “hill-like” features and an increased surface roughness compared to the other films are observed. This is most likely due to an even distribution of ZnO and disordered structure formation in the film [4.25]. It has been reported that a rougher interface between the photo-active layer and the top electron extraction layer can improve efficiency of organic solar cell devices by increasing light harvesting in the photo-active layer and by subsequently preventing the formation of shunt paths [4.26-4.29]. Moreover, it should be noted that a higher degree of surface roughness may result in a large scale phase-separation between the donor and the acceptor material. This can clearly be justified by SEM analysis in Figure 4.4, revealing larger aggregates across the film offering an inappropriate morphology for charge transport. As a result, most of the photogenerated holes simply recombine with electrons which transport through the polymer-rich matrix phase leading to a lower PCE. Therefore it can be concluded that samples spin-coated

from chloroform offers inappropriate morphology due to its lower solubility in P3HT and ZnO, hence a dichlorobenzene solvent will be used due to its better solubility in P3HT and fullerenes as previous reported by Motaung et al. [4.20]. Moreover, high ZnO ratios will be used for ZnO in DCB since they lead to better crystallinity and improved PCE, (to be discussed in section 4.3.1 to 4.3.4).

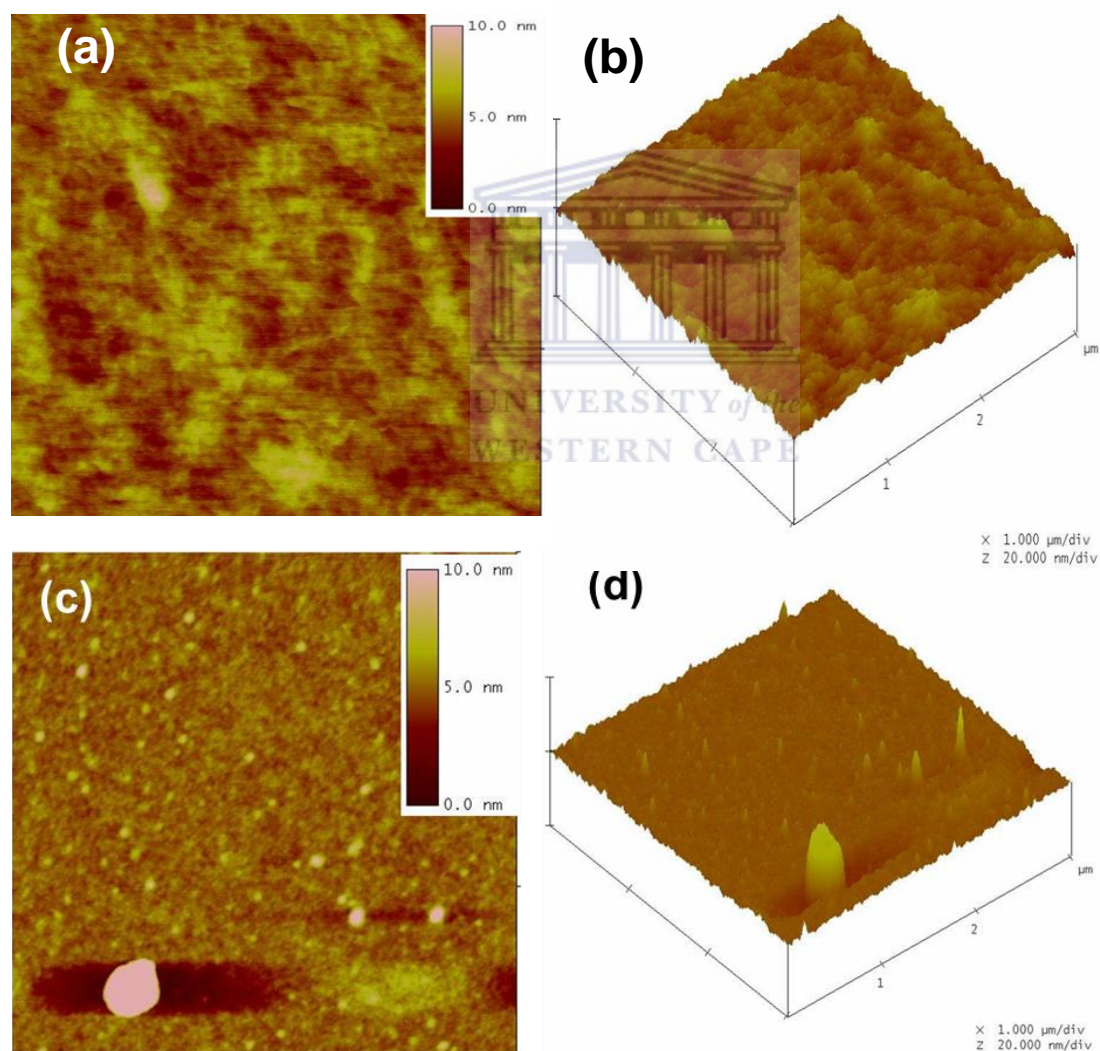


Figure 4.5: AFM height and 3D images of (a-b) P3HT and (c-d) P3HT:PCBM blend.

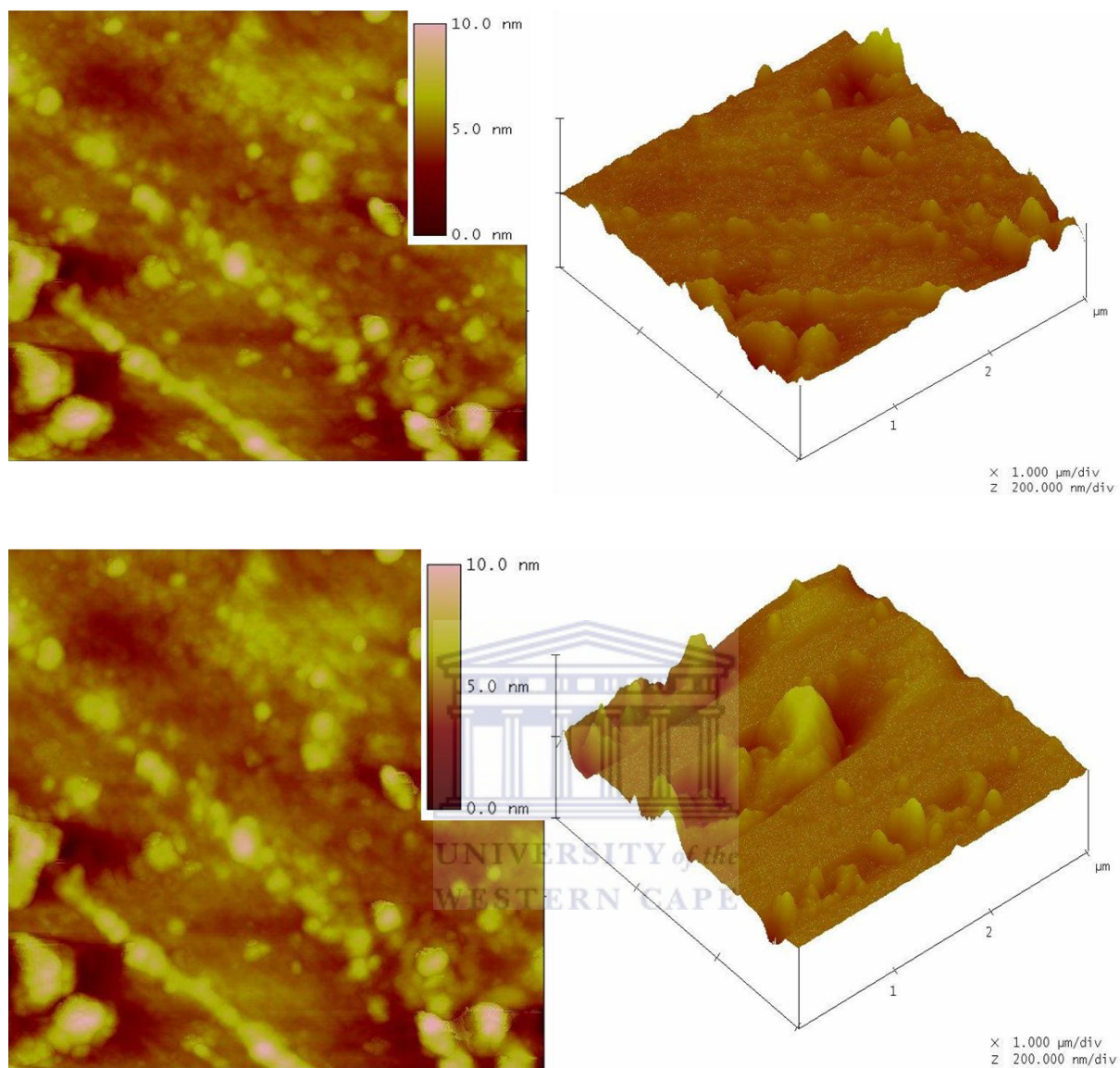


Figure 4.6: AFM height and 3D images of (a-b) P3HT:PCBM:ZnO (0.2:1:1 wt. ratio) and (c-d) P3HT:PCBM:ZnO (1:1:0.4 wt. ratio).

TABLE 4.2: Summary of rms values extracted from AFM measurements in P3HT and blended films.

Materials	RMS value (nm)
P3HT	0.812
P3HT:PCBM (1:1 wt. ratio) BLEND	1.196
HYBRID (1:1:0.2 wt. ratio)	12.808
HYBRID (1:1:0.4 wt. ratio)	15.182

4.3.3. Effect of 1, 2 dichlorobenzene as a casting solvent

4.3.3.1. Structural properties



To study the structural properties such as chain orientation and crystallinity of the polymer blends and hybrid films, the X-ray diffraction (XRD) measurements were carried out. Figure 4.7 shows the XRD patterns of polymer blends and hybrid inorganic-organic films prepared by the spin-coating method. The diffraction peak around $2\theta = 5.4^\circ$ can be attributed to a (100) reflection, which corresponds to an ordered self-organized structure with an interlayer spacing formed by parallel stacks of P3HT main chains, separated by regions filled with alkyl side chains [4.30]. It is evident that a peak shift to smaller angle occurs when PCBM is mixed into the polymer, with a hump occurring due to the broadening of the peak; this indicates an interference with the ordering of the P3HT due to the introduction of PCBM into the matrix [4.31 - 4.32].

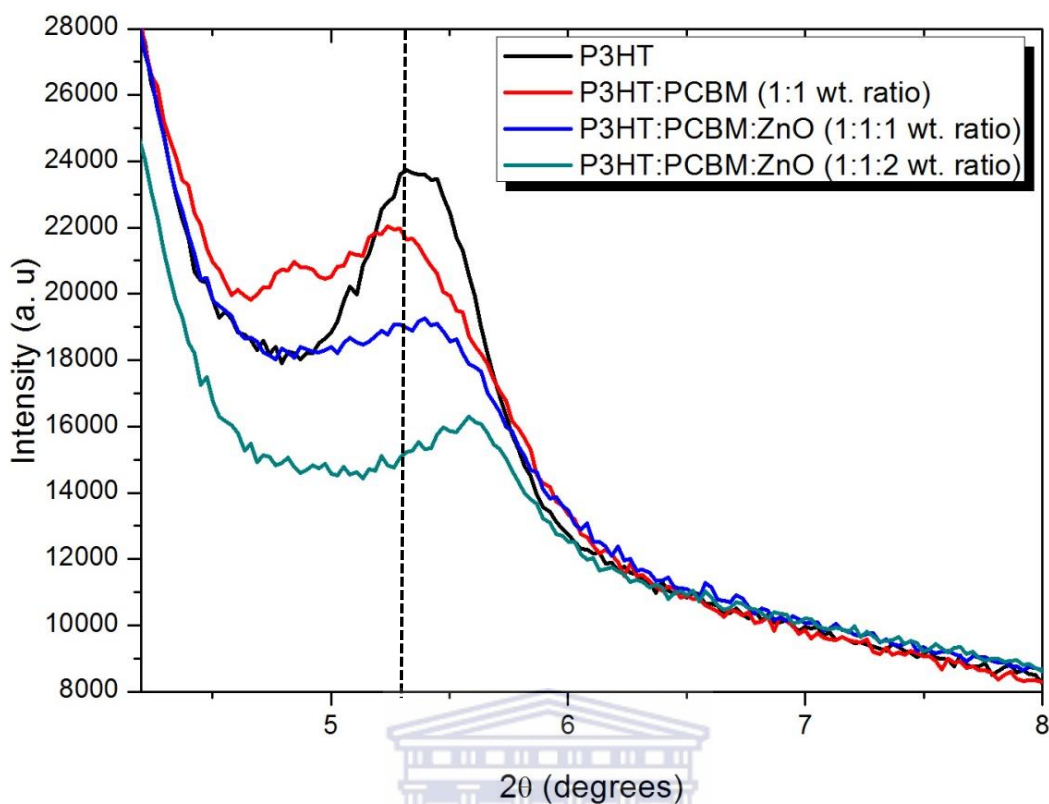


Figure 4.7: XRD patterns of P3HT and its blended films.

Table 4.3 gives a summary of the calculated peak information of P3HT, the equal ratio P3HT:PCBM blend and ZnO:P3HT:PCBM hybrid thin films. These calculations were performed using equations (3.2) and (3.3) (refer to chapter 3). Blending P3HT with PCBM create a shift to lower 2θ angles and allows for the side groups to incline leading to crystallinity during film deposition [4.33]. However, when ZnO is introduced the 2θ angles recover by shifting towards higher 2θ angles. Furthermore, for P3HT:PCBM, grain sizes could not be estimated due to the overlapping peaks. The film thickness obtained using spectroscopic ellipsometer [34] also decreases by a factor of 2 when PCBM is introduced. However, introducing ZnO regains the thickness by a small margin. By increasing the ratio of ZnO the thickness further increases.

Table 4.3: Summary of peaks positions, d-spacing and grain sizes of P3HT and its blended films estimated from XRD results.

P3HT:PCBM: ZnO (weight ratio)	Thickness (nm)	<100> 2θ position ($^{\circ}$)	d-spacing (nm)	Estimated grain size (nm)
1:0:0	84.5	5.39	1.63	17.50
1:1:0	43.9	5.32	1.62	-
1:1:1	48.1	5.45	1.62	12.23
1:1:2	49.2	5.61	1.58	16.36

The morphology of P3HT, the P3HT:PCBM blend and the hybrid P3HT:PCBM:ZnO was investigated to understand the characteristics of the active layer, and the possible impact on final solar cell performance. Figure 4.8 shows the TEM micrographs of the surface of P3HT:PCBM blended drop-coated onto copper grids. It is clear from Figure 4.8a that the high resolution image of pure P3HT shows hexagonal structure and this is confirmed on the Fourier transform image, see inset in Figure 4.8b. In addition, the hexagonal behavior is still maintained after P3HT is blended with PCBM and ZnO nanoparticles as shown in Figure 4.8c. The Fourier transform micrograph in Figure 4.8d, inset, clearly shows that the structure is mostly polycrystalline in nature and this is consistent with the XRD results.

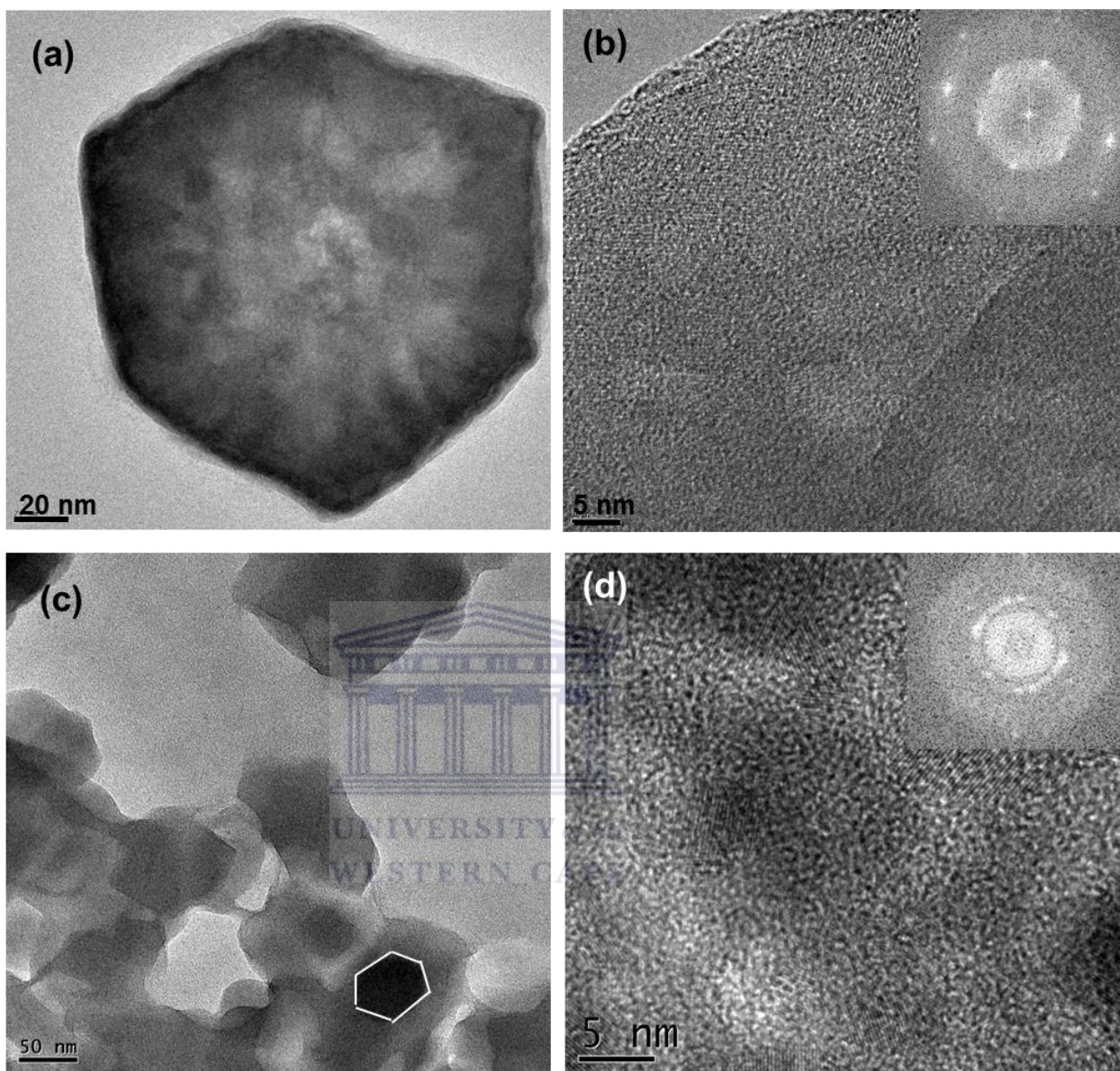


Figure 4.8: HR-TEM micrograph of (a-b) P3HT and (c-d) P3HT:PCBM:ZnO (1:1:1 wt. ratio).

Raman spectroscopy was employed to complement the FTIR study in investigating the chemical structure and vibrational properties of P3HT, P3HT:PCBM blend and different ratios of the hybrid ZnO:P3HT:PCBM. The spectra are depicted in

Figure 4.9, showing the different vibrational frequencies of the different vibrational modes. Various groups reported on the vibrational intensities of ZnO and it has been found to be in the region between 350 cm^{-1} and 600 cm^{-1} [4.35 - 4.38]. However, the peak at 500 cm^{-1} can be attributed to the Zn-O deformation. Dakhlaoui et al. [4.39] suggested that the peak at 520 cm^{-1} may be due to the transverse-optical vibration of the silicon substrate.

The peak at 722 cm^{-1} is a result of the C-S-C ring deformation and is also known as the thiophene peak. The bands between 1186 cm^{-1} and 1210 cm^{-1} is ascribed to C-H bending and C-C symmetric stretching, respectively. The broad band peak at 1375 cm^{-1} is due to the C-C stretching deformation in the aromatic thiophene ring. The most interesting band is found in the region between 1400 cm^{-1} and 1500 cm^{-1} and it is attributed to the symmetric C=C stretching deformation [4.40]. One can clearly see that the peak position corresponding to the symmetric C=C stretching deformation, is slightly shifted to lower wavenumber (cm^{-1}), when the polymer is blended with ZnO (1:1 wt. ratio). This is also evident for the PCBM and ZnO (1:1:1 wt. ratio) film. Normally, a downward shift in the wavenumber specifies an increase in the crystallinity of the polymer, and an increase of the effective conjugation length along the polymer backbone [4.41]. Moreover, the intensity of the C=C stretching deformation is higher for the samples blended with ZnO as shown in the inset of Fig. 4.9. This is probably due to a strong ordering of P3HT chains caused by the addition of ZnO. These trivial transformations observed in the symmetric stretching (C=C) are in good agreement with the observation reported by Motaung et al. [4.34].

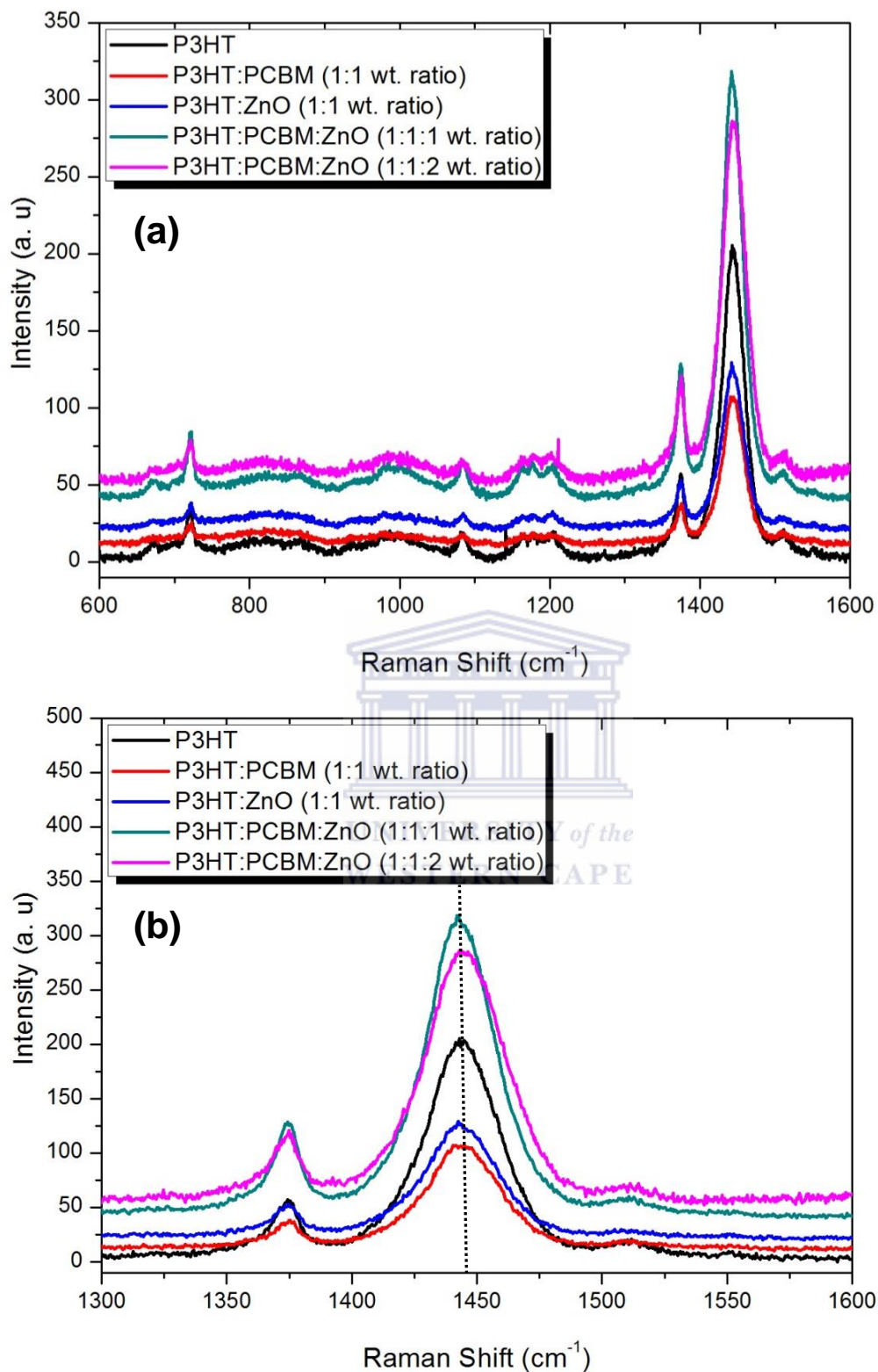


Figure 4.9: Raman spectra of (a) P3HT, P3HT:PCBM (1:1) blend and the hybrid of P3HT:PCBM:ZnO and (b) X-axis re-scaled for a better view of Fig 4.9a.

4.3.3.2. Surface morphology

The FE-SEM cross-sectional view in Figure 4.10 shows the layers of the silicon substrate and an active layer blend of P3HT:PCBM spin-cast from the solution of 1,2-dichlorobenzene. Film thickness is seen as a key factor in the fabrication of the device, i.e. the thicker the active layer the greater is the chance of the film to harvest more photons. We found that the P3HT:PCBM blend from 1,2-dichlorobenzene solution gives the best performance because of the thicker layer formed compared to when chloroform is used as solvent material.

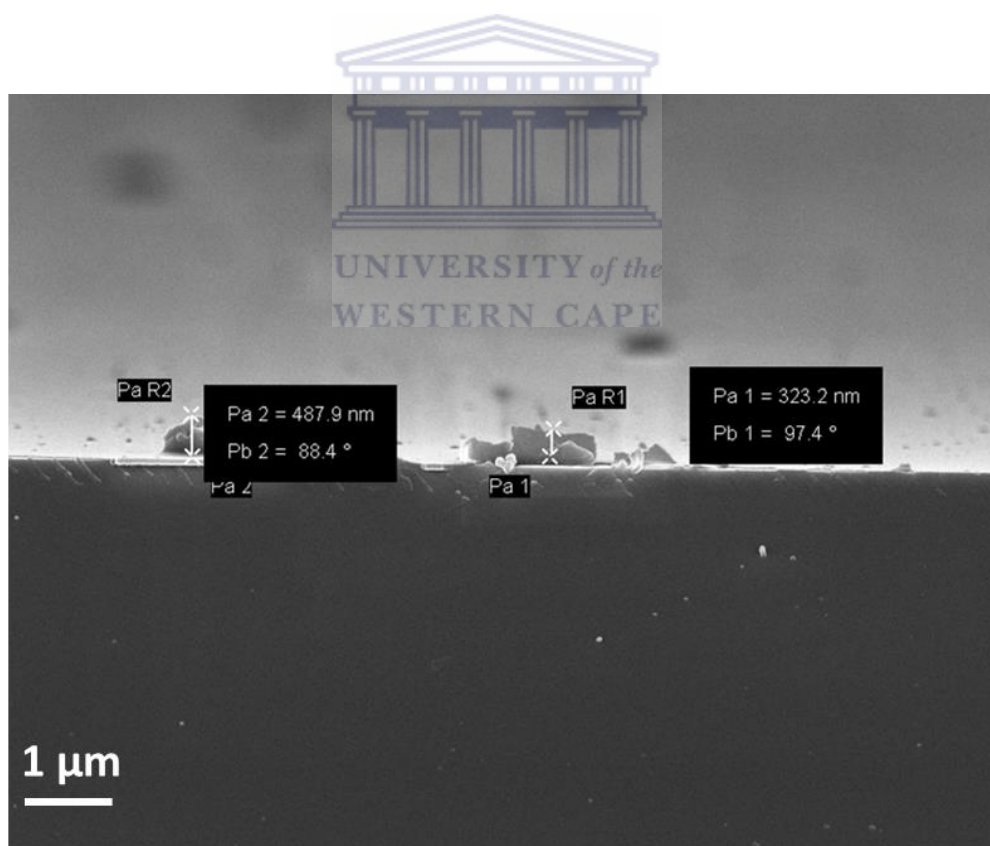


Figure 4.10: FE-SEM cross-sectional view of P3HT:PCBM film on silicon substrate.

To study the topography of P3HT, P3HT:PCBM and hybrid structures of P3HT:PCBM:ZnO in a 1:1:1 and 1:1:2 wt. ratios, AFM height images were extracted in a tapping mode as shown in Fig. 4.11. A pure P3HT film shows a porous structure with diameter ranging from 10-20 nm resulting to a root mean square (RMS) roughness of 1.89 nm. When incorporating the PCBM in the polymer matrix, the pore diameter increases to 30-40 nm. A series of small clusters with a RMS roughness of 2.63 nm is observed in the P3HT: PCBM blended film (Fig. 4.11b), which may be attributed to the PCBM aggregates. Previous results showed that the donor/acceptor (D/A) blend morphology can be controlled by spin-casting the blend from a specific solvent preventing large-size phase separation or enhancing the polymer chain packing [4.42, 4.43]. By incorporating the ZnO nanostructures in the P3HT:PCBM, smaller nanoparticles are observed across the film surface (Fig. 4.11c). However, when increasing the concentration of ZnO to 1:1:2 wt. ratio, the nanoparticles aggregate leading to a phase separation between the interfaces as shown in Fig. 4.11d.

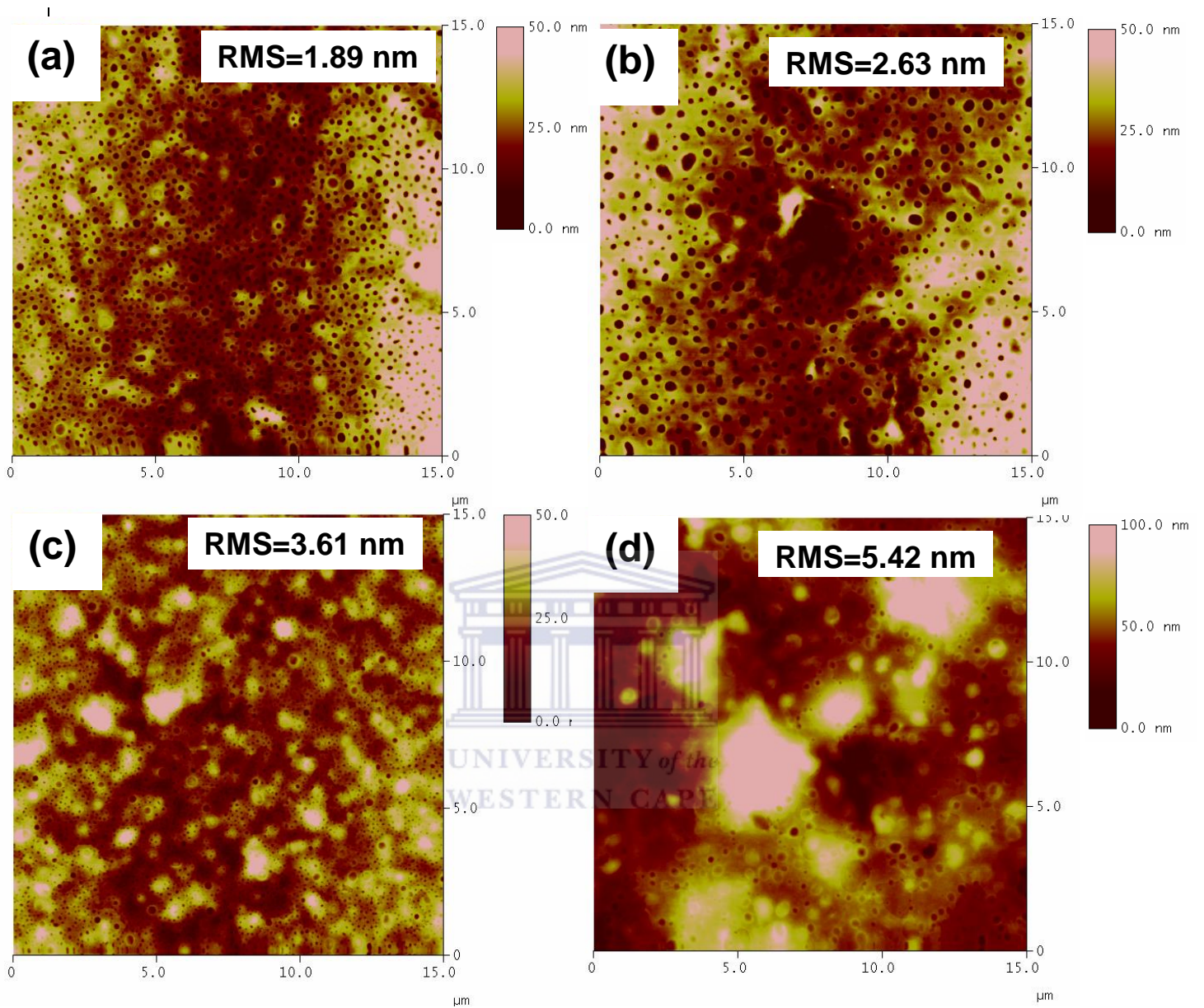


Fig. 4.11: AFM height images of (a) P3HT, (b) P3HT:PCBM, (c) P3HT:PCBM:ZnO (1:1:1 wt. ratio) and (d) P3HT:PCBM:ZnO (1:1:2 wt. ratio)

4.3.3.3. *Optical properties*

Figure 4.12 shows UV-Vis absorbance spectra of P3HT, the P3HT:PCBM blend (1:1 wt. ratio) and P3HT:PCBM:ZnO hybrid (1:1:1 wt. ratio) prepared from 1,2 dichlorobenzene and spin-coated on Corning 7059 glass substrates. A very strong shoulder peak can be observed at 610 nm for P3HT attributed to the π - π^* transition. The maximum absorbance is observed at the wavelengths region between 500 and 550 nm. Chen et al [4.44] also attributed these bands to the π - π^* transition.

It is also noted that on the same Figure 4.12, by blending P3HT with PCBM the intensity of the maximum peak drops compared to P3HT alone. This is as a result of a closely constrained spiral chain yielded by twisting of the polymer backbone of PCBM. The twisting of the polymer backbone results in divisions with shorter conjugation length and weaker inter-chain interaction [4.34]. This result can also be explained by a change in the stacking conformation of the polymer structure from high crystallinity to lower crystallinity, and a reduction of intraplane and interplane stacking, which causes a poor π - π^* transition and lower absorbance [4.45].

Incorporating ZnO in the P3HT:PCBM blend enhances charge transfer and recovers the absorbance intensity of the polymer. A wavelength shift and maximum absorbance intensity of the overall P3HT:PCBM:ZnO (1:1:1 wt. ratio) hybrid result between P3HT alone and the P3HT:PCBM blend. The slight red shift in the spectrum of the P3HT:PCBM:ZnO (1:1:1 wt. ratio) thin film depicted by Figure 4.12 can be attributed to the increase in order of the polymer chains [4.34, 4.46]. Additionally, a

pronounced absorption shoulder is observed around 610 nm for the P3HT:PCBM:ZnO (1:1:1 wt. ratio).

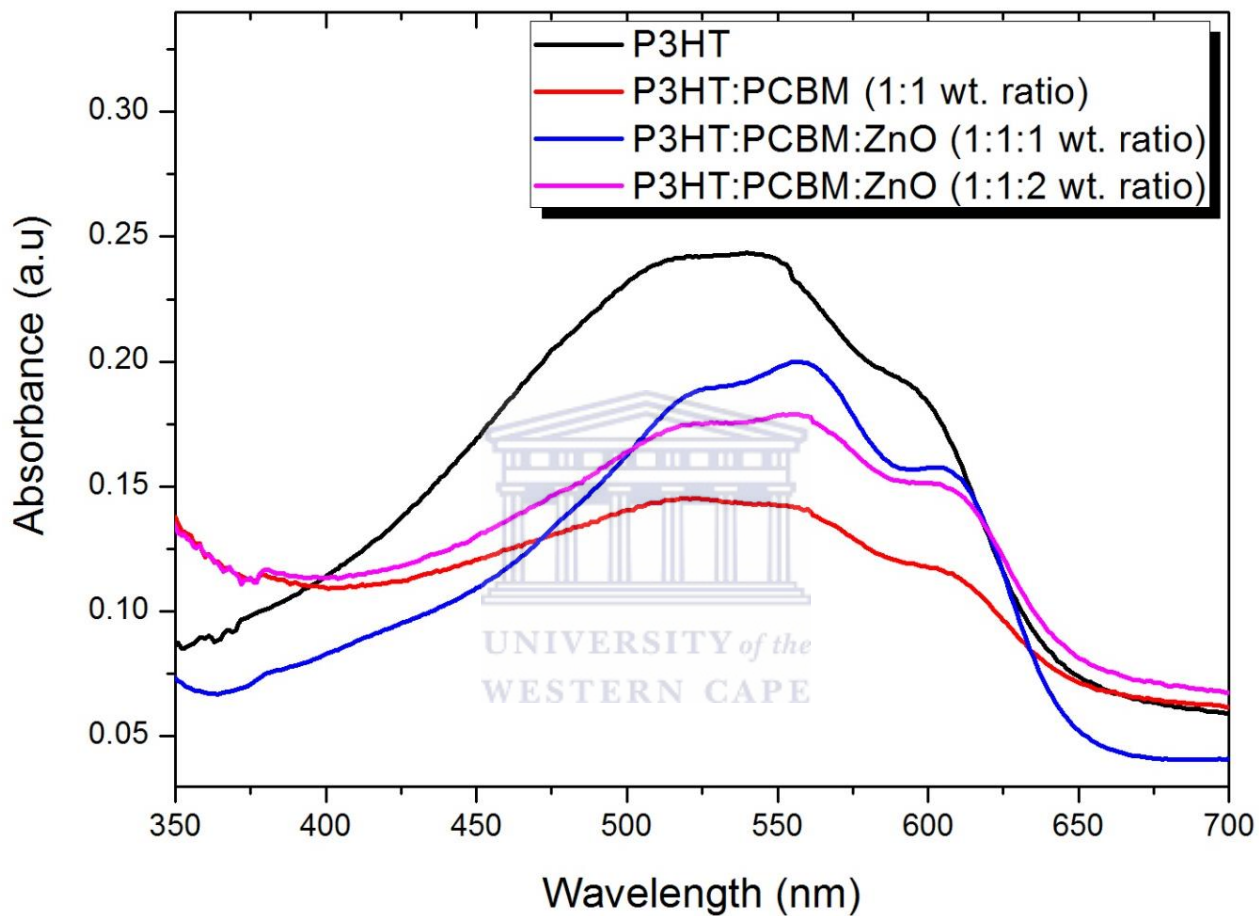
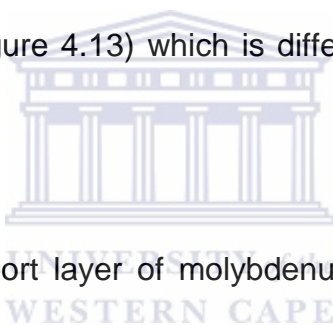


Figure 4.12: UV-VIS absorbance spectra of P3HT, P3HT:PCBM blend and P3HT:PCBM:ZnO hybrid structures).

4.3.3.4. Photovoltaic properties

To fabricate solar cells, an indium tin oxide (surface resistivity of 8-12 Ω/sq) substrate were ultrasonically cleaned in acetone, isopropanol and rinsed in de-ionized water thoroughly. About 90 nm layer of TiO_2 was sputtered using a physical vapour deposition system onto the ITO-coated glass, and was used as electron transport layer. An active layer of P3HT:PCBM and P3HT:PCBM blended with various concentrations of ZnO (0.2, 1, and 2.0 wt. ratio) were dissolved in 1,2 dichlorobenzene (since it showed better solubility as compared to chloroform) and deposited on a thin layer (90 nm) of TiO_2 , resulting in a configuration of ITO/ TiO_2 /P3HT:PCBM and ITO/ TiO_2 /P3HT:PCBM:ZnO (Figure 4.13) which is different than that used by Ikram et al. [4.17].



Then, a thin hole transport layer of molybdenum oxide was deposited (1×10^{-6} mbar) onto the photoactive layer using the physical vapour deposition system, which was followed by evaporation of the top Al electrode using a shadow mask. Current density–voltage (J–V) characteristics were measured using a Keithley 4200 Semiconductor Characterization System and a solar simulator equipped with xenon short arc lamp-based Sciencetech SF150 with 150 W of power and an AM1.5 G solar filter. Light was irradiated from the ITO/glass side. The effective area of the solar cells was measured to be 1.25 cm^2 .

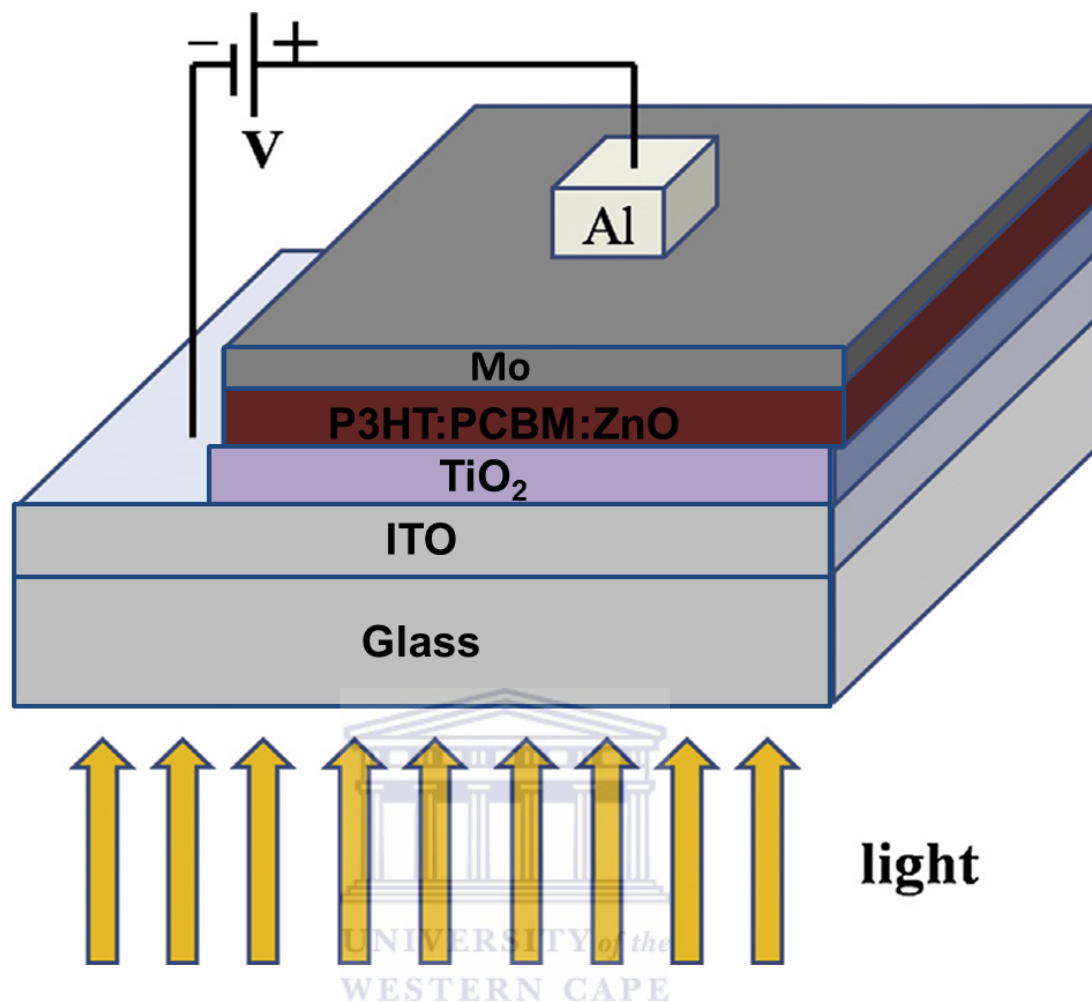


Figure 4.13. Schematic view of P3HT:PCBM:ZnO device architecture.

To investigate the effect of the ZnO on the photovoltaic performance, ZnO nanoparticles with various concentrations (0.2, 1.0 and 2.0 wt. ratio) were incorporated in the P3HT:PCBM devices resulting in a ternary device of ITO/TiO₂/P3HT:PCBM:ZnO/Mo/Al. Figure 4.14 shows the J-V characteristics of the devices characterized in the dark.

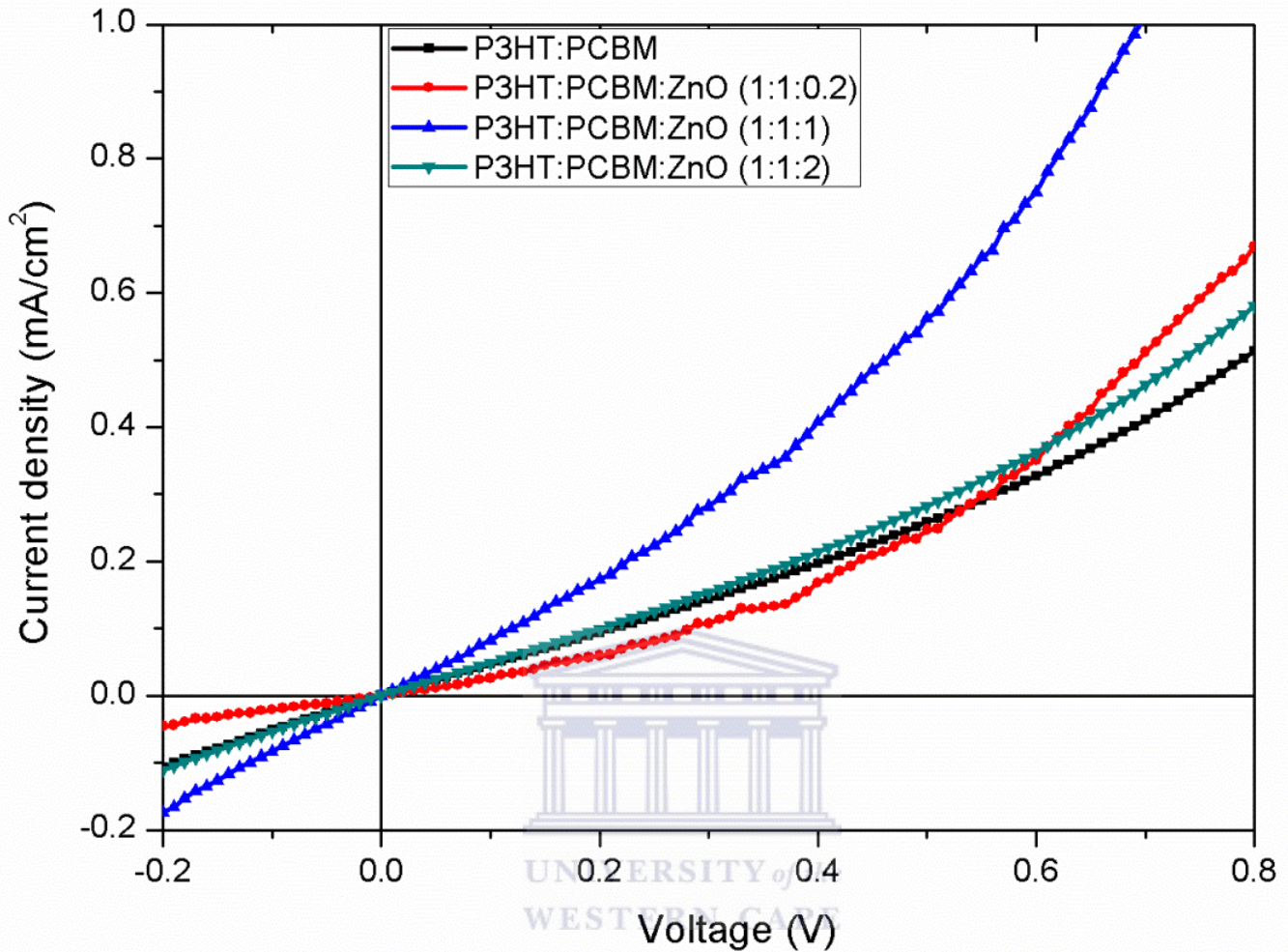


Figure 4.14: Current density–voltage (J–V) curves of the P3HT:PCBM and P3HT:PCBM:ZnO solar cells measured in the dark.

The current density–voltage (J–V) characteristics of the blend and ternary structure measured under simulated AM 1.5 illumination (solar simulator) with an intensity of 100 mW/cm^2 are shown in Figure 4.15 and Table 4.4. An efficiency of 1.0% is recorded for the P3HT:PCBM blend. However, by incorporating ZnO into the P3HT:PCBM polymer matrix to form P3HT:PCBM:ZnO hybrid (1:1:0.2 wt. ratio), the J_{sc}

and FF decreased subsequently resulting in an efficiency of 0.71%. However, when increasing the addition of ZnO to form P3HT:PCBM:ZnO (1:1:1 wt. ratio), the J_{SC} and FF improved due to a percolation network of ZnO nanostructures that facilitates the electron transport in the photoactive layer. The increase of J_{SC} and FF might be due to the strong field formed between the organic material and ZnO nanostructures [4.47]. This increase in ZnO weight concentration (1:1:1) resulted in a superior efficiency of 1.72 %. It is suggested that the increase in V_{OC} in ternary blend is due to the energy level alignment between the highest occupied molecular orbital (HOMO) of P3HT and ZnO. Therefore the energy offset in the vacuum levels between polymer and ZnO pushed the HOMO level of P3HT down and resulted in larger difference of 0.4–0.5 eV between the HOMO of P3HT and ZnO as previously observed by Feng et al. [4.48]. Such increase in efficiency can also be attributed to the improved conductivity, carrier mobility and photon harvesting induced by ZnO, which provide maximum donor-acceptor interface and an efficient conducting pathway for efficient exciton dissociation, transport and collection of charges [4.49]. These results are comparable to that obtained by Ikram et al. [4.17] for P3HT:PCBM:ZnO (1:0.55:0.15 wt. ratio).

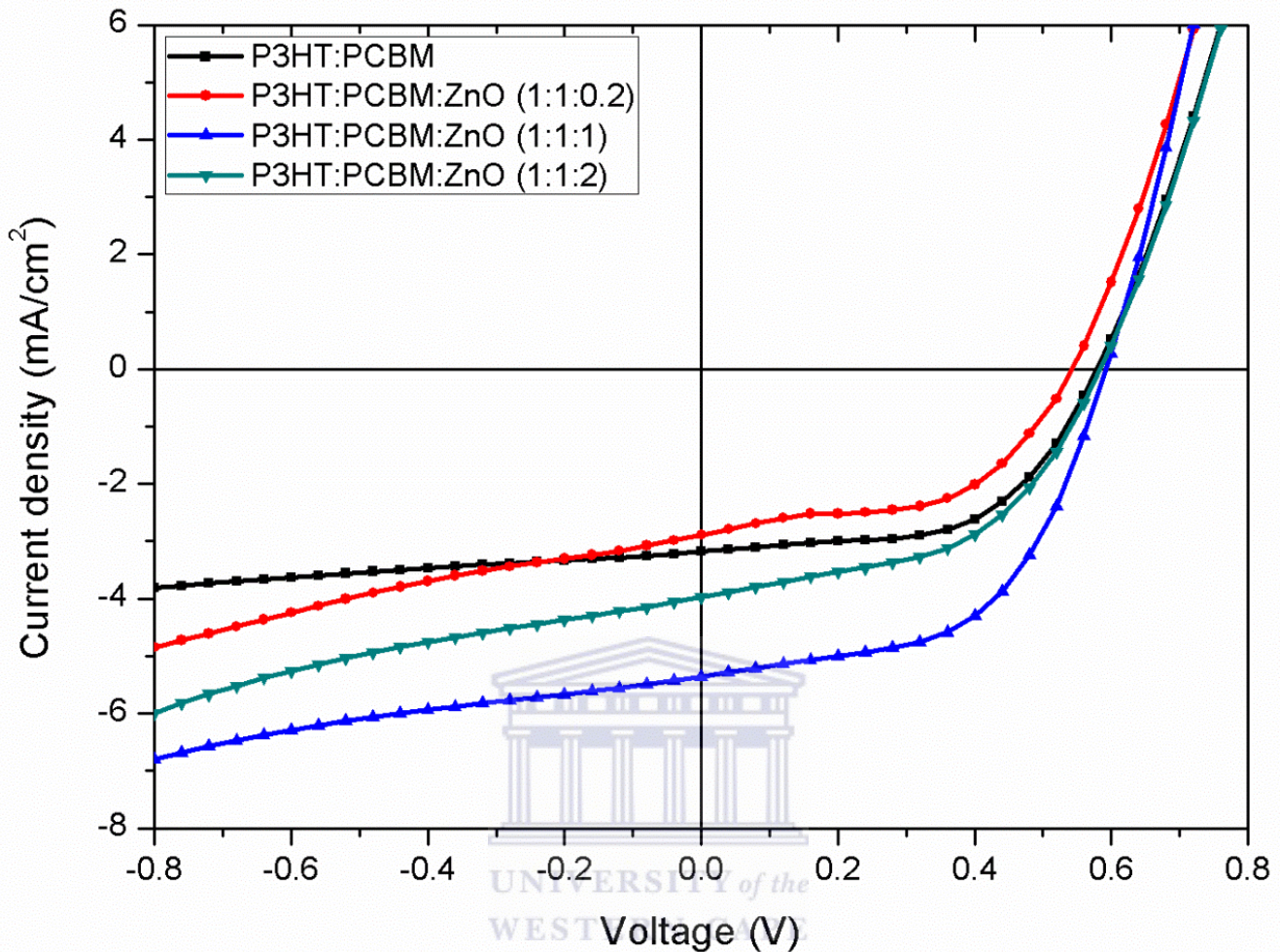


Figure 4.14: Current density–voltage (J–V) curves of the P3HT:PCBM and P3HT:PCBM:ZnO solar cells measured under white light illumination.

It is interesting to note that when the concentration of ZnO is increased further by a factor of 2 in a 1:1:2 wt. ratio; a FF of about 0.48 is observed resulting in a PCE of about 1.11%. This is probably due to the excess amount of ZnO creating a thicker layer in which the large surface-to-bulk ratio causes grain defects. Furthermore, the excess ZnO will lead to a decrease in the electrical conductivity. The low efficiency at higher thickness layer may be attributed to the low hole mobility in the film [4.50]. Malgas et al.

[4.51] reported that higher excess of ZnO in the polymer surface results in the formation of large ZnO agglomerations, a rougher surface as well as thicker P3HT:PCBM:ZnO layer, which in turn result in a large scale phase separation between the P3HT, PCBM and ZnO interface.

Table 4.4: Summary of photovoltaic properties of hybrid solar cells with different concentration of ZnO nanoparticles.

Films	V_{oc} (V)	J_{sc} (mA/cm ²)	FF	PCE (%)
P3HT:PCBM	0.58	3.19	0.55	1.00
P3HT:PCBM:ZnO (1:1:0.2)	0.54	2.87	0.46	0.71
P3HT:PCBM:ZnO (1:1:1)	0.59	5.33	0.55	1.72
P3HT:PCBM:ZnO (1:1:2)	0.58	3.98	0.48	1.11

This causes less charge generation and less available percolation pathways for electrons in the ZnO phase to reach the aluminum electrode. In addition, as shown in AFM analyses, at higher ZnO concentration, the RMS surface roughness increased revealing higher phase-separation between the donor and acceptor. The coarse

morphology of the (1:1:2 wt. ratio) ternary film result in poor contact between the active layer and cathode and increases the resistance. Additionally, the bumpy surface also scatters light away from the device. Previous studies reported that the rough surface reduces the efficiency of organic solar cells due to the formation of shunts [4.52-4.55].

4.4. CONCLUSION

In summary, the incorporation of ZnO nanoparticles in the active layer of P3HT:PCBM bulk heterojunction solar cells was investigated. Topography analyses revealed larger phase separation on thin films spin-coated from chloroform as compared to those prepared from dichlorobenzene indicating that chloroform as a solvent offers inappropriate morphology due to its lower solubility in P3HT and ZnO, as compared to 1,2 dichlorobenzene solvent. HR-TEM revealed that the hexagonal structure of ZnO is still maintained after incorporating ZnO nanoparticles in the P3HT:PCBM blend due to the fact that the structure is mostly polycrystalline in nature and this is consistent with the XRD results. Raman spectroscopy revealed a downward shift in the wavenumber of the (1:1:1 wt. ratio) hybrid film, specifying an increase in the crystallinity of the polymer, and effective conjugation length along the polymer backbone. UV-vis spectroscopy, showed that incorporation of ZnO in the P3HT:PCBM blend results in a slight red shift in the spectrum of the P3HT:PCBM:ZnO (1:1:1 wt. ratio) thin film due to the increase in order of the polymer chains. Photovoltaic results revealed that the addition of ZnO nanoparticles results in an increase in the PCE from a baseline of ~1.0 % in the P3HT:PCBM system to 1.7% in the P3HT:PCBM:ZnO ternary system. The enhanced PCE was due to improved absorption as compared to its

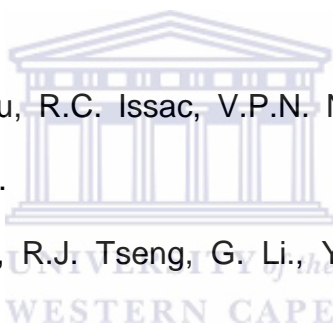
counterparts. Upon increasing the addition of ZnO nanoparticles in the P3HT:PCBM matrix, the PCE decreases, due to a large phase separation between the polymer, PCBM and ZnO induced by ZnO agglomerations which resulted in increased surface roughness of the active layer.



4.5. REFERENCES

- [4.1] F.C. Krebs, J. Alstrup, H. Spanggaard, K. Larsen, E. Kold, Sol. Energy Mater. Sol. Cells 83 (2004) 293.
- [4.2] H. Spanggaard, F.C. Krebs, Sol. Energy Mater. Sol. Cells 83 (2004) 125.
- [4.3] D.E. Motaung, G.F. Malgas, C.J. Arendse, T. Malwela, Mater. Chem. Phys. 124 (2010) 208.
- [4.4] E. Bundgaard, F.C. Krebs, Sol. Energy Mater. Sol. Cells 91 (2007) 954.
- [4.5] F.C. Krebs, H. Spanggaard, Chem. Mater. 17 (2005) 5235.
- [4.6] F.C. Krebs, K. Norrman, Prog. Photovolt.: Res. Appl. 15 (2007) 697.
- [4.7] H. Neugebauer, C.J. Brabec, J.C. Hummelen, N.S. Sariciftci, Sol. Energy Mater. Sol. Cells 61 (2000) 35.
- [4.8] J.A. Hauch, P. Schilinsky, S.A. Choulis, R. Childers, M. Biele, C.J. Brabec, Sol. Energy Mater. Sol. Cells 92 (2008) 727.
- [4.9] M. Jørgensen, K. Norrman, F.C. Krebs, Sol. Energy Mater. Sol. Cells 92 (2008) 686.
- [4.10] Heliatek. Available at: [/http://www.heliatek.comS](http://www.heliatek.comS) (accessed 11.21.2011).
- [4.11] Konarka. Available at: [/http://www.konarka.comS](http://www.konarka.comS) (accessed 11.21.2011).
- [4.12] S. Aramaki, M.R.S. Boston, Fall Meeting, 2011
- [4.13] W.U. Huynh, J.J. Dittmer, A.P. Alivisatos, Science 295 (2002) 2425.
- [4.14] B. Sun, E. Marx, N.C. Greenham, Nano Lett. 3 (2003) 961.
- [4.15] W.J.E. Beek, M.M. Wienk, R.A. J. Janssen, Adv. Funct. Mater. 16 (2006) 1112.
- [4.16] S.H. Oh, S.J. Heo, J.S. Yang, H.J. Kim, ACS Appl. Mater. Interfaces 5 (2013) 11530.

- [4.17] M. Ikram, R. Murray, A. Hussain, S. Alid, S. Ismat Shaha, Mater. Sci. Engineering B 189 (2014) 64.
- [4.18] D.E. Motaung, G.F. Malgas, C.J. Arendse, J. Mater. Sci. 46 (2011) 4942.
- [4.19] M. Manceau, A. Rivaton, J.L. Gardette, S. Guillerez, N. Lemaitre, Polym. Degrad. Stab 94 (2009) 898.
- [4.20] D.E. Motaung, G.F. Malgas, C.J. Arendse, Synth. Met. 160 (2010) 876.
- [4.21] M.S.A. Abdou, S. Holdcroft, Can. J. Chem. 73 (1995) 1893
- [4.22] Y. Furukawa, M. Akimoto, I. Harada, Synth. Met. 18 (1987) 151
- [4.23] V. Shrotriya, J. Ouyang, R.J. Tseng, G. Li, Y. Yang, Chem. Phys Lett. 411 (2005) 138.
- [4.24] S.S. Harilal, C.V. Bindhu, R.C. Issac, V.P.N. Nampoori, C.P.G. Vallabhan, J. Appl. Phys. 82 (5) (1997).
- [4.25] V. Shrotriya, J. Ouyang, R.J. Tseng, G. Li., Y. Yang, Chem. Phys. Lett.411 (2005) 138.
- [4.26] K. Takanezawa, K. Tajima, K. Hashimoto, Appl. Phys. Lett. 93 (1–3) (2008) 063308.
- [4.27] H. Kleinwechter, C. Janzen, J. Knipping, et al., J. Mater Sci, 37 (2002) 4349
- [4.28] O.M. Ntwaeaborwa, R. Zhou, L. Qian, S.S. Pitale, J. Xue, H.C. Swart, P.H. Holloway, Physica B 407 (2012) 1631.
- [4.29] H. Kim, W.-W. So, S.-J. Moon, Solar Energy Mater. Sol. Cells 91 (2007) 581.
- [4.30] J. Zhou, F. Zhao, Y. Wang, Y. Zhang, L. Yang, J. Lumines. 122-123 (2007) 195.
- [4.31] Z.M. Khoshhesab, M. Sarfaraz, M.A. Asadabad, Metal-Organic and Nano-Metal Chemistry 41 (2011) 814.

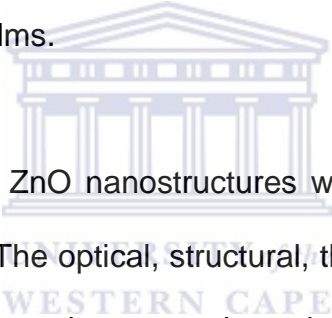


- [4.32] D.M. DeLongchamp, B.M. Vogel, Y. Jung, M.C. Gurau, C.A. Richter, O.A. Kirillov, J. Obrzut, D.A. Fischer, S. Sambasivan, L.J. Richter, E.K. Lin, Chem.Mater. 17 (2005) 5610.
- [4.33] D.E. Motaung, G.F. Malgas, S.S. Nkosi, G.H. Mhlongo, B.W. Mwakikunga, T. Malwela, C.J. Arendse, T.F.G. Muller, et al, J. Mater. Sci. 48 (2013) 1763.
- [4.34] D.E. Motaung, G.F. Malgas, C.J. Arendse, S.E. Mavundla, Mat. Chem. Phys. 135 (2012) 401.
- [4.35] S.S. Harilal, C.V. Bindhu, R.C. Issac, V.P.N. Nampoori, C.P.G. Vallabhan, J. Appl. Phys. 82 (5) (1997).
- [4.36] B. Kumar, H. Gong, S.Y. Chow, S. Tripathy, Y. Hua, Appl Phys Lett 89 (2006) 7.
- [4.37] A. Umar, B.Karunagaran, E.K. Suh, Y.B. Hahn, Nanotechnology 17 (2006; 17: 4072.
- [4.38] A. Khan, M.E. Kordesch, Mater. Lett 62 (2008) 230.
- [4.39] A. Dakhlaoui M. Jendoubi, L.S. Smiri, A. Kanaev, N. Jouini, J. Cryst Growth 311 (2009) 3989.
- [4.40] E. Klimov, W. Li, X. Yang, G.G. Hoffmann, J. Loos, Macromolecules 39 (2006) 4493.
- [4.41] C. Heller, G. Leising, C. Godon, S. Lefrant, W. Fischer, Phys. Rev. B 51 (1995) 8107.
- [4.42] S.E. Shaheen, C.J. Brabec, N.S. Sariciftci, F. Padinger, T. Fromherz, J.C. Hummelen, Appl Phys Lett 78 (2001) 841.
- [4.43] J.K.J. van Duren, X. Yang, J. Loos, C.W.T. Bulle-Lieuwma, A.B. Sieval, J.C. Hummelen, R.A.J. Janssen, Adv Funct Mater 14 (2004) 425

- [4.44] T-A. Chen, X. Wu and D. Rieke J. Amer. Chem. Soc. 117 (1995) 233.
- [4.45] V. Shrotriya, J. Ouyang, R. J. Tseng, G. Li, Y. Yang, Chem. Phys. Lett. 411 (2005) 138.
- [4.46] Y. Kim, S. Cook, S.M. Tuladhar, S.A. Choulis, J. Nelson, J.R. Durrant, D.D.C. Bradley, M. Giles, I. McCulloch, C.S. Ha, M. Ree, Nat. Mater. 5 (2006) 197.
- [4.47] S.H. Oh, S.J. Heo, J.S. Yang, H.J. Kim, ACS Appl. Mater. Interfaces 5 (2013) 11530.
- [4.48] W. Feng, S. Rangan, Y. Cao, E. Galoppini, R.A. Bartynski, E. Garfunkel, J. Mater. Chem. A2 (2014) 7034.
- [4.49] D.C. Olson, S.E. Shaheen, R.T. Collins, D.S. Ginley, J. Phys. Chem. C 111 (2007) 16670.
- [4.50] D.E. Motaung, G.F. Malgas, C.J. Arendse, S.E. Mavundla, C.J. Oliphant, D. Knoesen, Sol. Energy Mater. Sol. Cells 93 (2009) 1674.
- [4.51] G.F. Malgas, D.E. Motaung, G.H. Mhlongo, S.S. Nkosi, B.W. Mwakikunga, M. Govendor, C.J. Arendse, T.F.G. Muller, Thin Solid Films 555 (2014) 100.
- [4.52] G. Li, V. Shrotriya, J. Huang, Y. Yao, T. Moriarty, K. Emery, Y. Yang, Nat. Mater. 4 (2005) 864.
- [4.53] E.-K. Park, J.-H. Kim, I.A. Ji, H.M. Choi, J.-H. Kim, K.-T. Lim, J.H. Bang, Y.-S. Kim, Microelectronic Engineering 119 (2014) 169.
- [4.54] Y. Guo, H. Geng, Thin Solid Films 519 (2011) 2349.
- [4.55] D.E. Motaung, G.F. Malgas, S.S. Ray, C.J. Arendse, Thin Solid Films 537 (2013) 90.

SUMMARY

In spite of technological advances and increasing market volumes, the price of solar energy remains relatively high compared to that of grid electricity due to high material and production costs. Ongoing efforts by science and industry to reach a breakthrough in the long-term contribution of PV to the global energy supply are therefore often devoted to cost reduction by investigating improved as well as novel technologies such as the effect of the additional electron acceptor in hybrid ZnO:P3HT:PCBM spin-coated films.



In the thesis, high purity ZnO nanostructures were synthesized using a simple hydrothermal assisted method. The optical, structural, thermal, chemical and vibrational properties of the as-synthesized products were investigated in detail. TGA showed high thermal weight loss. X-ray diffraction, HR-TEM and Raman analyses demonstrated that the as-synthesized products have wurtzite structure and are polycrystalline in nature. Raman scattering analyses confirmed the as-prepared products have good crystal quality. XPS analysis revealed that ZnO films are stoichiometric with Zn/O atomic ratio very close to that of ZnO single crystal. UV-vis absorption spectra exhibited that the absorption band of the ZnO is around 360 nm, which is blue-shifted relative to the bulk exciton absorption (373 nm) due to the quantum confinement effect.

The incorporation of ZnO nanoparticles in the active layer of P3HT:PCBM bulk heterojunction solar cells as an additional electron acceptor was investigated. The concentration of ZnO in the polymer matrix was varied between 0.2 to 2 wt. ratios. The slight red shift and a pronounced absorption shoulder around 610 nm in the spectrum of the P3HT:PCBM:ZnO (1:1:1 wt. ratio) thin film was observed and attributed to the increase in order of the polymer chains. The photovoltaic properties demonstrated a power conversion efficiency (PCE) of ~1.0 % in P3HT:PCBM system and 1.7% in P3HT:PCBM:ZnO (1:1:1) hybrid system. This was due to the incorporation of ZnO nanostructures in the P3HT:PCBM polymer matrix, which facilitates the electron transport in the photoactive layer resulting in improved efficiency. Increasing the concentration of ZnO to P3HT:PCBM:ZnO (1:1:2 wt. ratio) hybrid led to a decrease in the PCE due to large-phase separation induced by excess ZnO in the polymer surface. Therefore based on the above analyses we can conclude that the P3HT:PCBM:ZnO (1:1:1 wt. ratio) hybrid is the most desirable weight ratio for improved efficiency.

FUTURE WORK

A manuscript for a journal article emanating from this work is being prepared, further work is under way to fabricate devices and explore the relationship between their photovoltaic performances and the film morphology from different solvents.